



**Sol-Gel Derived Particles, Low-Sintering Temperature Ceramic, Thin and Thick
Films of Barium Zirconate Titanate System**

Nawal Binhayeeniyi

**A Thesis Submitted in Fulfillment of the Requirements
for the Degree of Doctor of Philosophy in Physics**

Prince of Songkla University

2011

Copyright of Prince of Songkla University

Thesis Title Sol-gel derived particles, low-sintering temperature ceramic,
thin and thick films of barium zirconate titanate system
Author Ms. Nawal Binhayeeniyi
Major Program Physics

Major Advisor :

.....
(Assoc. Prof. Dr. Nantakan Muensit)

Co-advisor :

.....
(Prof. Dr. Claude Lucat)

Examining Committee :

.....Chairperson
(Prof. Dr. Piyasan Prasertthdam)

.....
(Assoc. Prof. Dr. Nantakan Muensit)

.....
(Prof. Dr. Claude Lucat)

.....
(Dr. Chanchana Thanachayanont)

.....
(Assist. Prof. Dr. Pornsuda Bomlai)

The Graduate School, Prince of Songkla University, has approved this
thesis as fulfillment of the requirements for the Doctor of Philosophy in Physics

.....
(Prof. Dr. Amornrat Phongdara)
Dean of Graduate School

ชื่อวิทยานิพนธ์ อนุภาค เซรามิก ฟิล์มหนาและฟิล์มบางของแบเรียมเซอร์โคเนตไทเทเนตที่ดัดแปลงเตรียมด้วยวิธีโซลเจล

ผู้เขียน นางสาวนวัต บินหะยีนียิ

สาขาวิชา ฟิสิกส์

ปีการศึกษา 2553

บทคัดย่อ

งานวิจัยนี้ศึกษาการเตรียมอนุภาค เซรามิก ฟิล์มบาง ฟิล์มหนาของแบเรียมเซอร์โคเนตไทเทเนตหรือบีซีที ($\text{Ba}(\text{Zr}_x\text{Ti}_{1-x})\text{O}_3$, BZT) ด้วยวิธีโซลเจล โดยที่ x คือปริมาณของเซอร์โคเนียมโดยโมล

ฟิล์มบางบีซีทีที่เตรียมได้มีค่าหนา 300 ถึง 400 นาโนเมตร เตรียมขึ้นโดยการฉาบที่ละชั้นบนฐานรอง Pt/Ti/SiO₂/Si เสาที่อุณหภูมิ 800 องศาเซลเซียส เป็นเวลา 30 นาที ทำการศึกษาโครงสร้างผลึกของฟิล์มจากผลการเลี้ยวเบนของรังสีเอ็กซ์ พบว่าฟิล์มทั้งหมดมีโครงสร้างแบบเพอรอฟสไกต์ และมีการเรียงตัวแบบสุ่ม โดยฟิล์มที่ไม่มีส่วนประกอบของเซอร์โคเนียมจะมีองค์ประกอบของเฟสเตตระโกนอล ส่วนฟิล์มบาง $\text{Ba}(\text{Zr}_{0.05}\text{Ti}_{0.95})\text{O}_3$ มีองค์ประกอบเฟสแบบออโรธอมบิก และองค์ประกอบของเฟสโรมโบฮีดรอลคือ ฟิล์มบาง $\text{Ba}(\text{Zr}_{0.10}\text{Ti}_{0.90})\text{O}_3$ และ $\text{Ba}(\text{Zr}_{0.15}\text{Ti}_{0.85})\text{O}_3$ ท้ายสุดฟิล์มบาง $\text{Ba}(\text{Zr}_{0.20}\text{Ti}_{0.80})\text{O}_3$ องค์ประกอบของเฟสคือ คิวบิก ค่าคงที่ไดอิเล็กตริกที่สูงที่สุดพบในฟิล์มบาง $\text{Ba}(\text{Zr}_{0.20}\text{Ti}_{0.80})\text{O}_3$ วัดค่าคงที่โพลาไรเซชันไดอิเล็กตริกของทุกฟิล์มด้วยระบบอินเทอร์เฟอโรมิเตอร์แบบไม่เคลื่อนพบที่ฟิล์มบาง $\text{Ba}(\text{Zr}_{0.05}\text{Ti}_{0.95})\text{O}_3$ มีค่าคงที่โพลาไรเซชันไดอิเล็กตริก d_{33} มากที่สุดคือเท่ากับ 35 pm/V และมีค่ามากกว่าฟิล์มที่ตัดส่วนอื่นๆ

การเตรียมอนุภาคเซรามิกบีซีทีด้วยวิธีโซลเจลที่มีความความเป็นเนื้อเดียวกันสูง ส่วนการเติมสารเจือลิเทียมออกไซด์ (Li₂O) พบว่าช่วยลดอุณหภูมิการเผาแคลไซน์จาก 1100 องศาเซลเซียส เหลือ 700 องศาเซลเซียส และได้นำอนุภาคเป็นสารตั้งต้นในการเตรียมเซรามิก และพบว่าสามารถลดอุณหภูมิอบผนึกจาก 1250 องศาเซลเซียส เหลือ 900 องศาเซลเซียส

งานวิจัยนี้ได้เตรียมไมโครคานดิลเวอร์ที่มีโครงสร้างอิสระแบบปลายเปิดบีซีทีด้วยวิธีสกรีนจลุลาย ร่วมกับวิธีกำจัดชั้นรองคาน ที่ใช้เตรียมในระบบเลดเซอร์โคเนตไททานตโดยเตรียมจากอนุภาคเซรามิกที่เริ่มต้นด้วยวิธีโซลเจล ที่มีสมบัติทางไฟฟ้ากลที่ดีที่สุดคือ $\text{Ba}(\text{Zr}_{0.05}\text{Ti}_{0.95})\text{O}_3$ และเจือด้วยสารเจือลิเทียมออกไซด์ ซึ่งสามารถใช้ได้ดีกับขั้วไฟฟ้าทอง ดังนั้นจาก

การศึกษาวัสดุพีซีทีในงานวิจัยนี้ คาดว่าจะมีการประยุกต์ใช้วัสดุพีซีทีในอุปกรณ์ไมโครอิเล็กทรอนิกส์เพิ่มขึ้นเรื่อยๆ ในอนาคต

Thesis Title Sol-gel derived particles, low-sintering temperature ceramic, thin and thick films of barium zirconate titanate system
Author Ms. Nawal Binhayeeniyi
Major Program Physics
Academic Year 2010

ABSTRACT

This work presents barium zirconate titanate or $\text{Ba}(\text{Zr}_x\text{Ti}_{1-x})\text{O}_3$ or BZT prepared by reliable synthetic sol-gel route into different forms, powder, ceramic, thin and thick films. Hence, the x value refers to the zirconium content by mol.

The 300-400 nm of BZT thin films were prepared by a sol-gel method on a conventional Pt/Ti/SiO₂/Si substrates. The pyrolysis of 350 °C and annealing of 800°C were used in the procedure. All the films crystallized into perovskite phase. Without Zr, the film crystallized into tetragonal structure, $\text{Ba}(\text{Zr}_{0.05}\text{Ti}_{0.95})\text{O}_3$ into orthorhombic. It is rhombohedral for both $\text{Ba}(\text{Zr}_{0.10}\text{Ti}_{0.90})\text{O}_3$ and $\text{Ba}(\text{Zr}_{0.15}\text{Ti}_{0.85})\text{O}_3$. Finally, the $\text{Ba}(\text{Zr}_{0.20}\text{Ti}_{0.80})\text{O}_3$ is cubic. The permittivity of the film increased with Zr contents and reached its maximum value obtained from the $\text{Ba}(\text{Zr}_{0.20}\text{Ti}_{0.80})\text{O}_3$ thin films. For the piezoelectric response of thin films, it was effectively observed using a modified Michelson interferometer and the measured piezoelectric coefficient d_{33} of 35 pm/V was obtained from the $\text{Ba}(\text{Zr}_{0.05}\text{Ti}_{0.95})\text{O}_3$ thin film.

Sol-gel derived particles of BZT were prepared with high uniformity. The Li₂O additive reduced the calcination of the $\text{Ba}(\text{Zr}_{0.05}\text{Ti}_{0.95})\text{O}_3$ powder from 1,100 °C to be 700 °C. These structures are perovskite. The $\text{Ba}(\text{Zr}_{0.05}\text{Ti}_{0.95})\text{O}_3$ powder and Li₂O sintering additive was further used as the basis of synthesizing BZT ceramic at low-sintering temperature, 900 °C.

The BZT with composition exhibiting the best electromechanical property, $\text{Ba}(\text{Zr}_{0.05}\text{Ti}_{0.95})\text{O}_3$, were comparatively used for fabricating free-standing thick films. The technology consists of the screen-printing method with sacrificial layer which has been standardized for the lead-based system. The procedure was validated for producing the BZT powder with the Li₂O additive and gold electrodes.

From the study on the BZT materials in this work, it is anticipated that their applications in micro-electronic devices are increasing in the future.

ACKNOWLEDGEMENTS

This research has been financially supported under the Program Strategic Scholarships for Frontier Research Network for the Jointed Ph.D. Program Thai Doctoral Degree from the Office of the Higher Education Commission, Bangkok, the funding from NANOTEC Center of Excellence at Prince of Songkla University, Songkhla, the funding from PSU Graduate School, the funding the Princess of Naradhiwas University, Narathiwat and the Franco-Thai Joint Research Project under the Office of the Higher Education Commission, Thailand and the Partenariat Hubert Curien (PHC) Program, France.

I highly thank Asst. Prof. Dr. Chongrak Palasai, the President of Princess of Naradhiwas University, Narathiwat for giving me an opportunity advance my higher education.

I would like to sincerely thank my thesis advisor, Assoc. Prof. Dr. Nantakan Muensit, for her advice, encouragement and supervision. Her warm guidance and complete support made me active in doing the research.

I would to express my sincere appreciation to my co-advisor Prof. Dr. Claude Lucat who has been giving me invaluable guidance while I was at the Laboratoire de L' Intégration du Matériau au Système (IMS), Bordeaux 1 University, Bordeaux, France. Besides, I am grateful to Riadh Lakmi, Guillaume Blanchot, Dr. Christophe Castille, and Dr. Héléne Debéda-Hickel, for their friendships and helping hands.

I would like to thank the Examining Committee, Prof. Dr. Piyasan Praserttham, Department of Chemical Engineering, Faculty of Engineering, Chulalongkorn University, Prof. Dr. Claude Lucat, Director of Research CNRS, Bordeaux, France, Dr. Chanchana Thanachayanont, National Metals and Materials Technology Center (MTEC), and Asst. Prof. Dr. Pornsuda Bomlai, Department of Materials Science and Technology, Faculty of Science, Prince of Songkla University.

I am indebted to the encouragements from my friends, in particular, Dr. Panya Khaenamkaew and Dr. Chatchai Putson, Pisan Sukwisut, including the members in the Material Physics Laboratory.

The most important support of my soul has been delivered by these people; my parents, brothers and husband, my deep thanks have been given to them.

My special thanks go to Allah. Whenever I asked Allah for strength, Allah gave me difficulties to strengthen me. I asked Allah for wisdom and Allah gave me problems to solve. I asked Allah for encouragement and Allah gave me obstacles to overcome. I asked Allah for favours and Allah gave me opportunities. Maybe I receive nothing I want, but I receive everything I need. This is all a precious gift from Allah during my academic work life, Alhamdulillah.

Nawal Binhayeeniyi

TABLES OF CONTENTS

ABSTRACT (Thai)	iii
ABSTRACT (English)	v
ACKNOWLEDGEMENTS	vii
TABLES OF CONTENTS	ix
LIST OF FIGURES	xiii
LIST OF TABLES	xx
SYMBOLS	xxii
CHAPTER 1: INTRODUCTION	1
1.1 Statement of the problem	1
1.2 Thesis outline.....	2
1.3 Objectives of research.....	3
CHAPTER 2: BACKGROUND THEORY	4
2.1 Introduction to piezoelectricity.....	4
2.1.1 Polarity, polarization behavior and poling process.....	4
2.1.2 Perovskite-type materials	8
2.1.3 Piezoelectric effect.....	9
2.2 Common piezoceramics.....	13
2.3 Barium titanate and barium zirconate titanate systems.....	16
2.3.1 Barium titanate (BaTiO ₃) system.....	16
2.3.2 Barium zirconate titanate (Ba(Zr _x Ti _{1-x})O ₃) system	17
2.4 Various techniques for fabricating the powder, ceramic and thin film of perovskite materials.....	18
2.5. Thick film technology.....	23
2.5.1 Screen-printing process.....	23
2.5.2 Paste materials.....	24

TABLES OF CONTENTS (cont.)

2.5.3 Screen meshes.....	25
2.5.4 Substrates.....	26
2.5.5 Screen-printed elements of various designs.....	26
CHAPTER 3: SOL-GEL BARIUM ZIRCONATE TITANATE THIN FILMS	30
3.1 Introduction.....	30
3.2 Review of previous work.....	31
3.3 Materials and methods.....	34
3.3.1 Preparation of the Ba(Zr _x Ti _{1-x})O ₃ precursors.....	34
3.3.2 Thin film fabrication.....	36
3.3.3 Characterization of the thin film.....	37
3.4 Results and discussion	39
3.4.1 Thermogravimetric characterization.. ..	39
3.4.2 X-ray diffractions data	40
3.4.3 Raman spectroscopy	45
3.4.4 Microstructure of Ba(Zr _x Ti _{1-x})O ₃ thin films.....	47
3.4.5 Dielectric property and piezoelectric coefficient	55
3.5 Conclusions.....	60
CHAPTER 4: BARIUM ZIRCONATE TITANATE POWDERS	62
4.1 Introduction.....	62
4.2 Review of previous work.....	62
4.3 Materials and methods.....	64
4.3.1 Preparation of the Ba(Zr _x Ti _{1-x})O ₃ powders	64
4.3.2 Low-temperature synthesized Ba(Zr _{0.05} Ti _{0.95})O ₃ powder	65

TABLES OF CONTENTS (cont.)

4.4	Characterization of the Ba(Zr _x Ti _{1-x})O ₃ powders.....	66
4.5	Results and discussion.....	66
4.5.1	XRD patterns, Raman spectroscopic data and TEM analysis.....	66
4.5.2	Particle size characterization.....	75
4.5.3	Effect of sintering additive.....	78
4.6	Conclusions.....	83
CHAPTER 5:	UNDOPED BZT CERAMICS AND BZT CERAMICS SYNTHESIZED AT LOW-SINTERING TEMPERATURE	84
5.1	Introduction.....	84
5.2	Review of previous work.....	85
5.3	Sintering Process.....	86
5.3.1	Normal sintering.....	86
5.3.2	Sintering additives	87
5.3.3	Two step sintering.....	88
5.4	Materials and methods	89
5.4.1	Preparation procedure of the Ba(Zr _x Ti _{1-x})O ₃ ceramics.....	89
5.4.2	Process with the sintering additive.....	90
5.4.3	Microscopic characterization.....	91
5.4.4	Densification analysis.....	91
5.4.5	Dielectric and piezoelectric properties characterization.....	91
5.5	Results and discussion.....	92
5.5.1	Microstructure of the Ba(Zr _x Ti _{1-x})O ₃ ceramics.....	92
5.5.2	Dielectric properties of the Ba(Zr _x Ti _{1-x})O ₃ ceramics.....	95
5.5.3	Effect of the sintering additive	97
5.6	Conclusions.....	101

TABLES OF CONTENTS (cont.)

CHAPTER 6: FREE-STANDING BARIUM ZIRCONATE TITANATE THICK FILM	102
6.1 Introduction.....	102
6.2 Free-standing thick films and concepts of a cantilever.....	103
6.3 Review of previous work.....	105
6.4 Materials and methods.....	109
6.4.1 Preparation of the sacrificial layer paste	109
6.4.2 Preparation of the BZT pastes.....	109
6.4.3 The BZT thick film fabrication	111
6.4.4 Pressing the thick films	112
6.4.5 Removal of the sacrificial layer.....	114
6.5 Results and discussion.....	114
6.5.1 Particle size distribution.....	115
6.5.2 Effect of sintering condition.....	116
6.5.3 Poling effect.....	120
6.5.3 Preliminary results.....	120
6.6 Conclusions.....	121
CHAPTER 7: CONCLUSIONS AND FUTURE WORK	122
7.1 Main conclusions.....	122
7.2 Future work.....	123
REFERENCES	125
VITAE	136

LIST OF FIGURES

Figure 2.1	Poling of ferroelectrics.	6
Figure 2.2	Classification of the crystallographic point groups.	6
Figure 2.3	Illustration of the ferroelectric phase transition.	7
Figure 2.4	Perovskite crystals in its (a) cubic, (b) tetragonal, and (c) rhombohedral states.	8
Figure 2.5	Directions of spontaneous polarization in (R) rhombohedral, (O) orthorhombic, (T) tetragonal and (C) cubic crystals of barium titanate.	9
Figure 2.6	Effect of electric field on a piezoelectric material, before and after the field is applied.	10
Figure 2.7	Phase diagram of PZT.	14
Figure 2.8	Property comparisons between PZT materials and lead-free materials: (a) dielectric permittivity as a function of the Curie temperature; (b) piezoelectric coefficient as a function of the Curie temperature.	15
Figure 2.9	Unit cell distortions of BaTiO ₃ single crystals.	16
Figure 2.10	Ion displacements in the cubic-tetragonal distortion in BaTiO ₃ .	17
Figure 2.11	Lattice constants of the nanoparticles (open circles and dash lines) and ceramics (solid lines) of Ba(Zr _x Ti _{1-x})O ₃ system.	18
Figure 2.12	Overview of various sample geometries prepared by sol-gel method.	19
Figure 2.13	Screen-printing process (a) and screen mesh (b).	24

LIST OF FIGURES (cont.)

- Figure 2.14 Examples of MEMS made by screen printing techniques with sacrificial layer (a) Gold cantilever beam (top) photograph and (bottom) SEM micrograph of AA cross section, (b) Screen-printed copper actuator, (left) top view photograph and (right) SEM micrograph of AA cross-section, (c) Free-standing AgPt resistor of cantilever type (left) top view and (right) SEM, (d) Photograph of a silver microchannel (left) and SEM micrograph of AA cross-section (right) and (e) multi-stage screen-printing Au/PZT/Au. 27
- Figure 2.14 **Cont.** Examples of MEMS made by screen printing techniques with sacrificial layer (a) Gold cantilever beam (top) photograph and (bottom) SEM micrograph of AA cross section, (b) Screen-printed copper actuator, (left) top view photograph and (right) SEM micrograph of AA cross-section, (c) Free-standing AgPt resistor of cantilever type (left) top view and (right) SEM, (d) Photograph of a silver microchannel (left) and SEM micrograph of AA cross-section (right) and (e) multi-stage screen-printing Au/PZT/Au. 28
- Figure 2.14 **Cont.** Examples of MEMS made by screen printing techniques with sacrificial layer (a) Gold cantilever beam (top) photograph and (bottom) SEM micrograph of AA cross section, (b) Screen-printed copper actuator, (left) top view photograph and (right) SEM micrograph of AA cross-section, (c) Free-standing AgPt resistor of cantilever type (left) top view and (right) SEM, (d) Photograph of a silver microchannel (left) and SEM micrograph of AA cross-section (right) and (e) multi-stage screen-printing Au/PZT/Au . 29
- Figure 3.1 Preparation procedure used in the BZT sol-gel process. 35
- Figure 3.2 Flow chart of the BZT thin film and the preparation conditions mainly used in this work. 36

LIST OF FIGURES (cont.)

Figure 3.3	Schematic diagram of the modified Michelson interferometer used for the determination of the piezoelectric coefficient.	38
Figure 3.4	TGA curves of the $\text{Ba}(\text{Zr}_x\text{Ti}_{1-x})\text{O}_3$ gels.	40
Figure 3.5	XRD results of the $\text{Ba}(\text{Zr}_{0.20}\text{Ti}_{0.80})\text{O}_3/ (111)\text{Pt}/\text{Ti}/\text{SiO}_2/\text{Si}$ annealed at various temperatures.	41
Figure 3.6	XRD patterns of the $\text{Ba}(\text{Zr}_x\text{Ti}_{1-x})\text{O}_3/ (111)\text{Pt}/\text{Ti}/\text{SiO}_2/\text{Si}$ annealed at 800 °C; $x=0.00-0.20$.	44
Figure 3.7	Lattice constants of the $\text{Ba}(\text{Zr}_x\text{Ti}_{1-x})\text{O}_3$ thin films.	45
Figure 3.8	Raman spectra of the $\text{Ba}(\text{Zr}_{0.05}\text{Ti}_{0.95})\text{O}_3$ thin film.	46
Figure 3.9	Raman spectra of the $\text{Ba}(\text{Zr}_{0.10}\text{Ti}_{0.90})\text{O}_3$ thin film.	46
Figure 3.10	Raman spectra of the $\text{Ba}(\text{Zr}_{0.15}\text{Ti}_{0.85})\text{O}_3$ thin film.	47
Figure 3.11	SEM cross-sectional image of the BaTiO_3 thin film.	48
Figure 3.12	SEM cross-sectional image of the $\text{Ba}(\text{Zr}_{0.05}\text{Ti}_{0.95})\text{O}_3$ thin film.	48
Figure 3.13	SEM cross-sectional image of the $\text{Ba}(\text{Zr}_{0.10}\text{Ti}_{0.90})\text{O}_3$ thin film.	49
Figure 3.14	SEM cross-sectional image of the $\text{Ba}(\text{Zr}_{0.15}\text{Ti}_{0.85})\text{O}_3$ thin film.	49
Figure 3.15	SEM cross-sectional image of the $\text{Ba}(\text{Zr}_{0.20}\text{Ti}_{0.80})\text{O}_3$ thin film.	50
Figure 3.16	FE-SEM planar image of the BaTiO_3 thin film.	50
Figure 3.17	FE-SEM planar image of the $\text{Ba}(\text{Zr}_{0.05}\text{Ti}_{0.95})\text{O}_3$ thin film.	51
Figure 3.18	FE-SEM planar image of the $\text{Ba}(\text{Zr}_{0.10}\text{Ti}_{0.90})\text{O}_3$ thin film.	51
Figure 3.19	FE-SEM planar image of the $\text{Ba}(\text{Zr}_{0.15}\text{Ti}_{0.85})\text{O}_3$ thin film.	52
Figure 3.20	FE-SEM planar image of the $\text{Ba}(\text{Zr}_{0.20}\text{Ti}_{0.80})\text{O}_3$ thin film.	52
Figure 3.21	AFM planar image of the BaTiO_3 thin film.	53
Figure 3.22	AFM planar image of the $\text{Ba}(\text{Zr}_{0.05}\text{Ti}_{0.95})\text{O}_3$ thin film.	53
Figure 3.23	AFM planar image of the $\text{Ba}(\text{Zr}_{0.10}\text{Ti}_{0.90})\text{O}_3$ thin film.	54
Figure 3.24	AFM planar image of the $\text{Ba}(\text{Zr}_{0.15}\text{Ti}_{0.85})\text{O}_3$ thin film.	54
Figure 3.25	AFM planar image of the $\text{Ba}(\text{Zr}_{0.20}\text{Ti}_{0.80})\text{O}_3$ thin film.	55

LIST OF FIGURES (cont.)

Figure 3.26	Variation of dielectric constant with frequency for the $\text{Ba}(\text{Zr}_x\text{Ti}_{1-x})\text{O}_3$ thin films with different compositions.	56
Figure 3.27	Variation of dielectric loss with frequency for the $\text{Ba}(\text{Zr}_x\text{Ti}_{1-x})\text{O}_3$ thin films with different compositions.	56
Figure 3.28	Variation of displacement with applied voltage for BaTiO_3 thin film.	58
Figure 3.29	Variation of displacement with applied voltage for the $\text{Ba}(\text{Zr}_{0.05}\text{Ti}_{0.95})\text{O}_3$ thin film.	58
Figure 3.30	Variation of displacement with applied voltage for the $\text{Ba}(\text{Zr}_{0.10}\text{Ti}_{0.90})\text{O}_3$ thin film .	59
Figure 3.31	Variation of displacement with applied voltage for the $\text{Ba}(\text{Zr}_{0.15}\text{Ti}_{0.95})\text{O}_3$ thin film .	59
Figure 4.1	Preparation procedure for the BZT powder.	65
Figure 4.2	Preparation procedure for the $\text{Ba}(\text{Zr}_{0.05}\text{Ti}_{0.95})\text{O}_3$ powder with sintering additive powder.	65
Figure 4.3	XRD patterns of the BaTiO_3 powder calcined at various temperatures.	67
Figure 4.4	XRD patterns of the $\text{Ba}(\text{Zr}_{0.20}\text{Ti}_{0.80})\text{O}_3$ calcined at various temperatures.	68
Figure 4.5	XRD patterns of the $\text{Ba}(\text{Zr}_x\text{Ti}_{1-x})\text{O}_3$ powders calcined at $1,100^\circ\text{C}$ for 2h.	69
Figure 4.6	Calculated lattice constants as a function of the $\text{Ba}(\text{Zr}_x\text{Ti}_{1-x})\text{O}_3$ calcined powders at various Zr contents.	70
Figure 4.7	Raman spectra of the $\text{Ba}(\text{Zr}_{0.05}\text{Ti}_{0.95})\text{O}_3$ powder calcined at $1,100^\circ\text{C}$ for 2 h.	71
Figure 4.8	Raman spectra of the $\text{Ba}(\text{Zr}_{0.10}\text{Ti}_{0.90})\text{O}_3$ powder calcined at $1,100^\circ\text{C}$ for 2 h.	71
Figure 4.9	Raman spectra of the $\text{Ba}(\text{Zr}_{0.15}\text{Ti}_{0.85})\text{O}_3$ powder calcined at $1,100^\circ\text{C}$ for 2 h.	72

LIST OF FIGURES (cont.)

Figure 4.10	CBED patterns (a) and simulated (b) images for [102] zone axis of Ba(Zr _{0.05} Ti _{0.95})O ₃ powder.	73
Figure 4.11	CBED patterns (a) and simulated (b) images for [001] zone axis of Ba(Zr _{0.05} Ti _{0.95})O ₃ powder.	74
Figure 4.12	Particle size distribution of the BaTiO ₃ calcined powder.	76
Figure 4.13	Particle size distribution of the Ba(Zr _{0.05} Ti _{0.95})O ₃ calcined powder.	76
Figure 4.14	Particle size distribution of the Ba(Zr _{0.10} Ti _{0.90})O ₃ calcined powder.	77
Figure 4.15	Particle size distribution of the Ba(Zr _{0.15} Ti _{0.85})O ₃ calcined powder.	77
Figure 4.16	Particle size distribution of the Ba(Zr _{0.20} Ti _{0.80})O ₃ calcined powder.	78
Figure 4.17	XRD patterns of Ba(Zr _{0.05} Ti _{0.95})O ₃ powder calcined at 1,100 ° C for 2 h and Ba(Zr _{0.05} Ti _{0.95})O ₃ powder with 1.5 wt.% Li ₂ O calcined at 700 ° C for 10 h.	79
Figure 4.18	TGA patterns of Ba(Zr _{0.05} Ti _{0.95})O ₃ gel and the Ba(Zr _{0.05} Ti _{0.95})O ₃ with 1.5 wt% Li ₂ O powder calcined at 700 ° C for 10 h.	80
Figure 4.19	Raman spectra of the Ba(Zr _{0.05} Ti _{0.95})O ₃ powders calcined at 1,100 °C for 2 h and the Ba(Zr _{0.05} Ti _{0.95})O ₃ powders with 1.5 wt.% Li ₂ O calcined at 700 ° C for 10 h.	81
Figure 4.20	Particle size distribution of the calcined Ba(Zr _{0.05} Ti _{0.95})O ₃ powders.	82
Figure 4.21	Particle size distribution of the calcined Ba(Zr _{0.05} Ti _{0.95})O ₃ with 1.5 wt.% Li ₂ O powder.	82
Figure 5.1	Preparation procedure of the BZT ceramic.	89

LIST OF FIGURES (cont.)

Figure 5.2	Preparation procedure of the Ba(Zr _{0.05} Ti _{0.95})O ₃ with 1.5 % wt. Li ₂ O ceramic.	90
Figure 5.3	SEM image of the BaTiO ₃ ceramic.	92
Figure 5.4	SEM image of the Ba(Zr _{0.05} Ti _{0.95})O ₃ ceramic.	93
Figure 5.5	SEM image of the Ba(Zr _{0.10} Ti _{0.90})O ₃ ceramic.	93
Figure 5.6	SEM image of the Ba(Zr _{0.15} Ti _{0.85})O ₃ ceramic.	94
Figure 5.7	SEM image of the Ba(Zr _{0.20} Ti _{0.80})O ₃ ceramic.	94
Figure 5.8	Variations of the dielectric constant with temperature of Ba(Zr _x Ti _{1-x})O ₃ ceramics.	96
Figure 5.9	SEM image of Ba(Zr _{0.05} Ti _{0.95})O ₃ ceramic.	98
Figure 5.10	SEM image of Ba(Zr _{0.05} Ti _{0.95})O ₃ with 1.5 wt.% Li ₂ O ceramic.	98
Figure 5.11	Variations of the dielectric constant with temperature for Ba(Zr _{0.05} Ti _{0.95})O ₃ without and with 1.5 wt% Li ₂ O.	100
Figure 6.1	Thick film procedure with sacrificial layer deposited onto a substrate at the beginning step and removed afterwards at a final step.	104
Figure 6.2	Transversal vibration (a) and longitudinal vibration (b).	104
Figure 6.3	Flow chart of the preparation of PZT thick-film actuator.	106
Figure 6.4	The PZT thick film geometry with various shapes.	106
Figure 6.5	Flow chart of the thick film elaborating.	111
Figure 6.6	Patterned screen for (a) the tracks of gold (b) the layer sacrificial (c) the lower electrode (connected to conductive tracks), (d) the layer piezoelectric and (e) the top gold electrode.	112
Figure 6.7	Procedure of pressing thick film.	113
Figure 6.8	Samples encapsulated in polymer film.	113
Figure 6.9	The pressing machine.	114
Figure 6.10	Particle size distribution of group A powder.	115
Figure 6.11	Particle size distribution of group B powder.	115
Figure 6.12	Particle size distribution of group C powder.	116

LIST OF FIGURES (cont.)

Figure 6.13	The BZT (group A) cantilever of the element of dimension of 10x2 mm thickness ~ 60 μm .	117
Figure 6.14	A picture and a sketch of the element of dimension of 8x2 mm showing the cracks at the corners of the element.	118
Figure 6.15	The thick film made from group B paste sintered at various sintering conditions (a) 850 °C for 0.5 h, (b) 900 °C for 0.1 h, (c) 900 °C for 0.5 h and (d) 900 °C for 2 h.	118
Figure 6.16	The Group C thick films sintering at 850 °C with a rate of 15 °C / min for 0.5 h.	119

LIST OF TABLES

Table 2.1	Vibration modes of piezoelectric materials.	12
Table 2.2	Advantages and disadvantages of various techniques for processing of ferroelectric films.	21
Table 2.2	Advantages and disadvantages of various techniques for processing of ferroelectric films.	22
	Cont.	
Table 2.3	Characteristics of conventional screen meshes.	25
Table 3.1	Summary of the Bragg planes, 2θ , d_{hkl} , and lattice constants of the $\text{Ba}(\text{Zr}_{0.20}\text{Ti}_{0.80})\text{O}_3$ thin film annealed at 800 °C.	42
Table 3.2	Summary of the Bragg planes, 2θ , d_{hkl} , and lattice constants of the $\text{Ba}(\text{Zr}_{0.20}\text{Ti}_{0.80})\text{O}_3$ thin film annealed at 900 °C.	42
Table 3.3	Summary of the Bragg planes, 2θ , d_{hkl} , and lattice constants of the $\text{Ba}(\text{Zr}_{0.20}\text{Ti}_{0.80})\text{O}_3$ thin film annealed at 1000 °C.	43
Table 3.4	The dielectric constant and dielectric loss measured at 1 kHz for the $\text{Ba}(\text{Zr}_x\text{Ti}_{1-x})\text{O}_3$ thin films.	57
Table 3.5	The clamped values of the d_{33} coefficient for the poled $\text{Ba}(\text{Zr}_x\text{Ti}_{1-x})\text{O}_3$ thin films.	57
Table 4.1	The crystalline size of the $\text{Ba}(\text{Zr}_x\text{Ti}_{1-x})\text{O}_3$ powders.	75
Table 5.1	Density and grain size of the $\text{Ba}(\text{Zr}_x\text{Ti}_{1-x})\text{O}_3$ ceramics.	95
Table 5.2	Summary of the room-temperature dielectric properties measured at 1 kHz of the $\text{Ba}(\text{Zr}_x\text{Ti}_{1-x})\text{O}_3$ ceramics.	95
Table 5.3	Summary of the electromechanical properties of the $\text{Ba}(\text{Zr}_x\text{Ti}_{1-x})\text{O}_3$ ceramics	97
Table 5.4	Density and grain size of the $\text{Ba}(\text{Zr}_{0.05}\text{Ti}_{0.95})\text{O}_3$ ceramics, without and with the sintering additive.	99
Table 5.5	Room-temperature dielectric properties of the $\text{Ba}(\text{Zr}_{0.05}\text{Ti}_{0.95})\text{O}_3$ ceramics, without and with the sintering additive.	99

LIST OF TABLES (cont.)

Table 5.6	Electromechanical properties of the Ba(Zr _{0.05} Ti _{0.95})O ₃ ceramics, without and with the sintering additive.	100
Table 6.1	Summary of sintering conditions of group A thick films.	117
Table 6.2	Summary of sintering conditions of group C thick films.	119
Table 6.3	Electromechanical characterization of BZT cantilever.	120

SYMBOLS

<p>A = Electrode Area</p> <p>C = Capacitance</p> <p>S_{ij} = Strain Tensor</p> <p>D = Dielectric Displacement</p> <p>d = Thickness</p> <p>d_{ij} = Piezoelectric Stress Coefficient</p> <p>d_{ac} = Surface Displacement</p> <p>E = Electric Field</p> <p>E_c = Coercive Field</p> <p>F = Force</p> <p>f = Frequency</p> <p>g = Piezoelectric Strain Coefficient</p> <p>I = Light Intensity</p> <p>k = Electrical coupling Factor</p> <p>m = Electric Current</p> <p>P = Polarization</p> <p>P_r = Remanent Polarization</p> <p>P_s = Saturation Polarization</p> <p>2ME = 2-methoxyethanol</p> <p>CSD = Chemical Solution Deposition</p> <p>PLD = Pulsed Laser Deposition</p> <p>PZT = $\text{Pb}(\text{Zr}_x\text{Ti}_{1-x})\text{O}_3$</p> <p>BZT = $\text{Ba}(\text{Zr}_x\text{Ti}_{1-x})\text{O}_3$</p> <p>FeRAM = Ferroelectric Random Access Memory</p> <p>DRAM = Dynamic Random Access Memory</p> <p>MLCC = Multilayer Ceramic Capacitor</p>	<p>Q = Charge</p> <p>R = Resistance</p> <p>$\tan\delta$ = Loss Tangent</p> <p>T = Temperature</p> <p>T_c = Curie Temperature</p> <p>t = Time</p> <p>V = Voltage</p> <p>U = Thermal Energy</p> <p>Z = Acoustic Impedance</p> <p>ε = Permittivity of a Medium</p> <p>ε_0 = Permittivity of a Free Space</p> <p>ε_r = Relative Permittivity</p> <p>σ_{ij} = Stress Tensor</p> <p>γ = Thermal Expansion</p> <p>λ = wavelength</p> <p>ω = Angular Frequency</p> <p>χ = Electric susceptibility</p>
--	--

SYMBOLS (Cont.)

XRD	=	X-ray Diffraction
SEM	=	Scanning Electron Microscopy
TEM	=	Transmission Electron Microscopy
LPSA	=	Laser Particle Size Analyzer
TGA	=	Thermogravimetric analyzer

CHAPTER 1

INTRODUCTION

1.1 Statement of the problem

In the development of micro-electronic devices, for example, micromachined sensors and piezo-actuators based on the micro-electromechanical systems (MEMS), ferroelectric materials have been integrated into miniaturization of their components for decades. Perovskite lead-zirconate-titanate or PZT family is the most well-known material of excellent electromechanical property that has long been recognized to meet industrial standards. As can be seen, a typical ingredient of the PZT material is the lead (Pb) which is toxic. Accumulations of the lead caused by the manufacturing during the production process and the recycling procedure of the products or devices in which it is incorporated lead to a controversial argument all over the industrial communities concerning the environmental safety and, consequently, discontinuing of the use of the lead-based material. The PZT is included, unfortunately. (U.S Department of Health and Human Services, Public Health Service Agency for Toxic Substances and Disease and Registry, 2007; Official Journal of the European Union, 2003).

According to the statement mentioned above, the perovskite lead-free materials whose physical and electromechanical properties are superior or, at least, equivalent to those of PZT are highly desirable. Recently, an interest in barium zirconate titanate or BZT family has risen because of the chemical stability of the perovskite unit cell induced by the substitution of a Ti^{4+} by a Zr^{4+} . In addition, a larger ionic size of the Zr^{4+} effectively expands the perovskite lattice of the original BaTiO_3 one. The lattice distortion leads to a high strain level and good piezoelectric effect in both single crystals and ceramics (Wu, Wu and Chen, 1996; Yu, Guo and Bhalla, 2000; Jiwei *et al.*, 2004).

The present work therefore considers BZT ($\text{Ba}(\text{Zr}_x\text{Ti}_{1-x})\text{O}_3$) material, whose chemistry involving the fabrication and some physical properties are well-known (Wu, Wu and Chen, 1996; Jiwei *et al.*, 2004), promising as alternative choices to PZT. However, a main concern is involving with the development of the material properties, in particular, piezoelectricity of the BZT which is still inferior to that of the PZT.

Basically, the physical properties of the perovskite-type materials strongly depend on their stoichiometry and morphology which are closely related to the electromechanical behavior of the materials. For the fabrication of the piezoelectric BZT bulk, powder and films in this work, different preparation methods and associated factors have been used. The sol-gel process is chosen for fabricating thin film. The same sol-gel route will be also used to produce the BZT powder whose crystal defects can be minimized. Solid-state reaction and its appropriate calcining and sintering conditions are chosen for, especially, synthesizing BZT ceramic at low-sintering temperature. A newly developed technology of free-standing PZT thick film has been firstly validated for fabricating free-standing BZT in this work.

1.2 Thesis outline

The thesis consists of seven chapters. In the present chapter, the statement of the problem is addressed, including the research objectives.

Chapter 2 presents the background of the piezoelectricity and related effects. Methods of the fabrication of perovskite materials of various forms are described. General background of thick films technology is given.

Chapter 3 describes the realizable synthetic route, acetic sol-gel, for production of BZT thin films. The thin films have been deposited using the spinning method. The material properties of the thin film have been presented and thoroughly discussed.

Chapter 4 describes the fabrication of homogeneous BZT powder. Methods for characterizing the properties of the powder and an effect of sintering additive on BZT powder are also presented.

Chapter 5 presents the fabrication and characterization of BZT ceramics without and with sintering additive. The BZT ceramic synthesized at low-sintering temperature and its property are completely reported in this chapter.

Chapter 6 presents the background of thick-film fabricating technique, focusing on the free-standing geometry. The application of the free-standing fabricating technique to BZT thick film is validated in this chapter.

Chapter 7 concludes the findings presented in the present work. The prognosis for future work and difficulties arisen during the course of study are addressed.

1.3 Objectives of research

1. To develop, through qualified sol-gel route, uniform thin films, powders, and ceramics at low sintering-temperature of $\text{Ba}(\text{Zr}_x\text{Ti}_{1-x})\text{O}_3$, $x = 0.00, 0.05, 0.10, 0.15$ and 0.20 .
2. To validate procedures for fabricating BZT thick film.

CHAPTER 2

BACKGROUND THEORY

This chapter presents the background of the piezoelectricity and related effects. Several techniques for the fabrications of perovskite materials of various forms are described. Finally, background of thick films technology is addressed.

2.1 Introduction to piezoelectricity

2.1.1 Polarity, polarization behavior and poling process

Dielectric materials are electrical insulators. It can be grown in single crystal or polycrystalline forms. Those substances in which the centers of positive and negative charges do not coincide will form an electric dipole. The application of an electrical field modifies the distribution of charges in each molecule in such, that dipole moments are induced. The dipole moment averaged over the volume is the polarization, denoted by P . The polarization is thus presented in a polar crystal or polycrystalline material. The polarization P and the overall charge neutrality of dielectrics in an external field E is described by (William and Callister, 2005)

$$D = \varepsilon_0 E + P \quad (2.1)$$

Considering a simple parallel plate capacitor filled with dielectrics, if the applied voltage is kept constant ($E = \text{constant}$ short circuit condition), additional free charges need to flow into the system to increase D (electrical displacement). If the charges on the plates are kept constant ($D = \text{constant}$ open circuit condition), the field E and the voltage between the plates will therefore decrease according to equation (2.1).

For many dielectric materials, P is proportion to the electric field in a linear approximation (William and Callister, 2005) by

$$P = \varepsilon_0 \chi E \quad \text{or} \quad D = \varepsilon_0 \varepsilon_r E = \varepsilon E \quad (2.2)$$

Where the electric susceptibility, χ is related to the dielectric constant or relative permittivity (ε_r) by $\chi = \varepsilon_r - 1$. ε and ε_0 are the permittivity of the material and free space (8.854×10^{-12} F/m), respectively.

When an alternating current is applied to a dielectric material, the dipoles are no longer able to follow the oscillation of the electric field at a certain frequency. This result is energy dissipation, defined as the dielectric loss or $\tan \delta$ or loss tangent or dissipation factor (D)

$$D = \tan \delta = \frac{\varepsilon''}{\varepsilon'} = \frac{\varepsilon_r''}{\varepsilon_r'} \quad (2.3)$$

The dielectric material that is polarized will exhibit polarity. Polar materials are always piezoelectric as described in next topic (2.1.3). If the direction of the dipole can be reversed by means of an external electric field, the material is called ferroelectric. Nevertheless, we need to apply a high DC field to the crystal or polycrystalline material. The details will be addressed in next paragraph.

Poling is a process by which a DC electric field is applied to a specimen of multi-domain crystal to switch the direction of electric dipoles. An electric field of the order of kV/mm is applied to the crystal to align the internal electrical dipoles in a single orientation, as shown in figure 2.1. The permanent dipoles begin to move towards the direction of an externally applied field. When the electric field is removed, some dipole moments rotate back, but incompletely, resulting in a remnant polarization. At this point the materials exhibit both piezoelectric and pyroelectric effects. The piezoelectricity is the phenomenon of interest in this section. In order to know what material is piezoelectric, the concept of

the crystal symmetry is introduced as extensively reported by Moulson and Herbert, (1990), Ikeda (1990), Uchino (1997) and Böttger (2005).

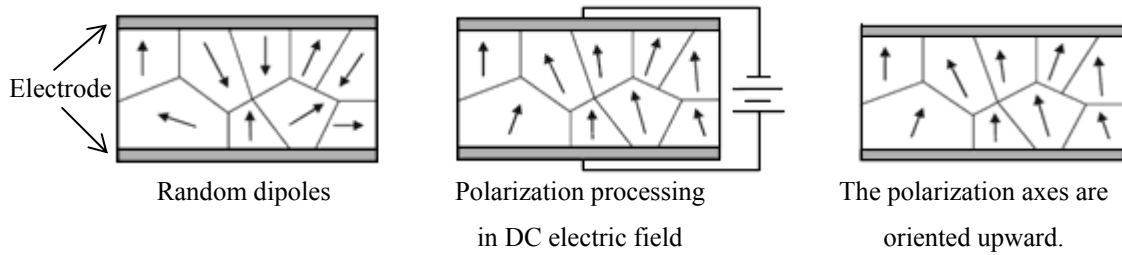


Figure 2.1 Poling of ferroelectrics (Böttger, 2005).

According to the crystal symmetry with respect to a point, classifications of the crystal can be made as illustrated in figure 2.2. From 32 crystallographic point groups or crystal classes, 21 are non-centrosymmetric. Of these 21, 20 are piezoelectric. Of these 20, 10 are pyroelectric. Of these 10, 5 are ferroelectric.

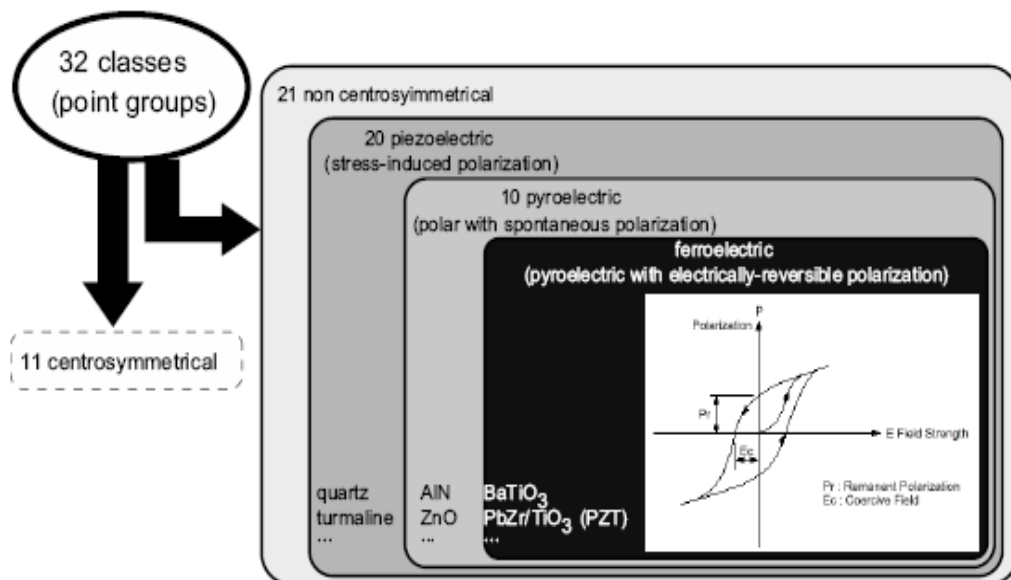


Figure 2.2 Classification of the crystallographic point groups (Böttger, 2005).

It is important to point out that all ferroelectrics are piezoelectrics. In principle, a ferroelectric phase transition is a structure phase transition which is a spontaneous polarization, polarization in the absence of an electric field; this spontaneous polarization is a result of the positioning of the positive and negative charges within the unit cell of the material. The ferroelectric phase transition occurs at the ferroelectric Curie temperature, denoted by T_C . Above T_C the crystal is centrosymmetric paraelectric state. Below T_C , the crystal is non-centrosymmetric characteristics, which result in the ferroelectric state. At T_C , the dielectric constant (ϵ) exhibits a maximum value, as shown in figure 2.3 Above T_C , the relationship between ϵ and the temperature follows the Curie-Weiss law:

$$\epsilon = \frac{C}{T - T_0} \quad (2.4)$$

Where C is the Curie constant and T_0 is the Curie-Weiss temperature.

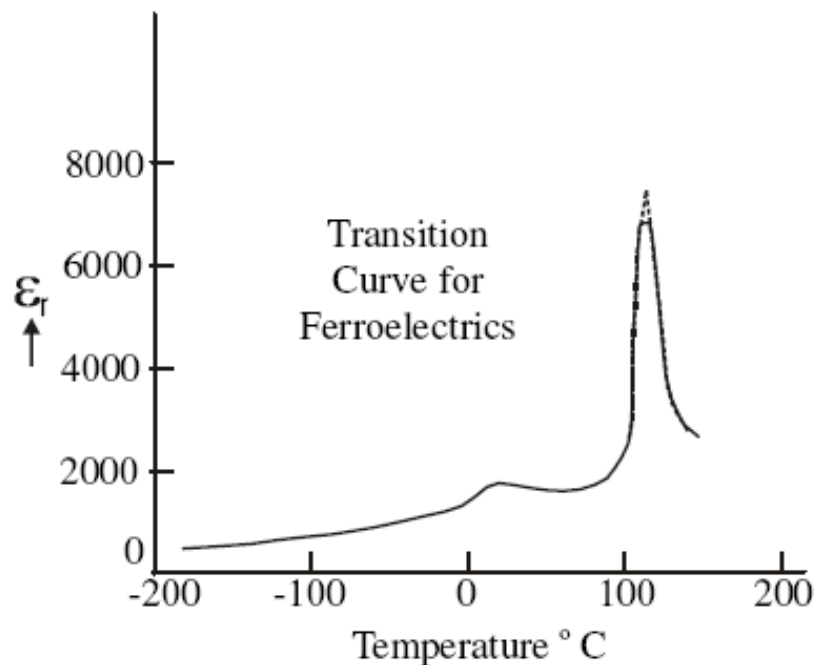


Figure 2.3 Illustration of the ferroelectric phase transition (Swartz, 1990).

2.1.2 Perovskite-type materials

The perovskite structure allows the non-zero polarization in the unit cell and common occurrence of ferroelectric in this structure. The perovskite ABO_3 structure consisting of A atoms are located on the crystal corner which are monovalent or divalent metal, such as barium or lead. The B atom located at the centre of the unit cell is a tetravalent or pentavalent metal, such as zirconium or titanium atoms. The oxygen atoms appear at the face centers, respectively. The perfect perovskite crystal is cubic as illustrated in figure 2.4(a). It is the shape of paraelectric state. Below the Curie temperature the cubic lattice is tetragonal lattice distortion (figure 2.4 (b)) which is manifest ferroelectric phase or some material display a rhombohedral ferroelectric phase (figure 2.4 (c)) (Uchino, 1997).

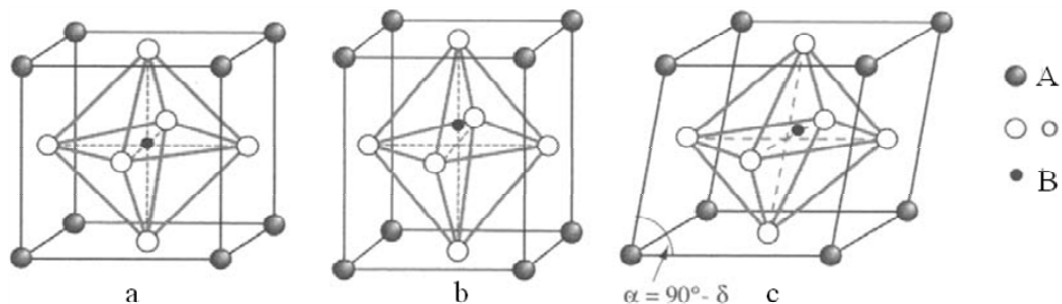


Figure 2.4 Perovskite crystals in its (a) cubic, (b) tetragonal, and (c) rhombohedral states (Damjanovic, 2005).

The polarization is only allowed along certain directions depending on the crystallographic class as an example showed in figure 2.5. Not all domains will be precisely aligned to the poling direction but will be as close as the crystal orientation permits if given sufficient energy and time.

The greater the number of polarizable directions the closer the polar axes can align to the poling field to increase the piezoelectric properties. In polycrystalline piezoelectrics the maximum attainable polarization can be given as a fraction of the single crystal value. For a tetragonal perovskite, there are six polar

directions giving a fraction of 0.83. In practice, the value is limited by internal strains that inhibit 90° domain switching. The switching of 180° domain can be almost totally accomplished (Moulson and Herbert, 1990).

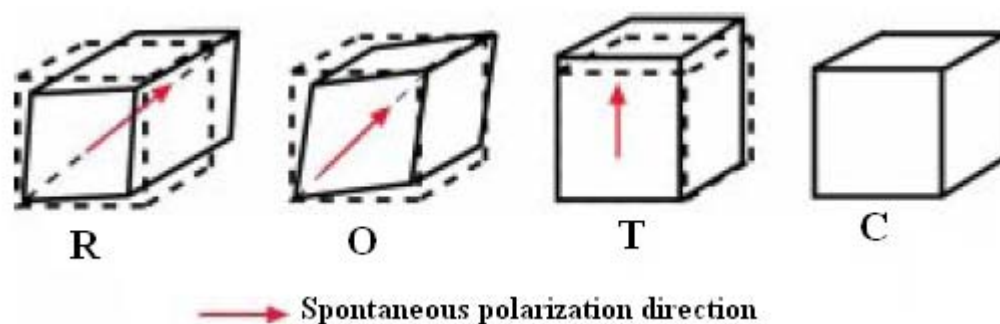


Figure 2.5 Directions of spontaneous polarization in (R) rhombohedral, (O) orthorhombic, (T) tetragonal and (C) cubic crystals of barium titanate (Moulson and Herbert, 1990).

2.1.3 Piezoelectric effect

Thermodynamics predicts the existence of a direct and an inverse effect for piezoelectric material. Direct effect is considered to be the generation of charge by an applied mechanical stress, while the inverse effect is the generation of strain by an applied field. Since there are two of each type; namely, mechanical stress (T) and strain (S) and electrical displacement (D) and field (E), there are four different piezoelectric coefficients. In the present case, our interest is centered on the dependence of the mechanical strain on the electric field. This dependence is described by the piezoelectric d coefficient.

The constitutive equations for piezoelectric materials describing the effects with respect to electrical and mechanical properties are presented in the following equations:

$$D = dT + \varepsilon^T E \quad (2.5)$$

Where D , E and T are the electric displacement, the electric field, (V/m), and the mechanical stress (N/m²), respectively. The constant ε^T is a dielectric constant at constant stress (F/m) and d the piezoelectric coefficient.

The second piezoelectric form is the converse effect, which is able to convert an applied electrical potential into mechanical strain energy.

$$S = s^E T + dE \quad (2.6)$$

Where S is the mechanical strain, and s^E is elastic compliance at constant electric field (m/N).

There are two important types of the piezoelectric coefficient: the longitudinal (d_{33}) and transverse (d_{31}) piezoelectric coefficients (figure 2.6). When the electric field is applied to the original volume of a material, the original volume transforms into the inner volume. This has created the extension in the z direction (poled direction), while contraction in x - or y -axis directions, due to constant sample volume. From equations (2.5) and (2.6) the direct piezoelectric effect is responsible for the materials ability to function as a sensor while the converse piezoelectric effect is accountable for its ability to function as an actuator.

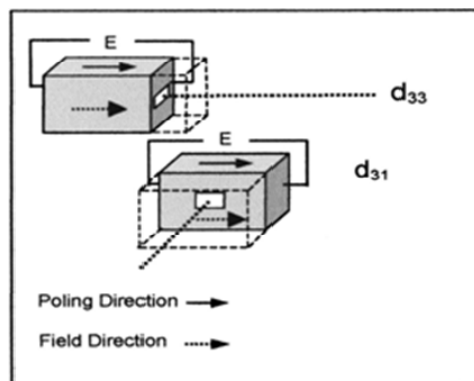


Figure 2.6 Effect of electric field on a piezoelectric material, before and after the field is applied (outer and inner cubes, respectively) (Modified from Masys *et al.*, 2003).

There are two independent and equivalent techniques of measuring piezoelectric coefficient in a material. First, measuring of the direct piezoelectric effect. A probe for observing a charge amount produced by imposing a load is directly placed on the material and the d_{33} can be extracted. Second, a measurement of the reverse piezoelectric effect. The probe for observing the displacement induced by applied electric field is used. The latter is more difficult, however, more precise.

It is common to measure the electromechanical coupling coefficient, k of a piezoelectric material. It is defined as follows:

$$k^2 = \text{stored mechanical energy}/\text{input electrical energy}$$

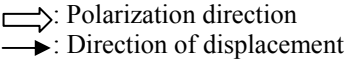
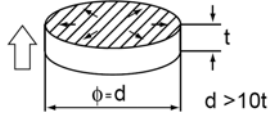
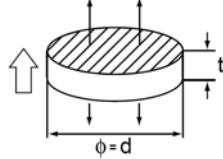
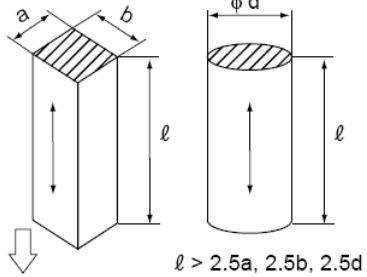
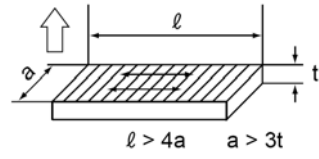
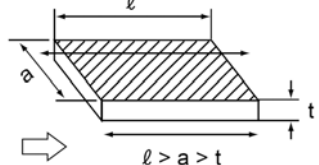
or $k^2 = \text{stored electrical energy}/\text{input mechanical energy}$

In practice, the electromechanical coupling coefficient is often defined by (Ikeda, 1990):

$$k^2 = \frac{d^2}{\epsilon^T s^E} \quad (2.7)$$

The electromechanical coupling coefficient for various geometries of piezoelectric materials is listed in table 2.1. The electromechanical coupling coefficient can be determined for various modes of vibration using one of the two following methods. First, the static method is the original measurement using the direct effect. In detail, putting a weight on a material and observing the charge generated by charge detector such as an electrometer. This method is rather indeterminate since it may depend on how much of the charge generated has leaked off during the measurement.

Table 2.1 Vibration modes of piezoelectric materials.

Mode of Vibration	Shape 	Electromechanical Coupling Coefficient
Radial	Disk 	$k_p^2 \cong \left(2.51 \cdot \frac{f_a - f_r}{f_a} \right) - \left(\frac{f_a - f_r}{f_a} \right)^2$
Thickness extension	Disk 	$k_t^2 = \frac{\pi}{2} \cdot \frac{f_r}{f_a} \cot \left(\frac{\pi}{2} \cdot \frac{f_r}{f_a} \right)$
Longitudinal length	Cylinder 	$k_{33}^2 = \frac{\pi}{2} \cdot \frac{f_r}{f_a} \cot \left(\frac{\pi}{2} \cdot \frac{f_r}{f_a} \right)$
Transverse length	Rectangular plate 	$\frac{k_{31}^2}{1 - k_{31}^2} = -\frac{\pi}{2} \cdot \frac{f_a}{f_r} \cot \left(\frac{\pi}{2} \cdot \frac{f_a}{f_r} \right)$
Thickness shear	Rectangular plate 	$k_{15}^2 = \frac{\pi}{2} \cdot \frac{f_r}{f_a} \cot \left(\frac{\pi}{2} \cdot \frac{f_r}{f_a} \right)$

(PIEZOTITE[®], 2008; Ferroperm Piezoceramics, 2003).

The second method is an easy and accurate method to evaluate the k -value. It is by measuring the resonance and anti-resonance frequencies which relate to the k -value (Mason and Jaffee, 1954). In this method, if an AC voltage of varying frequency is applied to a piezoelectric ceramic of a certain shape (as listed in Table 2.1), there is a specific frequency at which the ceramic produces a very strong vibration. This frequency is called the resonance frequency which depends on the shape, orientation of polarization, and the direction of the electric field. Each vibration mode has a unique resonance, f_r (the impedance is at a minimum) and anti-resonance f_a (oppositely, the impedance is at a maximum).

The effective electromechanical coupling k_{eff} is frequently used to express the electromechanical coupling of an arbitrary resonator regardless of its shape as given by:

$$k_{eff}^2 = \frac{f_a^2 - f_r^2}{f_r^2} \quad (2.8)$$

Where f_r is the resonance frequency of piezoelectric material at minimum impedance while the current is at a maximum. Oppositely, the f_a corresponds to the frequency at the lowest current value and at the highest impedance.

2.2 Common piezoceramics

Piezoelectric ceramics are a type of multi-crystal dielectric with a high dielectric. Important piezoceramic materials are introduced for MEMS (Micro-Electro-Mechanical System), sensors, actuator and transducers. (Tadigadapa and Mateti, 2009) and are listed into two main groups as below.

1) Lead-based Piezoceramics such as lead zirconate titanate (PZT)

Solid-solution of PbTiO_3 - PbZrO_3 (PZT) is one of the most important ferroelectric and piezoelectric materials (Jaffe, Cook and Jaffe, 1971). PZT adopts a distorted version of perovskite structure as illustrated in figure 2.7, the

structural changes at the Curie temperature and the morphotropic phase boundary (MPB), separating the rhombohedral and tetragonal structure at about 45 mole percent PbTiO_3 . For large polarization, the composition near the MPB is preferred. It is believed that the tetragonal phase with six equivalent domain states (in the $\langle 100 \rangle$ directions) and the rhombohedral phase with eight domain states (in the $\langle 111 \rangle$ directions) co-exist for these compositions, resulting in 14 possible different directions of alignment over a wide temperature range (Jaffe, Cook and Jaffe, 1971).

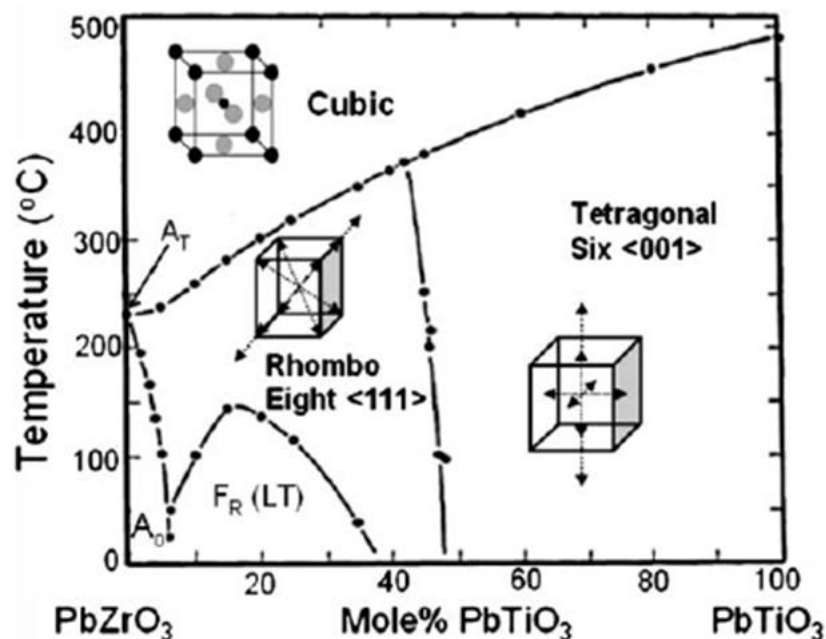
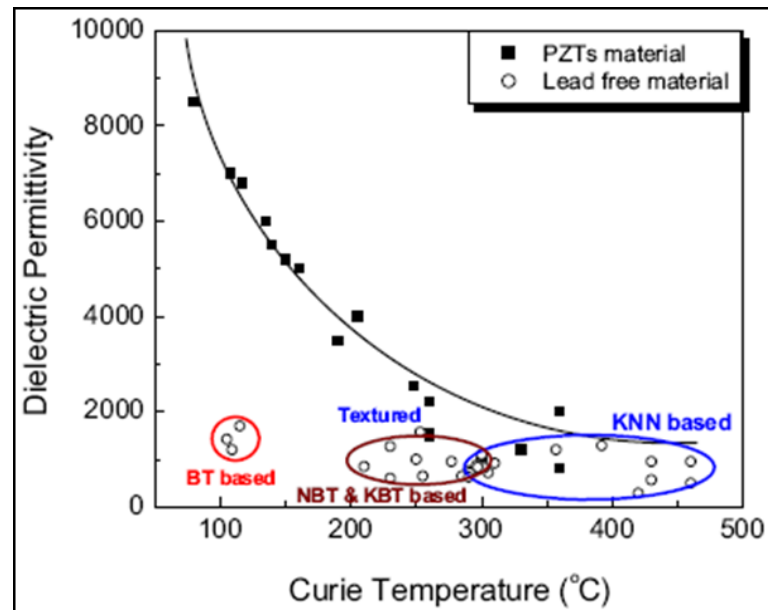


Figure 2.7 Phase diagram of PZT (Jaffe, Cook and Jaffe, 1971).

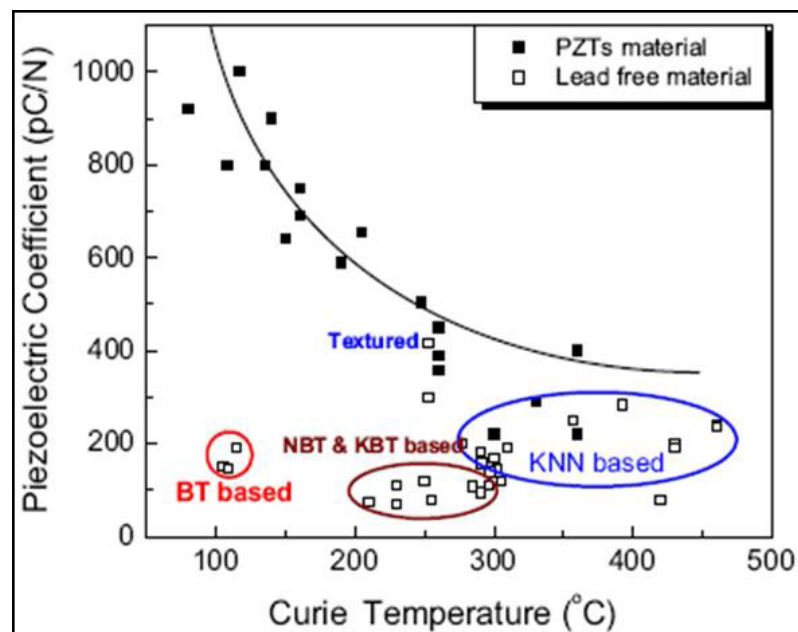
The lone pair electron may play an important role in stabilizing ferroelectric structure. Thus the ferroelectric transition temperature and spontaneous distortion of PbTiO_3 is much larger than BaTiO_3 (Jaffe Cook and Jaffe, 1971).

2) Non-lead or lead-free piezoceramics

Lead-free piezoceramics such as KNN base, NBT and KBT base, and BaTiO_3 base was shown in figure 2.8 (a and b) the piezoelectric coefficient of BaTiO_3 base ceramic is lower than PZT, but those values are compared to the others.



(a)



(b)

Figure 2.8 Property comparisons between PZT materials and lead-free materials: (a) dielectric permittivity as a function of the Curie temperature; (b) piezoelectric coefficient as a function of the Curie temperature (Shrout and Zhang, 2007).

2.3 Barium titanate and barium zirconate titanate systems

2.3.1 Barium titanate ($BaTiO_3$) system

Barium titanate or $BaTiO_3$ ceramic is one of the most intensively studied ferroelectric materials and used in various applications such as electro-optic and electronic component. $BaTiO_3$ has an $A^{II}B^{IV}O_3$ type perovskite structure. A general unit cell of a cubic perovskite. This material is interesting due to it has a series of phase transitions (cubic to tetragonal to orthorhombic to rhombohedral) as shown in figure 2.9. Below the Curie point ($\sim 130^\circ\text{C}$), the structure is slightly distorted to the tetragonal form with a dipole moment along the c direction. Other transformations occur at temperatures close to 0°C and -90°C below 0°C , the unit cell is orthorhombic with the polar axis parallel to a face diagonal and it is rhombohedral with the polar axis along a body diagonal below -90°C .

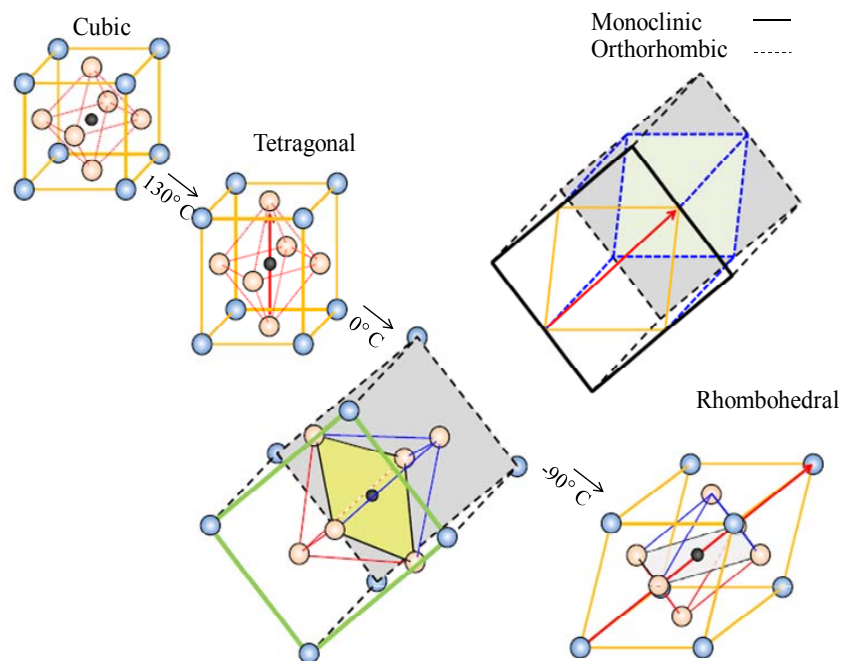


Figure 2.9 Unit cell distortions of $BaTiO_3$ single crystals (Kay and Vousdan, 1949).

A consideration of the ion displacements accompanying the cubic-tetragonal transformation can give insight into how the spontaneous polarization might be coupled from unit cell to unit cell. X-ray studies have established that in the tetragonal form, taking the 4 central (B) oxygen ions in the cubic phase as origin, the other ions are slightly shifted was shown in figure 2.10.

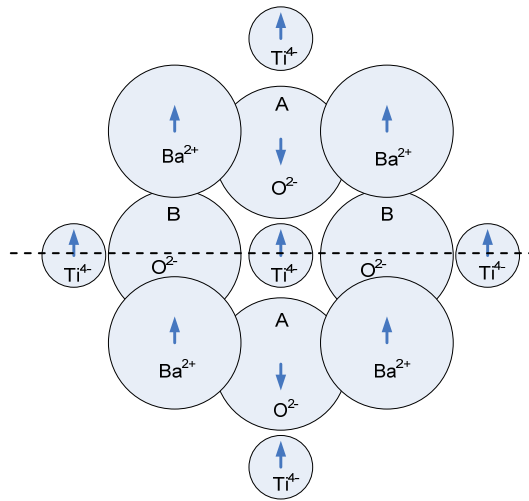


Figure 2.10 Ion displacements in the cubic-tetragonal distortion in BaTiO₃
(Moulson and Herbert, 1990).

2.3.2 Barium zirconate titanate (Ba(Zr_xTi_{1-x})O₃) system

BaTiO₃ based-material is used as the dielectric and original solid solution for many other ceramic systems such as Ba_xSr_{1-x}TiO₃ (BST) and Ba(Zr_xTi_{1-x})O₃ (BZT). Recently, BZT is a new dielectric as a possible alternative to BST for applications in electronic devices. Perovskite BZT has been studied for areas requiring high permittivity such as dynamic random access memory (DRAM), multilayer ceramic capacitor (MLCC), ferroelectric random access memory (FeRAM), etc. It is realized that the Zr substitution in BaTiO₃ decreases and shifts the Curie temperature below room temperature. The Zr⁴⁺ ion is more chemically stable than Ti⁴⁺ and has larger ionic size to expand the perovskite lattice. It is also reported that an increase in Zr content induces a reduction in the average grain size, decrease in dielectric constant (ϵ_r) and maintains a low and stable leakages current. (Dobal *et al.*, 2001; Dixit *et al.*, 2002; Pontes *et al.*, 2004 and Qi *et al* 2006). The well-known

crystal phase transitions in $\text{Ba}(\text{Zr,Ti})\text{O}_3$ material is as shown in figure 2.11 (Qi *et al.*, 2006).

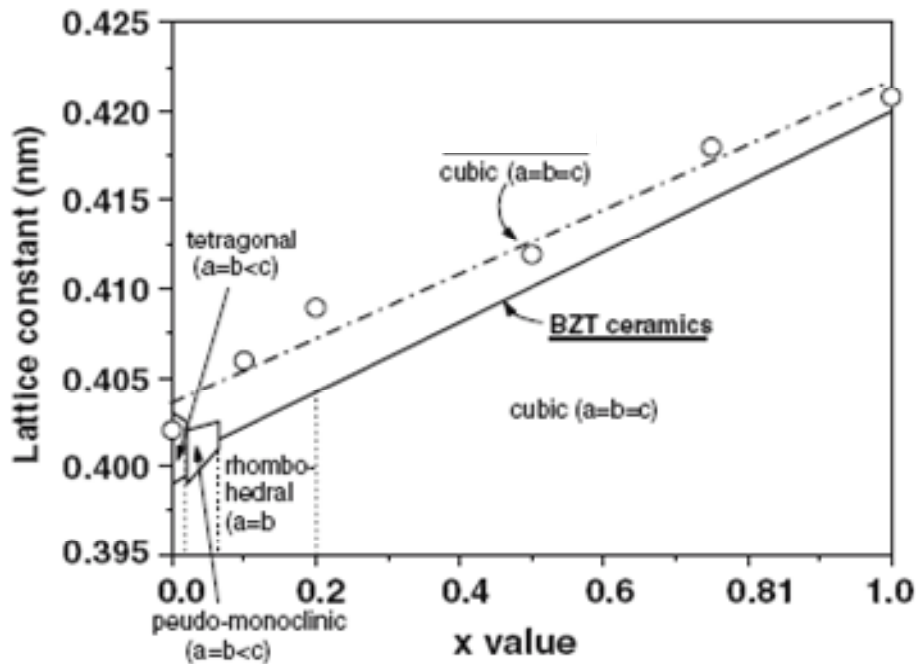


Figure 2.11 Lattice constants of the nanoparticles (open circles and dash lines (Qi *et al.*, 2006)) and ceramics (solid lines (Spinger-Varlag, 1981)) of $\text{Ba}(\text{Zr}_x\text{Ti}_{1-x})\text{O}_3$ system.

2.4 Various techniques for fabricating the powder, ceramic and thin film of perovskite materials

Sol-gel methods can be used for several purposes including the formation of fine powders homogeneous thin and thick films, fibers, homogeneous bulk material, porous solid, and powder as shown in figure 2.12 (Brinker and Scherer, 1990).

For powder synthesis, the process is normally achieved via ceramic processing routes such as solid-state reaction or mixed-oxide method. The process generally starts with the mixing and milling of the precursors, then the mixed powder is calcined. During the calcinations the crystallization is formed. This method is often

used because it is easy and has a low cost. In contrast, a high calcination temperature is required and impurities in powder can easily occur.

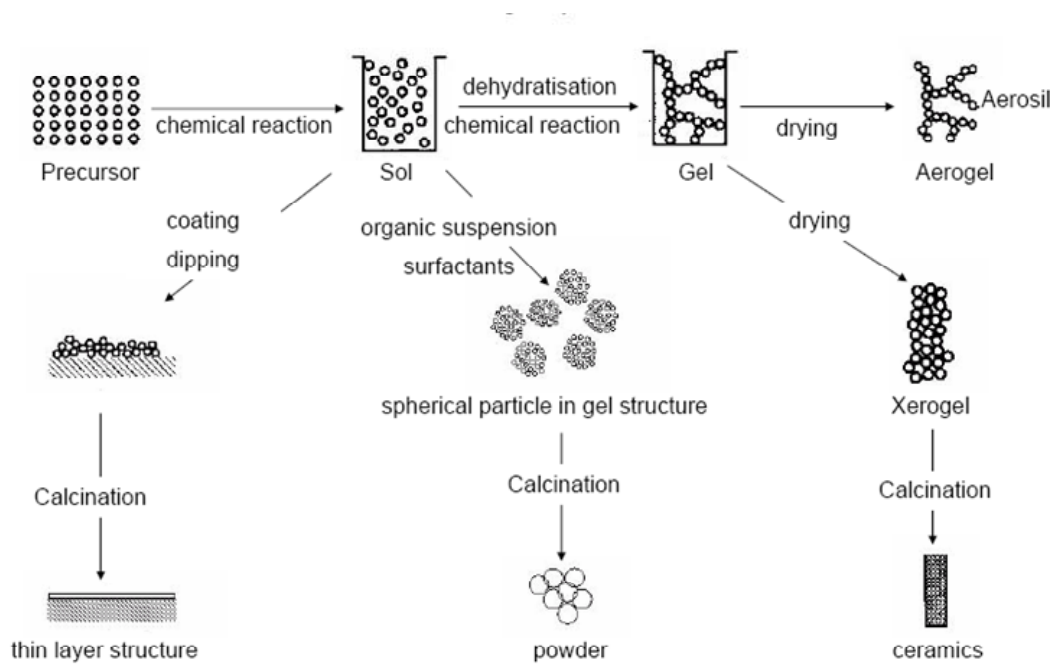


Figure 2.12 Overview of various sample geometries prepared by sol-gel method (Brinker and Scherer, 1990).

There are several methods employed to prepare powders such as precipitation, hydrothermal and sol-gel processes. Precipitation methods are mainly used for nano size powders which consist of only a few elements. If more elements are required in the powder, it is difficult to obtain the desired stoichiometry due to the differences in solubility of the various metal ions. Precipitation method commonly leads to the formation of small particles in the solution (Bernardi *et al.*, 2007). However, these small particles might form hard aggregates either during the precipitation process or during further processing steps, like filtration, washing, drying and calcinations.

Hydrothermal is a method involving the reaction that occurs at elevated temperature and pressure condition ($T > 100\text{ }^{\circ}\text{C}$, $p > 100\text{ kPa}$) in aqueous solution with in close system. There are various benefits obtained by this method, such as, cost effective precursor, low temperature process and high purity.

The sol-gel process normally starts with the product of sol, which is converted by a gelatin process into a gel. A polycrystalline can be further obtained from calcinations process. The powder obtained via sol-gel process is very interesting due to its superior mechanical stability and a high chemical purity for the production of high technology ceramics. Advantages of this method are fine grain size, easier composition control, and short process cycle. Sol-gel method is probably disadvantageous for the production powder due to only relatively small quantities of powders are obtainable from large quantities of the solution. If the liquid in a wet gel is removed under specific conditions, an aerogel which is a highly porous and extremely low density material will be obtained as shown in figure 2.12.

Generally, polycrystalline materials are prepared by solid-state or mixed-oxide method and started with powders of compound. Ceramics prepared from a homogeneous mixture of the powders result uses high temperature profile in order to obtain dense polycrystalline ceramics. For this reason the ceramics obtained from sol-gel process can reduce the expense of the overall process.

For fabricating thin films, table 2.2 summaries various techniques in the literature.

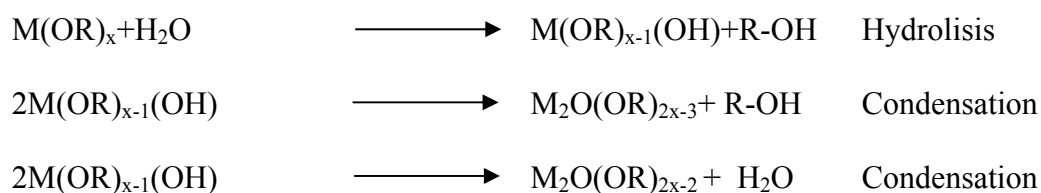
Table 2.2 Advantages and disadvantages of various techniques for processing of ferroelectric films (Jayadevan and Tseng, 2002).

Process	Advantage	Disadvantage
Sputtering	Possibility of a wide variety of materials at affordable cost, using multi-target assembly	Different sputtering yield variations in compositions
Pulse-laser-deposition (PLD)	Efficient and quick	Volatility of some species leads to non-uniform flux distribution and unsuitable for depositing large surface area
Molecular beam epitaxial (MBE)	Highly efficient for fabrication of superlattices	Sophisticated, highly expensive apparatus
Metal-organic chemical Vapor deposition (MOCVD)	Dense films deposited at low temperature on selected area	Complex reaction kinetics in the chamber affecting the film quality
Atomic layer MOCVD (ALM MOCVD)	Layer by layer depositions	Sophisticated apparatus, decomposition of individual source materials affects deposition process
Metal-organic Molecular beam epitaxy (MOMBE)	Suitable for fabrication of superlattices	Sophisticated, highly expensive apparatus, complex reaction kinetics in the chamber

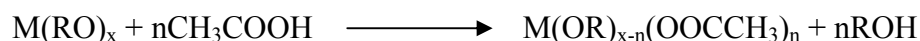
Table 2.2 Advantages and disadvantages of various techniques for processing of ferroelectric films (Jayadevan and Tseng, 2002) Cont.

Process	Advantage	Disadvantage
Sol-gel method	Economically affordable, low process temperature, good control over compositions, deposition on large area substrate	Difficult to active good conformal coverage on selective deposition, contamination due to decomposed groups in a gel

Among the techniques, sol-gel processing is an effective chemical method for preparing thin films. The common method for sol-gel synthesis involves hydrolysis and condensation alkoxides, starting from drying and densification of resulting gels in order to produce a ceramic material.



The starting reagents are typically metal alkoxide compounds, M(OR)_x , where M is a metal and R is an alkyl group, metal carboxylates, M(OOCR)_x , and metal β -diketonates, $\text{MO}_x(\text{CH}_3\text{-COCHCOCH}_3)_x$. The thin films have been prepared by sol-gel methods using a variety of metal organic precursors and solvent systems. Several methods are in current use for preparing sol gel, each of which has its merits and disadvantages. For example, 2-methoxyethanol route, this method was first reported by Budd, Dey and Panye (1986). The benefits of this method are controllable and reproducible chemistry and minimal aging effects. High cost of precursors, methoxyethanol is volatile and hazardous and a lot of chemistry for non-chemists is the disadvantages of this method. The other method is acetic acid route by using alkoxide compounds but modified by chelating reaction



The advantages of this method are simple solution preparation and non-hazardous. The selection of the starting reagents is dictated by solubility and reactivity considerations and the type of solution precursor species desired. Sol-gel method is normally followed by the deposition or coating technique such as spinning spray, dipping. Here we used the spin coater with high spinning speed. At each stage, temperature and time in a suitable range is necessary in order to obtain the crystalline film with good texture (Schwartz, Schneller and Waser, 2004).

Other thin film growth techniques from liquid and solution phase are spin casting, spraying, or dip coating. In this work the spin coater with high spinning speeds is used. At each stage, temperature and time in a suitable range is necessary to control in order to obtain the crystalline film with good texture.

2.5 Thick film technology

2.5.1 Screen-printing process

Thin films technology normally requires extreme deposited time, and are limited in the various thicknesses range. This is because the increase of internal stress during deposition possibly leads to the cracking of the thin films. Thick film technology such as tape casting, ink-jet and screen printing thus play an important role in a wide range of industrial applications. Among these techniques the screen printing offers several benefits such as simple, flexible and cost effective. When thick films are deposited by the screen printing process, it is possible to batch print diverse pattern on a variety of substrate materials. The thickness can be obtained from 1 to 100 μm . This process, for example, is as shown in figure 2.13. Using this method, the deposition on insulated substrate of layer having different electric and functional properties can be obtained. Subsequently, the wet film is dried and fired at a high temperature.

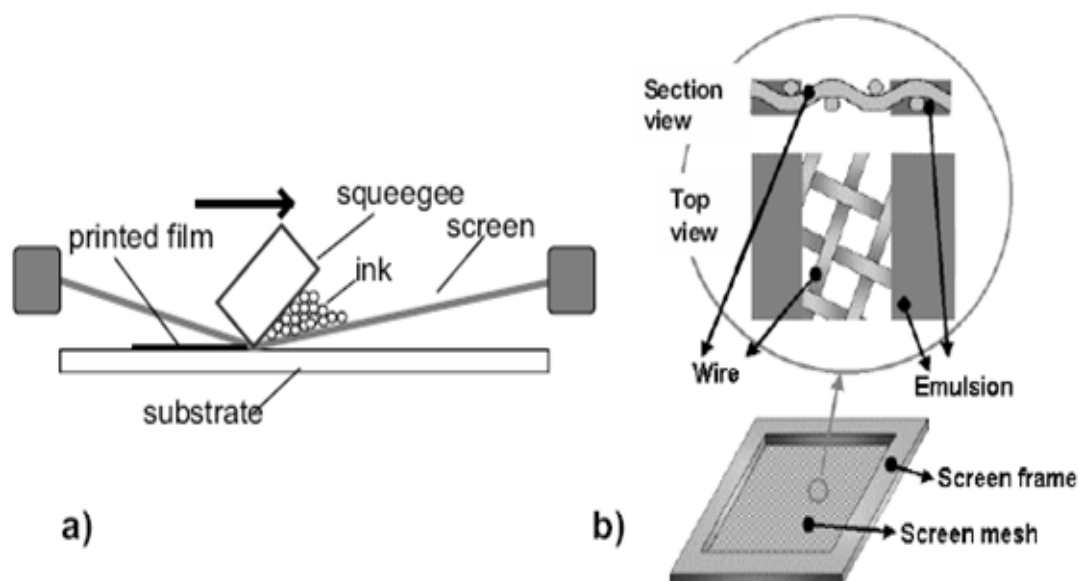


Figure 2.13 Screen-printing process (a) and screen mesh (b) (Ferrari, 2005).

Many factors relating to the preparation should be taken into consideration, such as the properties of the paste, the type of screen mesh and the substrate materials.

2.5.2 Paste materials

The paste is consisted of active material for application in electronic device, glass frits or oxide for densification and organic vehicles for deposition. The percentages of solid and liquid depends on the application and specific process. Screen printing techniques begin with making the paste or ink. The main property of the paste is enabled to pass through the screen easily and continuously, retaining the printed geometry with low temperature curing (Torah *et al.*, 2007).

The conductive inks normally use are gold, platinum-gold, gold-palladium, silver-palladium and silver. They meet the requirements which are solder ability, good adhesion, and high electrical conductivity, well-known physical and chemical stability with a relatively low cost.

A sintering additive is sometimes added into the ink in order to reduce sintering temperature. The process of distribution of active material and sintering aid form a liquid at temperatures in the region of 700-900 °C, which are introduced

through the liquid phase during the sintering process in order to enhance the packing of ceramic particles, also to activate diffusion paths for atomic species, and to increase the densification process of the thick film.

2.5.3 Screen meshes

Screen-printing most commonly used in MEMS technology is made of a woven stainless steel or nylon mounted on a steel frame. There are varieties of screen mesh, the characteristics of these materials are listed in table 2.3 .It can be seen that screen type 325 and 400 screen mesh is normally used in electrode screen printed layer due to its thin layer, For screen printing piezoelectric layer when thickness 50-70 μm will be obtained, the screen type 70 is used.

Table 2.3 Characteristics of conventional screen meshes (Castille, 2010).

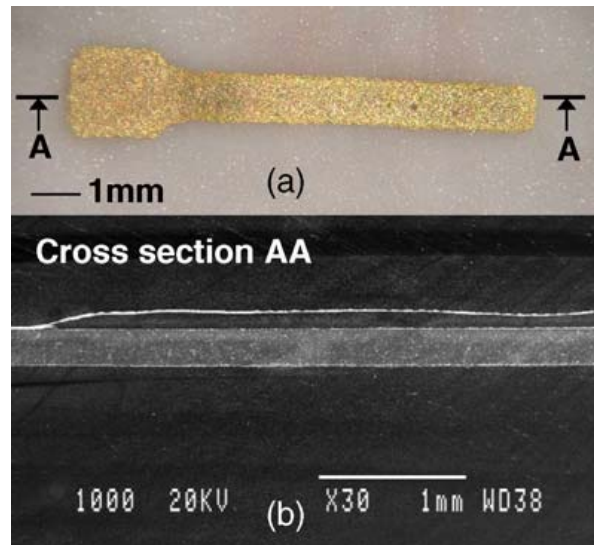
Screen type (mesh)	Wire diameter (μm)	Empty mesh (μm)	Thickness of screen (μm)	Thickness of wet film (μm)
70	51	266	211	185-230
105	75	160	162	144-178
200	41	86	94	81-97
325	30	51	66	58-71
400	25	38	56	50-61

2.5.4 Substrates

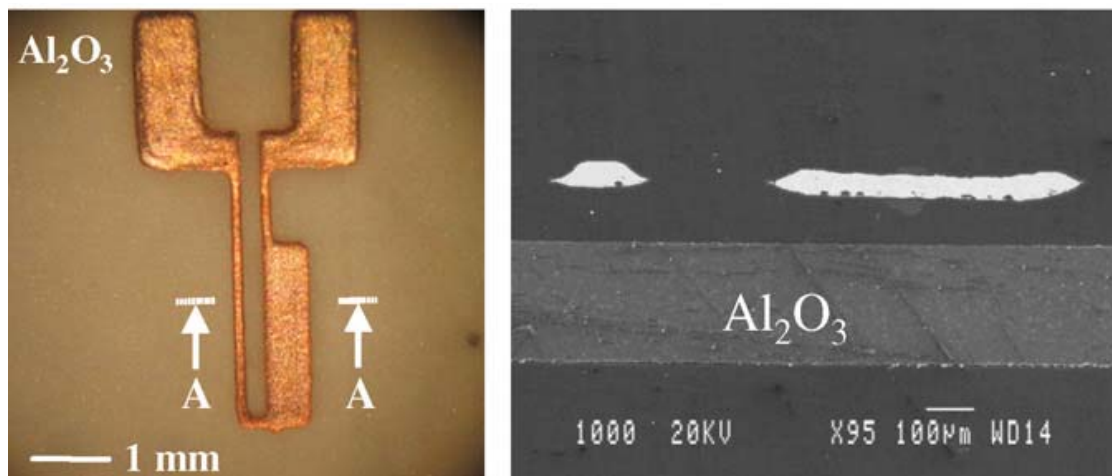
The screen-thick film can be printed on different types of substrate, such as alumina silicon, glass and stainless steel. A 96 % Alumina substrate is widely used for thick films can be printed hybrid circuit, because of their excellent mechanical strength, good thermal stability and dimension stability during the heat treatments (Torah *et al.*, 2007).

2.5.5 Screen-printed elements of various designs

Recently, the free-standing piezoelectric thick-films made with a sacrificial layer process for MEMS applications have been reported. They are very attractive due to move freely. The process of sacrificial layer involves three steps, firstly, deposition and consolidation of the sacrificial layer. The deposition of temporary structural layers with called sacrificial layer, then sintering. Finally, the sacrificial layer is eliminated by dissolving it in a solution. The basic requirements of the sacrificial layer in thick films technology are to provide mechanical support for depositing other layers, withstanding thermal especially, during sintering process and easy to remove in weak acetic acid (Lucat *et al.*, 2007; Ginet, 2007; Lucat *et al.*, 2008; Castille *et al.*, 2009; Castille., 2010). There applications are such as electrothermal, microactuators, microresistors, strain gauges, microchannels etc. as illustrated in figure 2.14.

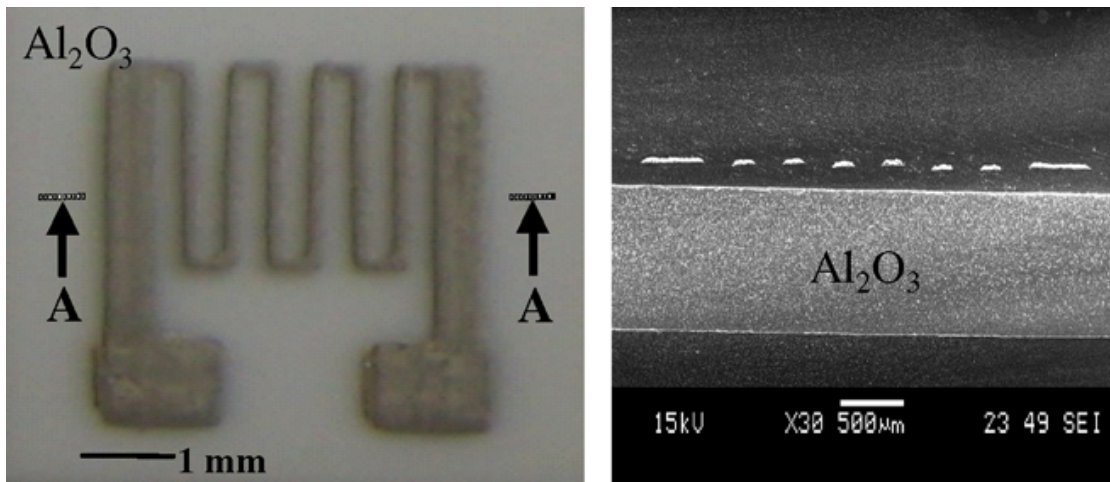


(a)

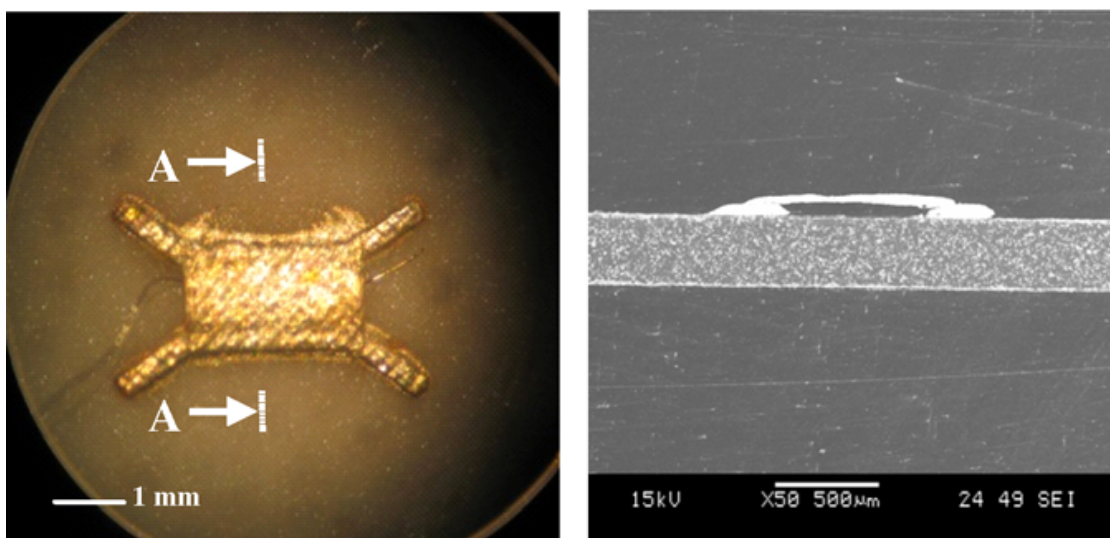


(b)

Figure 2.14 Examples of MEMS made by screen printing techniques with sacrificial layer (a) Gold cantilever beam (top) photograph and (bottom) SEM micrograph of AA cross section, (b) Screen-printed copper actuator (left) top view photograph and (right) SEM micrograph of AA cross-section, (c) Free-standing AgPt resistor of cantilever type (left) top view and (right) SEM, (d) Photograph of a silver microchannel (left) and SEM micrograph of AA cross-section (right) (Lucat *et al.*, 2008) and (e) Multi-stage screen-printing Au/PZT/Au (Castille *et al.*, 2009).

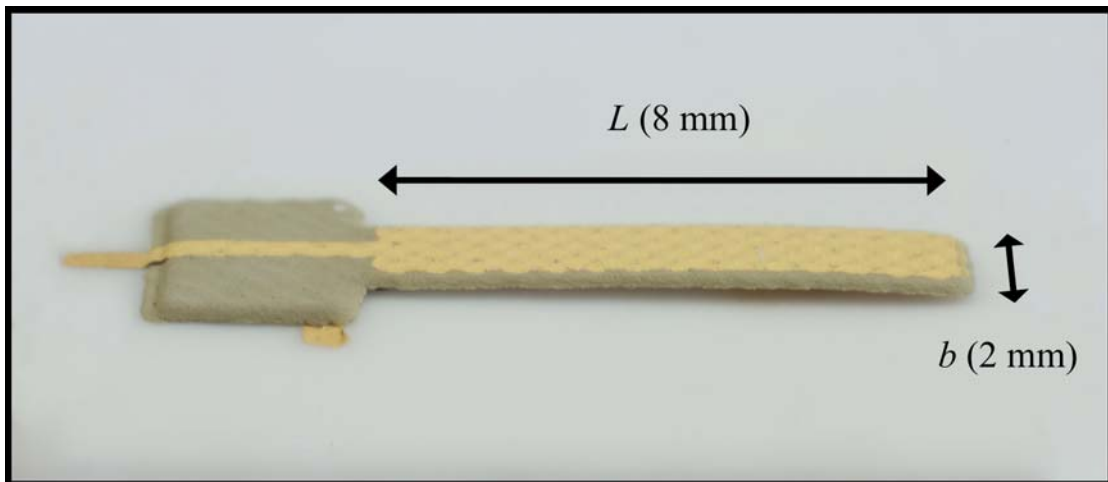


(c)



(d)

Figure 2.14 (Cont.) Examples of MEMS made by screen printing techniques with sacrificial layer (a) Gold cantilever beam (top) photograph and (bottom) SEM micrograph of AA cross section, (b) Screen-printed copper actuator (left) top view photograph and (right) SEM micrograph of AA cross-section, (c) Free-standing AgPt resistor of cantilever type (left) top view and (right) SEM, (d) Photograph of a silver microchannel (left) and SEM micrograph of AA cross-section (right) (Lucat, *et al.*, 2008) and (e) Multi-stage screen-printing Au/PZT/Au (Castille, *et al.*, 2009).



(e)

Figure 2.14 (Cont.) Examples of MEMS made by screen printing techniques with sacrificial layer (a) Gold cantilever beam (top) photograph and (bottom) SEM micrograph of AA cross section, (b) Screen-printed copper actuator (left) top view photograph and (right) SEM micrograph of AA cross-section, (c) Free-standing AgPt resistor of cantilever type (left) top view and (right) SEM, (d) Photograph of a silver microchannel (left) and SEM micrograph of AA cross-section (right) (Lucat, *et al.*, 2008) and (e) Multi-stage screen-printing Au/PZT/Au (Castille, *et al.*, 2009).

CHAPTER 3

SOL-GEL BARIUM ZIRCONATE TITANATE THIN FILMS

Piezoelectric elements of different compositions and dimensions are widely applied in a number of commercial products such as actuation and sensor. The integration of the piezoelectric bulk into the MEMS-based products is, however, often expensive or cannot achieve the functional requirements. The present work thus aims to describe the reliable synthetic route, acetic sol-gel, for production of BZT thin films. The thin films were deposited on the substrates using the spinning method and systematically characterized and discussed in this chapter. This is to increase the competitiveness of these films with lead-based piezoelectric elements available to date.

3.1 Introduction

Lead-free piezoelectrics whose properties are comparable to those of lead-based compositions have long been desired and extensively investigated. This includes remarkable barium titanate (BaTiO_3) and lithium titanate (LiTiO_3) (Shrout and Zhang, 2007). Particularly, barium titanate system such as perovskite $\text{Ba}(\text{Zr}_x\text{Ti}_{1-x})\text{O}_3$ or BZT have re-gained great attention because they are friendly to the environment and public welfare. Furthermore, in chemistry and material science basics the Zr^{4+} ion is more chemically stable than the Ti^{4+} ion. Larger ionic radius of the Zr^{4+} ion (86 pm) when compared to that of the Ti^{4+} ion (74.5 pm) leads to a bigger distortion of the perovskite lattice, resulting in high strain levels and high piezoelectric strain coefficient. There have been, nevertheless, only a few reports (Choi *et al.*, 2002; Dixit *et al.*, 2003; Zhai *et al.*, 2004; Cheng *et al.*, 2006) regarding the crystallographic data and material properties of the BZT thin films. The present work thus aims to fabricate the BZT thin films with different Zr/Ti ratios and identifies their crystallographic phases. Their composition-dependent properties including the piezoelectric coefficient are determined. Possible applications of these films have been also pointed out.

3.2 Review of previous work

In elaborating the thin films the chemical solution deposition (CSD) techniques are the most attractive due to several advantages achieved such as mild processing conditions with low cost, high homogeneity of the products and controllable stoichiometry. An important benefit of using this process is that an elaborated film is generally fired to complete its crystallization at a temperature lower than that in the solid-state reaction normally used for ceramic fabrication (Schwartz, , Schneller and Waser, 2004; Schwarzhkopf and Fornari, 2006).

There are four basic steps normally used in the CSD processes:

- (i) Synthesis of the precursor solution,
- (ii) Deposition by spin-casting or dip-coating,
- (iii) Low-temperature heat treatment (300-400 °C) in air or oxygen for drying, pyrolysis of organic species and formation of an amorphous film, and
- (iv) High-temperature heat treatment (typically 500-1100 °C) in air or oxygen atmosphere for densification and crystallization of the coated film.

The CSD methods can be divided into following three main routes:

- (a) Sol gel processes using 2-methoxyethanol solvent.
- (b) Chelate or hybrid processes using the modifying ligands such as acetic acid.
- (c) Metal-organic decomposition (MOD) route using water-sensitive metal carboxylate compounds.

Among these methods, the sol-gel process is the most widely used for thin films fabrication. This is because it enables the realization of highly homogeneous films into relatively large surface area with relative ease, however, time consuming. There are two main mechanisms involved with relative the sol-gel process (Schwarzhkopf and Fornari, 2006):

- (1) Hydrolysis reaction, consisting of a nucleophilic attack of water on the metalorganic or metal-salt molecules presented in the solution, this results in the formation of a so-called “sol”.
- (2) Condensation, where the 2- or 3-dimensional networks of an amorphous phase are firstly formed.

Several efforts have been used to improve the film qualities which are strongly depended upon the deposition conditions; non-stoichiometry occurred during the process, electrode materials, dopants, ceramic film-metal substrate interface, and microstructure, thickness and homogeneity of the films etc. The previously work by Khaenamkaew *et al.*, (2007) reported on the lead zirconate titanate or PZT thin films with various Zr/Ti ratios. They fabricated the PZT thin films on Pt/Ti/SiO₂/Si substrates by using the sol-gel 2-methoxyethanol route. All the PZT thin films crystallized into a single perovskite phase and had a dense texture without cracks. The PZT thin films with compositions located in the morphotropic phase boundary (MPB) shown the most attractive ferroelectric properties. They also fabricated the PZT films on Pt/Ti/SiO₂/Si with gradual change in Zr content across the thickness direction to obtain either up-graded or down-graded PZT thin films (Khaenamkaew *et al.*, 2008). These films contained successive layers of various compositions with a slight difference in order to facilitate the non-uniform distribution of stresses in the metal-ceramic interfaces, leading to the reliability and lifetime extension of the ferroelectric structure. However, the PZT graded thin film exhibited lower piezoelectric response than the PZT thin film of MPB composition (Muensit *et al.*, 2008). Thin films with single-composition deposition are therefore the main interesting structure adapted to the fabrication of the BZT thin films in the present chapter.

Dixit *et al.*, (2002) synthesized the sol-gel Ba(Zr_xTi_{1-x}O₃), (x = 0.0-1.0) thin films deposited on (100) oriented lanthanum aluminate substrate. Barium acetate or Ba(CH₃COO)₂, zirconium n-propoxide or Zr(OC₃H₇)₄ and titanium isopropoxide or Ti(OC₃H₇)₄ were used as starting materials, and the solvent was acetic, In order for the complete dissolution of barium acetate in acetic, ethylene glycol was added. Their BZT thin films of an average thickness of 400 nm were pyrolysed at 600 °C for 5 min. The thin films were annealed at 1,100 °C for 2 h. From their investigation obtained

from an atomic force microscopic data it was indicated that the Zr content significantly influenced the evolution of the microstructures and average grain size of the films. The observation from Raman spectra of the film has shown a cubic crystal structure in the film with $x > 0.20$.

Dixit *et al.*, (2005) characterized the dielectric property for sol-gel BZT thin films with various Zr contents and thicknesses of 0.55-0.59 μm . They reported the dielectric constant and dielectric loss measured at 100 kHz for the films of $\text{Ba}(\text{Zr}_{0.015}\text{Ti}_{0.095})\text{O}_3$, $\text{Ba}(\text{Zr}_{0.015}\text{Ti}_{0.095})\text{O}_3$, and $\text{Ba}(\text{Zr}_{0.015}\text{Ti}_{0.095})\text{O}_3$ were 516 and 0.05, 606 and 0.05, 335 and 0.03, respectively.

Jiwei *et al.*, (2004) prepared the $\text{Ba}(\text{Zr}_{0.35}\text{Ti}_{0.65})\text{O}_3$ thin films of highly (100) preferred orientation by introducing a buffer layer of LaNiO_3 onto Pt/Ti/SiO₂/Si substrates. The BZT precursors of different molars of 0.3, 0.1 and 0.05 M yielded the films with thicknesses of 330, 310 and 420 nm, respectively. It was found that the films were annealed at a temperature lower than 1,100 °C, i.e., 700 °C. It suggested that the concentration of the precursor directly related to the crystallization behavior and the microstructure of the thin films. The precursor with small concentration (0.3 M) produced the film with large average grain size and thus large P-E loop. The film with the largest thickness (420 nm) obtained the maximum dielectric.

Zhai *et al.*, (2004) fabricated the sol-gel the thin films of $\text{Ba}(\text{Zr}_{0.35}\text{Ti}_{0.75})\text{O}_3$. Their starting materials were similar to those mentioned earlier. According to their preparation procedure, the viscosity of the precursor solution was controlled by adding the ethylene glycol ($\text{CH}_2\text{OHCH}_2\text{OH}$). Good control in viscosity of the solution led to the resultant film without cracks and voids. It was important to reflux the solution until the concentration of the solution was 0.1 M. After 24 h-aging, the deposition of the film on Pt/Ti/SiO₂/Si(100) was done by spin coating. All the wet films were dried and annealed at 500 °C. The amorphous films were then fired at 700 °C for 30 min in order to allow the crystallization to take place. By repeating the spin-coating–drying–annealing process, the final thickness obtained for the BZT film was 320 nm, which was relatively small. (This was considered in the present work to be a major disadvantage in using thin films in microelectronic applications).

Halder *et al.*, (2005) reported the electromechanical property of sol-gel Ba(Zr_xTi_{1-x})O₃ thin films on Pt/TiO₂/SiO₂/Si substrates of various compositions ($x = 0, 0.03, 0.05, 0.07, 0.1, 0.2, 0.3$ and 0.4). A double-beam interferometric technique for the measurements was performed. The films were annealed at 750 °C for 30 min and sputtered a gold metal onto the surface of the film to use as electrodes. With increasing Zr content up to 0.07 and above, the electromechanical response in the films were found to decrease. The best value of the piezoelectric coefficient d_{33} about 30 pm/V was obtained from the Ba(Zr_{0.05}Ti_{0.95})O₃ thin film. The present work has also employed the interferometric technique which is a single-beam approach available in the Material Physics Laboratory, Prince of Songkla University to observe the piezoelectric response in all samples of the BZT system.

Recently, Cheng *et al.*, (2006) also prepared the Ba(Zr_{0.05}Zr_{0.95})O₃ thin film using sol-gel process. The first two starting materials were also barium acetate and zirconium-n-propoxide. The third one was tetrabutyl titanate or Ti(OC₄H₉)₄ and acetylacetone or C₅H₈O₂ was a reagent to stabilize the tetrabutyl titanate in 2-methoxyethanol or C₃H₈O₂ solvent. The prepared BTZ film was fired at a relatively low temperature of 650 °C for a short time of 10 min in an oxygen atmosphere. The 330 nm thickness BZT films had good ferroelectric properties showing the remanent polarization and coercive electric field of 3.54 μC/cm² and 95.5 kV/cm, respectively. At 10 kHz, the dielectric constant and dielectric loss of the film were 201 and 0.029, respectively.

3.3 Materials and methods

3.3.1 Preparation of the Ba(Zr_xTi_{1-x})O₃ precursors

In this work the precursor solution of Ba(Zr_xTi_{1-x})O₃ was prepared based on the acetic route reported by Zhai *et al.*, (2004) and Jiwei *et al.*, (2004) without depositing buffer layer. Chemical substances and the manufacturers used were barium acetate (Ba(CH₃COO)₂, Ajex Finechem), zirconium (IV) isopropoxide (C₁₂H₂₈O₄Zr, Aldrich, 70 wt% solution in 1-propanol), and titanium (IV) isopropoxide (C₁₂H₂₈O₄Ti, Aldrich, 97% purity), acetic acid (Merch, 100% purity) and 2-methoxyethanol (CH₃OCH₂CH₂OH, Ajex Finechem). In the preparation

procedure, barium acetate was initially heated and dissolved in acetic acid. After cooling to room temperature, zirconium (IV) isopropoxide ($C_{12}H_{28}O_4Zr$) was mixed with in the 2-methoxyethanol and followed by adding titanium (IV) isopropoxide ($C_{12}H_{28}O_4Ti$). The mol ratios of Zr:Ti were varied as 0.00:1.00, 0.05:0.95, 0.10:0.90, 0.15:0.85 and 0.20:0.80, respectively. The acetyl acetone (CH_2OHCH_2OH) was added into the mixture to control the viscosity and prevent cracking of the films. The solution was mixed and refluxed for 1 h. The concentration of the final solution was adjusted to be 0.1 M. The precursor was aging the hydrolyzed solution for 24 h. The preparation procedure for BZT solution was shown in figure 3.1. Subsequently, the BZT gel was analyzed the mass changed with temperature by using a Thermogravimetric Analyzer (TGA7; Perkin Elmer).

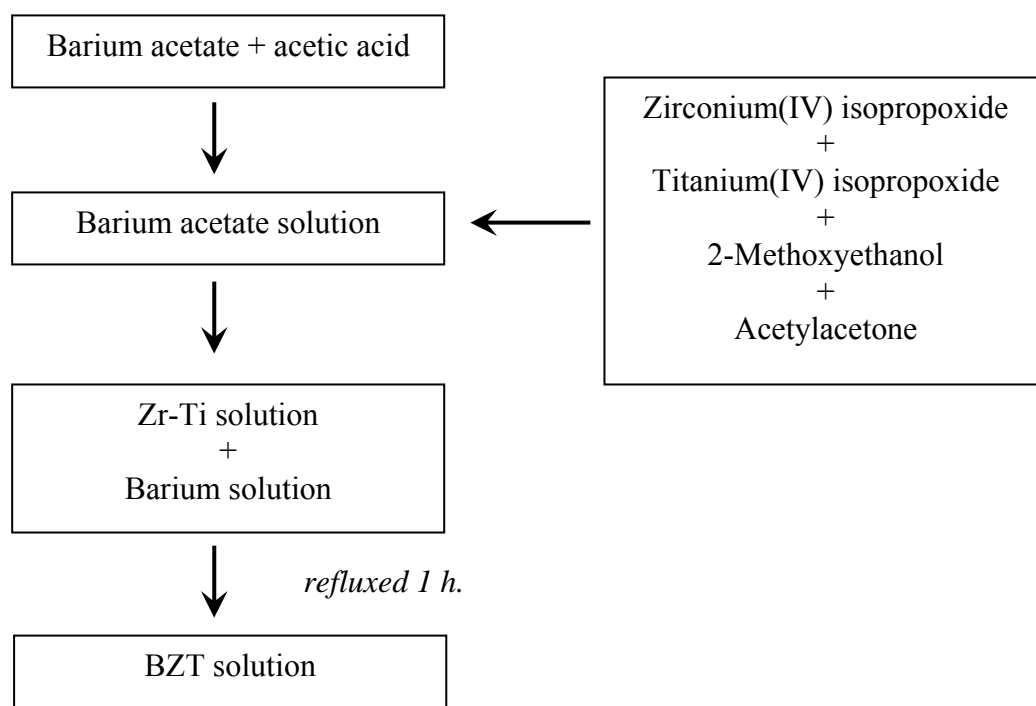


Figure 3.1 Preparation procedure used in the BZT sol-gel process.

3.3.2 Thin film fabrication

Commercial (111)Pt/TiO₂/SiO₂/Si substrates of an area of 0.8×0.8 cm² were used for depositing the BZT films. The deposition was repeated until the film had a thickness in a range of 200-400 nm. The wet films were dried at 150 °C and pyrolysed at 350 °C. These amorphous films were then annealed from 800-1,000 °C for 30 min. Figure 3.2 summaries the preparation procedure described in this section.

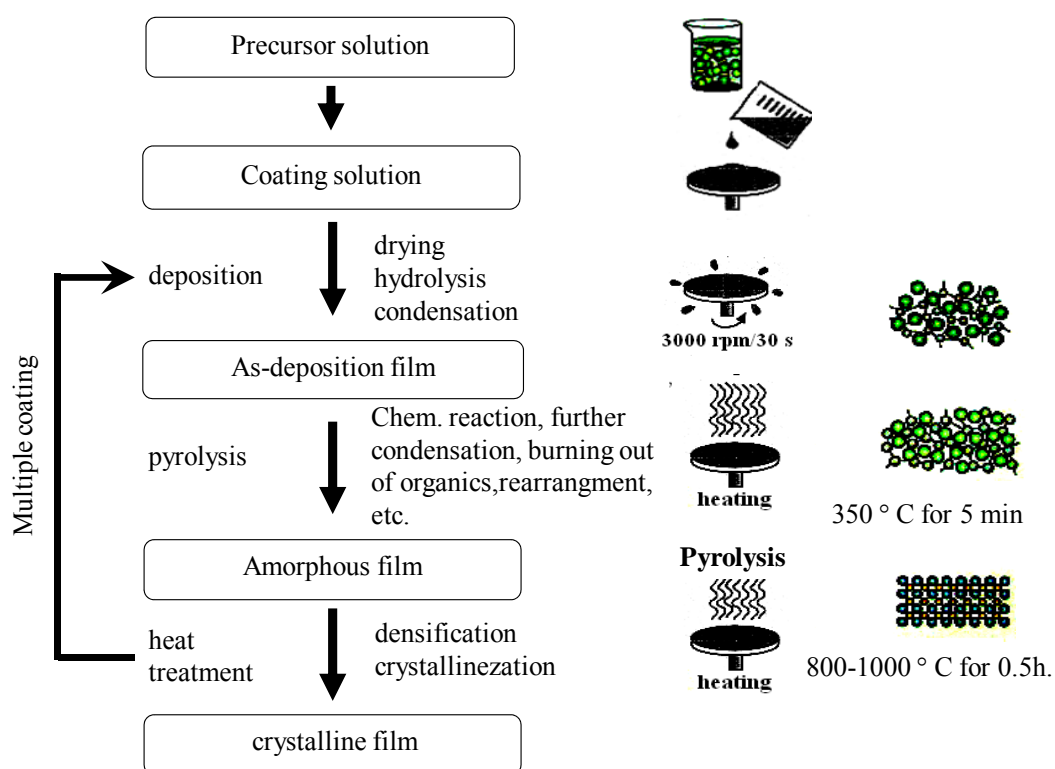


Figure 3.2 Flow chart of the BZT thin film and the preparation conditions mainly used in this work (Modified from Schwartz, Schneller and Waser, 2004).

3.3.3 Characterization of the thin films

3.3.3.1 Phase analysis of the thin films

The crystal structure for all the films was analyzed using Phillips PW 3710 Powder Diffractometer (PHILLIPS X'pert MPD) with Ni filtered $\text{CuK}\alpha$ radiation. The patterns were recorded in the 2θ range of $20\text{-}60^\circ$. The Raman spectroscope (NT_MDT; NTEGRA spectra) with an optical objective lens with 100X was used for focusing the 633 nm radiation from a Coherent He-Ne laser on each film.

3.3.3.2 Microstructure of the thin films

The SEM equipment was a JEOL JSM-5800 LV (SEM5800). The morphology of the films was observed in details by a Field Emission Scanning Electron Microscope (FE-SEM, HITACHI 4700) with magnifications ranging from 20X to 500,000X (0.2-0.3 eV). An Atomic force Microscope (AFM, SEIKO SPA 400) was used for investigating the topology of the thin films.

3.3.3.3 Dielectric properties and piezoelectric coefficient determination of the thin films

A layer of gold was sputtered through a rigid mask to form an electrode of an area of $\sim 0.3\text{ mm}^2$ on the surface of the film. At one corner of the specimen the film was etched away using a 40% hydrofluoric acid in order to use the bare metalized substrate as one of the electrodes (Khaenamkaew *et al.*, 2008). The dielectric constant (ϵ_r) and dielectric loss ($\tan \delta$) as a function of frequency measurements were measured at room temperature in a frequency range of 10^2 to 10^6 Hz using a LCR meter (Hewlett Packard 4263B and Aligent 4285A).

The piezoelectric response in the film was investigated by means of a single-beam Michelson interferometer with a spatial resolution of 10^{-13} m. Details of the experimental setup and principles of the techniques, have been reported elsewhere (Muensit and Guy, 1998; Muensit and Khaenamkae, 2002). In the arrangement (figure 3.3) a He-Ne polarized laser (1135p, Uniphase) was used as a light source. A beam splitter divided the incoming laser beam into two arms, reference and probing arms. The electrode surface of the film was used to reflect the laser beam in the probing arm back to the beam splitter while the other beam was reflected by the reference mirror.

Two reflected beams caused the interference fringes as well as a change in laser intensity caused by ambient vibration (<1 kHz). These displacement variations were stabilized electronically by a feedback amplifier. When an *ac* voltage was applied by a signal generator (DS 340, Stanford Research System) to the film, the film exhibited the inverse piezoelectric effect and caused a small change in the laser intensity which was detected by a *p-i-n* photodiode detector (BPX 65). The detector converted these optical changes into an electrical signal detected by a lock-in amplifier (SR5 10, Stanford Research System).

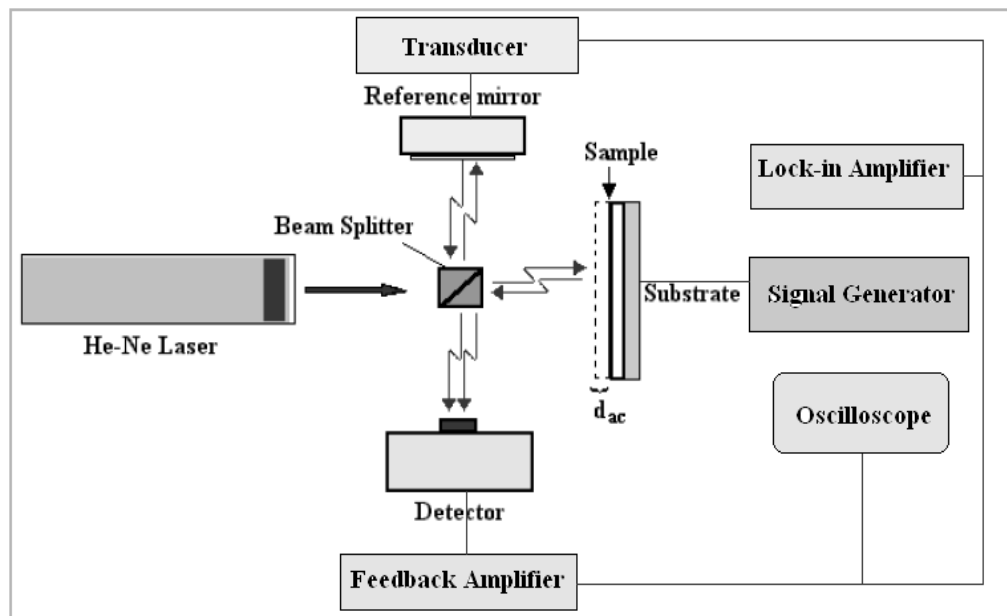


Figure 3.3 Schematic diagram of the modified Michelson interferometer used for the determination of the piezoelectric coefficient (Khaenamkaew, 2008).

In practice, the c -axis of the film is set to be perpendicular to the plane of the film. When the electric field applied parallel to the c -axis, the d_{33} value can be determined using the relationship given by (Zhang, Pan and Cross, 1988):

$$d_{33} = \frac{d_{ac}}{V} = \frac{\lambda V_{out}}{2\pi V_{pp} V} \quad (3.1)$$

where V is the *rms* voltage driving the film, V_{pp} is the peak-to-peak voltage corresponding to the change in interference light intensity, λ is the wavelength of the polarized He-Ne laser (632.8 nm, V_{out} is the output from the lock-in amplifier measured at the reference frequency from the function generator and d_{ac} is a small electric-field induced displacement related to the strain of the film. The obtained d values were the clamped one. In analyzing the true d values of the films (Muensit, *et al.*, 2008), the elastic compliances measured at a constant electric field are needed in the calculation, which was, however, not included in the present work.

3.4 Results and discussion

3.4.1 Thermogravimetric characterization

The thermogravimetric analyzer (TGA) curves were shown in figures 3.4. The mass loss during the heat treatment, three mechanisms were involved as follows: (i) dehydration of the gels in a 25-200 °C range, leading to the mass loss 5-10 %, (ii) pyrolysis in which all samples lost their weights for 40-50 % between 200-650 °C and (iii) decomposition of residual CO₂ and crystallization between 650-1,200 °C with the mass loss 10-15 %.

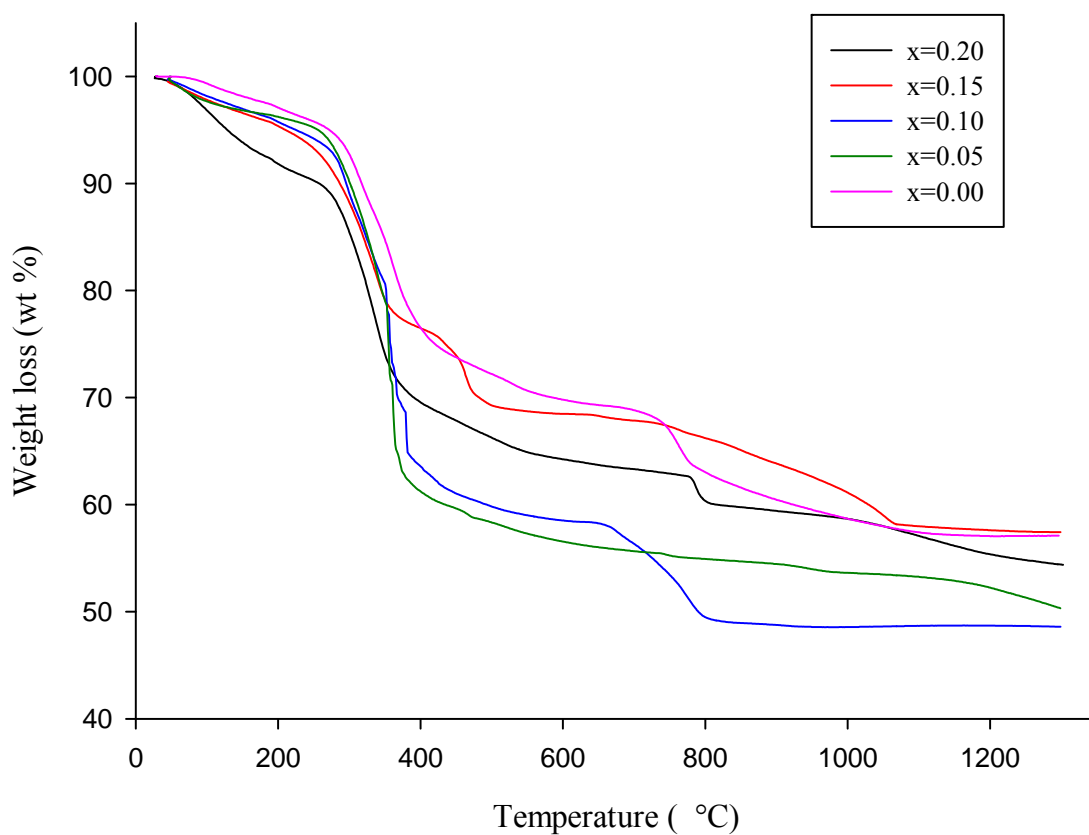


Figure 3.4 TGA curves of the Ba(Zr_xTi_{1-x})O₃ gels.

3.4.2 X-Ray diffraction data

The XRD patterns of Ba(Zr_{0.20}Ti_{0.80})O₃ thin films deposited on (111)Pt/Ti/SiO₂/Si substrates annealed at different temperatures were shown in figure 3.5.

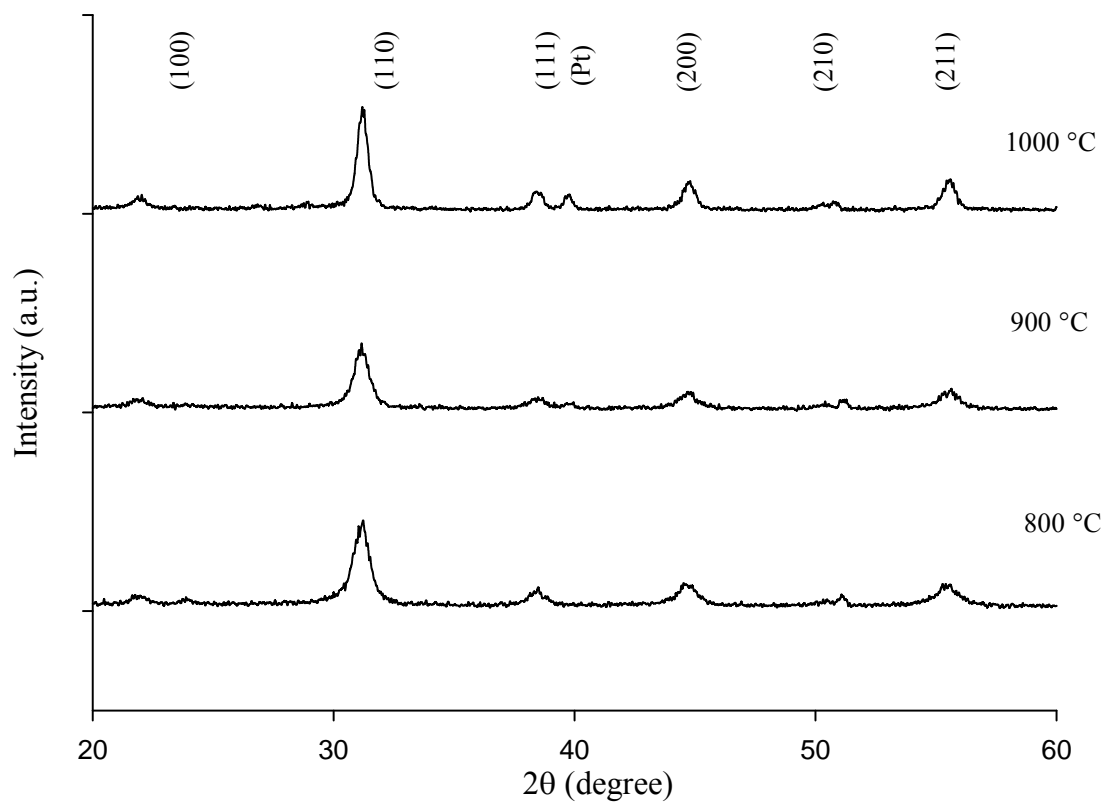


Figure 3.5 XRD results of the Ba(Zr_{0.20}Ti_{0.80})O₃/ (111)Pt/Ti/SiO₂/Si annealed at various temperatures.

By using the Bragg's Law, the lattice constants could be extracted from the XRD data (ICDD reference pattern: 00-036-0019) (figure 3.5) and summarized for all the films as shown in tables 3.1-3.3.

Table 3.1 Summary of the Bragg planes, 2θ , d_{hkl} , and lattice constants of the $\text{Ba}(\text{Zr}_{0.20}\text{Ti}_{0.80})\text{O}_3$ thin film annealed at 800 °C.

(hkl)	2θ	d_{hkl} (Å)	Lattice constants (a) (Å)
(001)	21.75	4.04	4.0497
(011)	31.23	2.85	4.0445
(002)	44.58	2.02	4.0586
(112)	55.27	1.65	4.0675

Table 3.2 Summary of the Bragg planes, d_{hkl} , 2θ , and lattice constants of the $\text{Ba}(\text{Zr}_{0.20}\text{Ti}_{0.80})\text{O}_3$ thin film annealed at 900 °C.

(hkl)	2θ	d_{hkl} (Å)	Lattice constants (a) (Å)
(001)	22.76	4.07	4.0786
(011)	31.12	2.87	4.0593
(002)	44.72	2.23	4.0479
(112)	55.56	1.65	4.0462

Table 3.3 Summary of the Bragg planes, d_{hkl} , 2θ , and lattice constants of the Ba(Zr_{0.20}Ti_{0.80})O₃ thin film annealed at 1,000 °C.

(hkl)	2θ	d_{hkl} (Å)	Lattice constants (a) (Å)
(001)	22.03	4.04	4.042
(011)	31.20	2.86	4.049
(002)	44.79	2.02	4.045
(112)	55.59	1.65	4.044

The average lattice constants of Ba(Zr_{0.20}Ti_{0.80})O₃ films were 4.055, 4.058 and 4.045 Å for the films annealed at 800, 900, and 1000 °C, respectively. From XRD patterns, It can concluded that a suitable annealing temperature for the film was then 800 °C because the annealed at 800 °C sample was polycrystalline perovskite without pyrochlore. Consequently, the XRD patterns of Ba(Zr_xTi_{1-x})O₃ thin films with various Zr/Ti ratios annealed at 800 °C were shown in figure 3.6. The (110) diffraction peak of BZT system shifted lower of diffraction angle as Zr increased

The lattice parameter of the thin films displayed in figure 3.7, for the film with $x = 0$ or BaTiO₃ thin film, the lattice parameters of $a = 3.965$ Å and $c = 4.017$ Å were evaluated from the XRD peaks at $2\theta = 32.33^\circ$ and 32.75 to revealed the tetragonal crystalline phase. When $x = 0.20$, the cubic phase was indicated due to the lattice constant of $a = 4.05$ Å (Wu, Wu and Chen, 1996; Pontes *et al.*, 2004; Qi *et al.*, 2006). For the Ba(Zr_{0.20}Ti_{0.80})O₃ thin film, the cubic phase was confirmed from the lattice constant, $a = 4.055$ Å evaluated from the XRD peak at 45° . An exact crystalline phase of films at other compositions, $0 < x < 0.2$, was not able to be identified due to the close proximity of diffraction angles of the phases (figure 3.6).

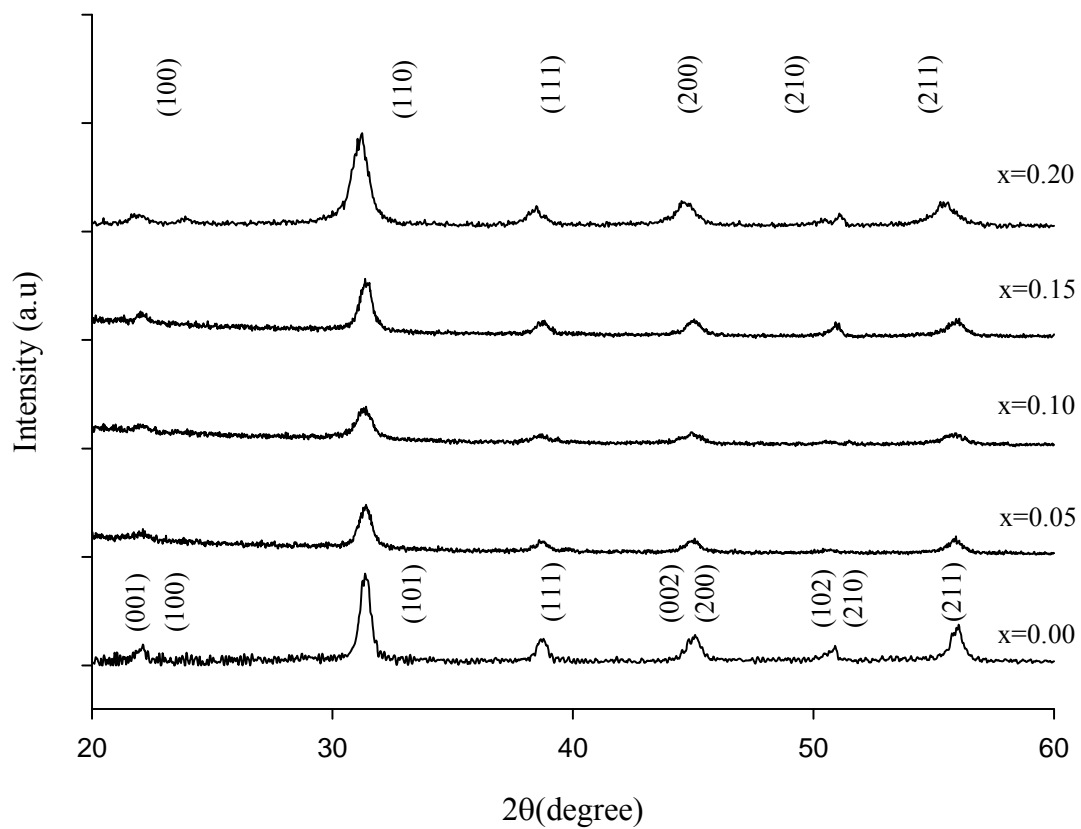


Figure 3.6 XRD pattern of the Ba(Zr_xTi_{1-x})O₃/ (111)Pt/Ti/SiO₂/Si annealed at 800 °C;
x = 0.00-0.20.

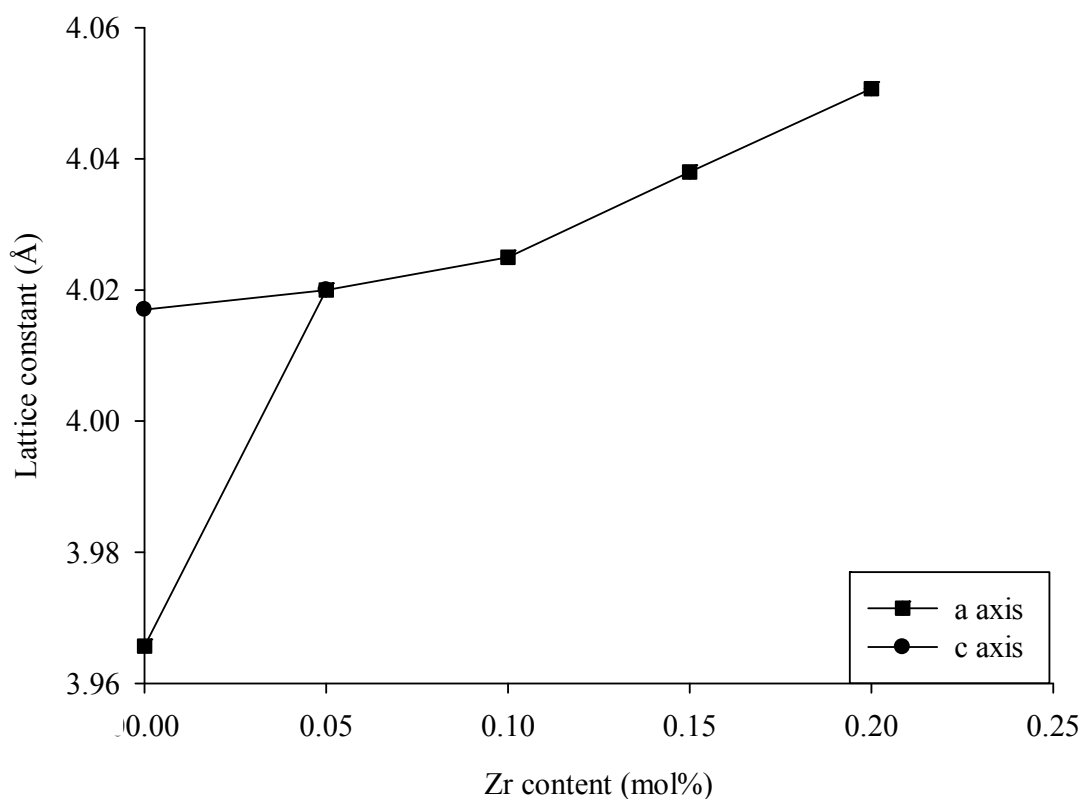


Figure 3.7 Lattice constant of the $\text{Ba}(\text{Zr}_x\text{Ti}_{1-x})\text{O}_3$ thin films.

3.4.3 Raman spectroscopy

The figures 3.8-3.10 represented the Raman spectrum of the $\text{Ba}(\text{Zr}_x\text{Ti}_{1-x})\text{O}_3$ thin films. The random grain orientation of the BZT films the directions of the phonon wave vectors are random from one grain to the others with respect to the crystallographic axes (Moura *et al.*, 2008; Dobal *et al.*, 2001). When the Zr content reached 10 mol%, the frequency mode was at about 129 cm^{-1} absent. This is because the ionic radius of the Zr^{4+} ions is larger than that of the Ti^{4+} ions. Moreover, it can be concluded that the phase transforms from orthorhombic to rhombohedral (Dobal *et al.*, 2001; Dixit *et al.*, 2002; Pontes *et al.*, 2004; Moura *et al.*, 2008).

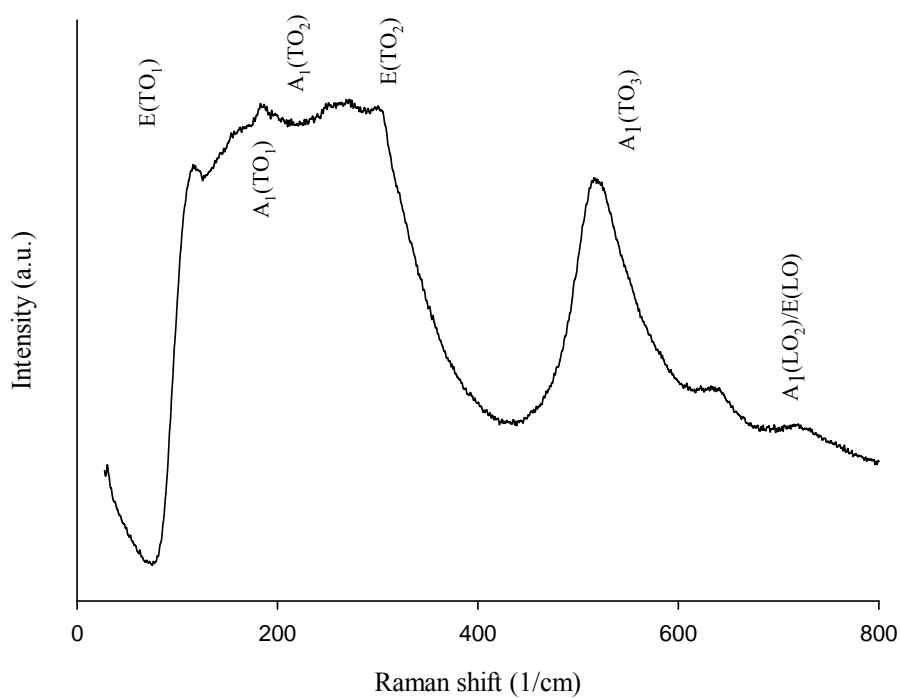


Figure 3.8 Raman spectra of the Ba(Zr_{0.05}Ti_{0.95})O₃ thin film.

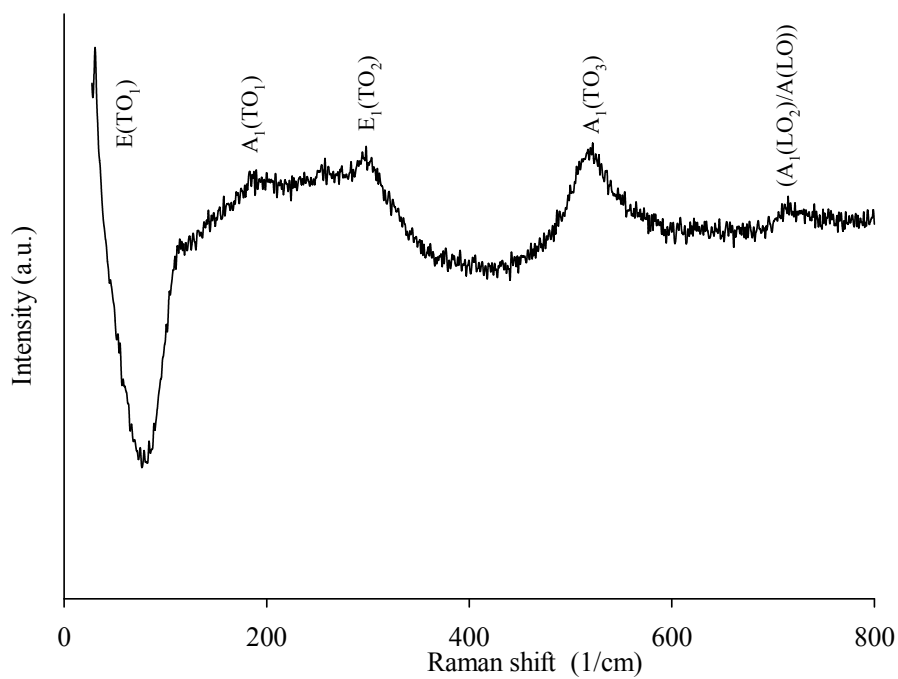


Figure 3.9 Raman spectra of the Ba(Zr_{0.10}Ti_{0.90})O₃ thin film.

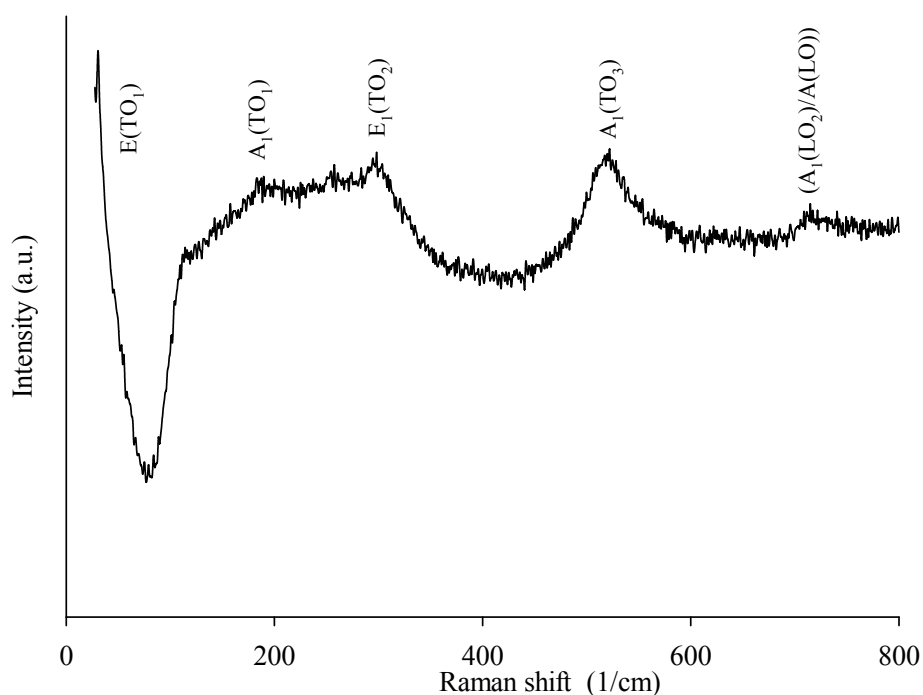


Figure 3.10 Raman spectra of the $\text{Ba}(\text{Zr}_{0.15}\text{Ti}_{0.85})\text{O}_3$ thin film.

3.4.4 Microstructure of $\text{Ba}(\text{Zr}_x\text{Ti}_{1-x})\text{O}_3$ thin films

From the SEM micrographs, the thicknesses of all films were approximately 300-400 nm and uniform in grain dimension. As seen in figures 3.11-3.15, these images could reveal the nucleation at the film-substrate interface and within the bulk of the film. This could be seen as a non-columnar microstructure (the columnar-type was normally found in the PZT thin films (Khaenamkaew *et al.*, 2007).

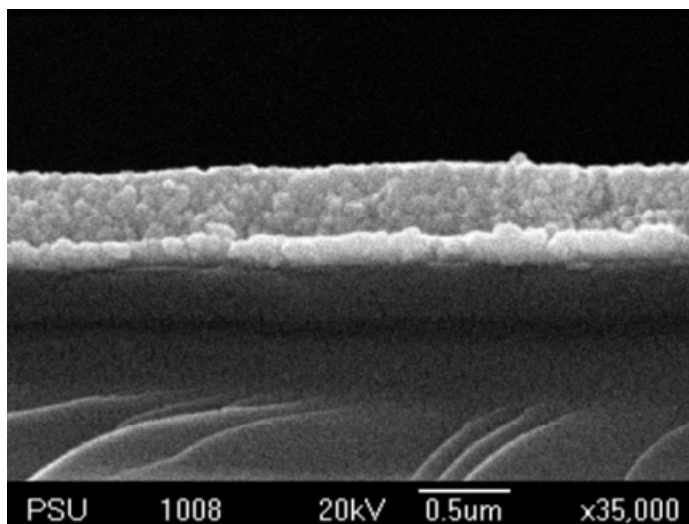


Figure 3.11 SEM cross-sectional image of the BaTiO₃ thin film.

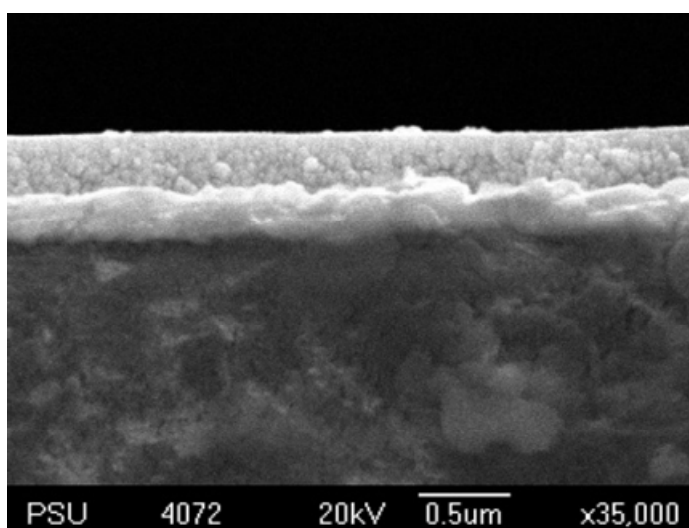


Figure 3.12 SEM cross-sectional image of the Ba(Zr_{0.05}Ti_{0.95})O₃ thin film.

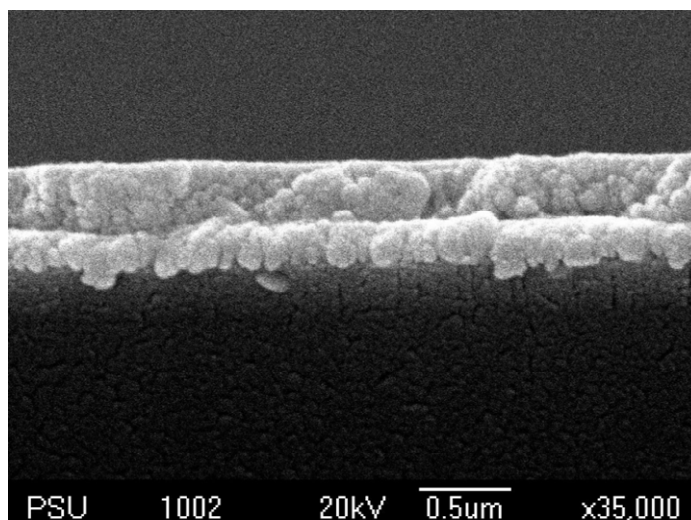


Figure 3.13 SEM cross-sectional image of the $\text{Ba}(\text{Zr}_{0.10}\text{Ti}_{0.90})\text{O}_3$ thin film.

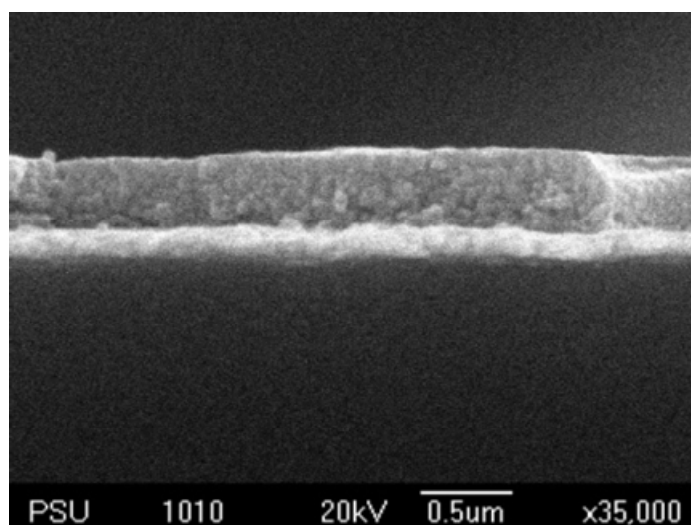


Figure 3.14 SEM cross-sectional image of the $\text{Ba}(\text{Zr}_{0.15}\text{Ti}_{0.85})\text{O}_3$ thin film.

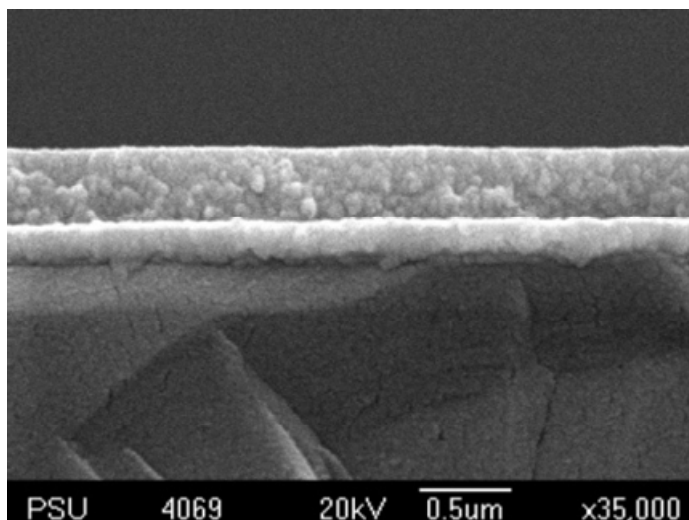


Figure 3.15 SEM cross-sectional image of the $\text{Ba}(\text{Zr}_{0.20}\text{Ti}_{0.80})\text{O}_3$ thin film.

Apart from the texture of the films observed from SEM images, the FE-SEM planar images were shown in figures 3.16-3.20. It could be seen that the increase of Zr content the morphology became dense, smoother and smaller grain size.

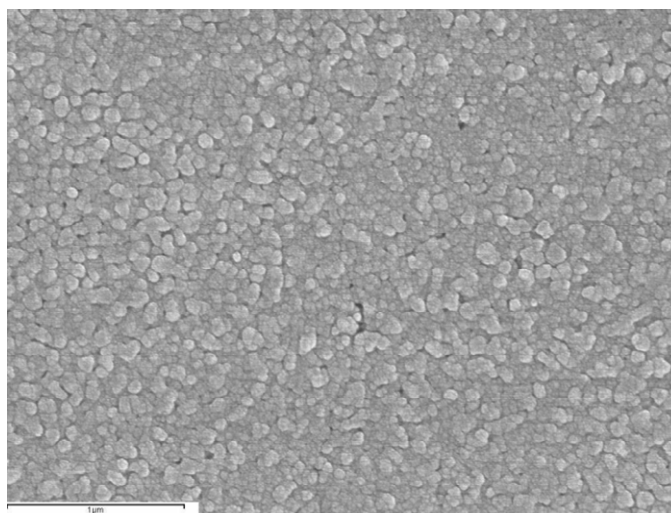


Figure 3.16 FE-SEM planar image of the BaTiO_3 thin film.

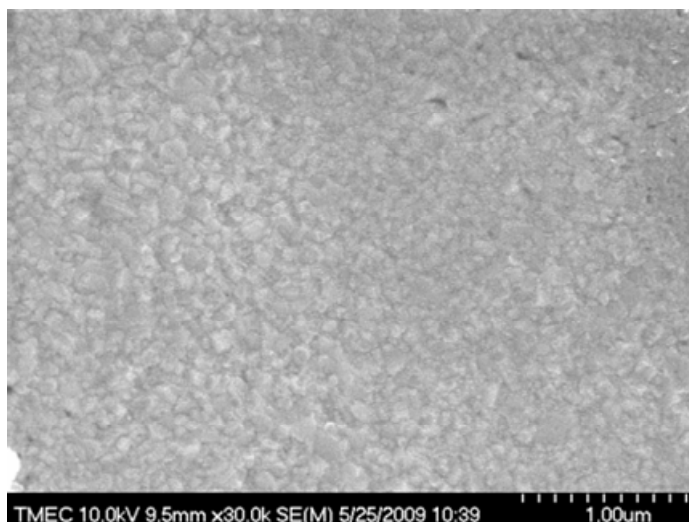


Figure 3.17 FE-SEM planar image of the Ba(Zr_{0.05}Ti_{0.95})O₃ thin film.

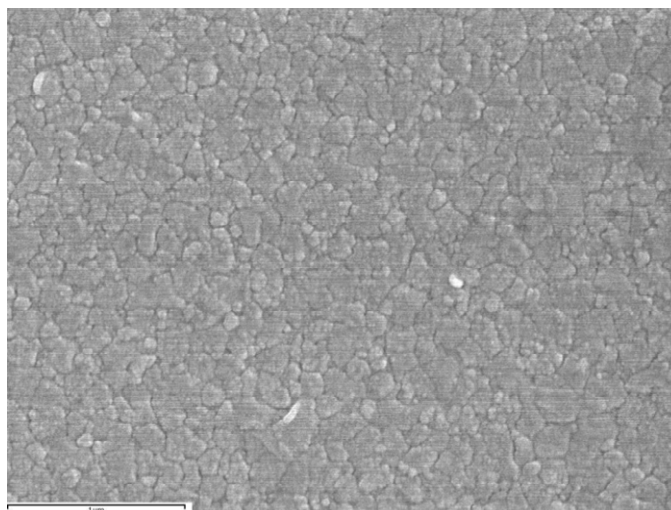


Figure 3.18 FE-SEM planar image of the Ba(Zr_{0.10}Ti_{0.90})O₃ thin film.

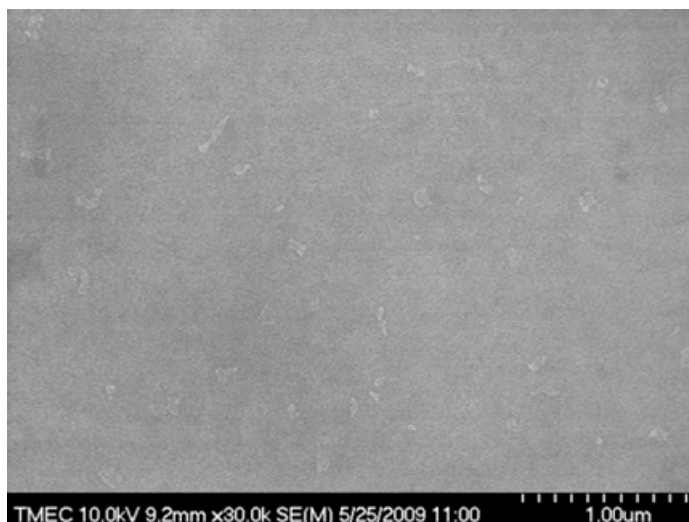


Figure 3.19 FE-SEM planar image of the Ba(Zr_{0.15}Ti_{0.85})O₃ thin film.

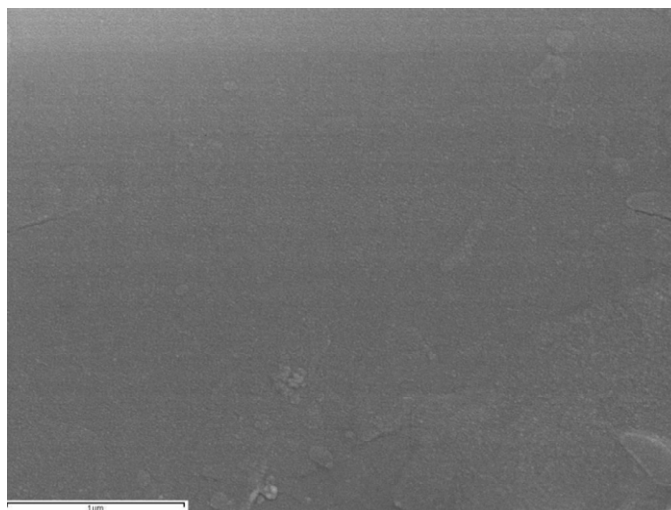


Figure 3.20 FE-SEM planar image of the Ba(Zr_{0.20}Ti_{0.88})O₃ thin film.

The surface morphologies were observed for using an area of $1\ \mu\text{m} \times 1\ \mu\text{m}$. The AFM images corresponding to the FE-SEM images were shown in figures 3.21-3.25. It is obvious the surface were smooth and the grain sizes of the films were about 40-100 nm.

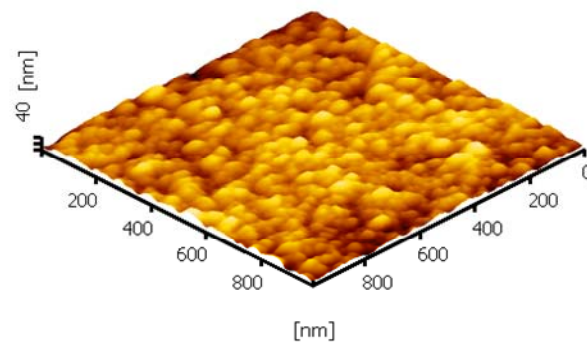


Figure 3.21 AFM planar image of the BaTiO₃ thin film

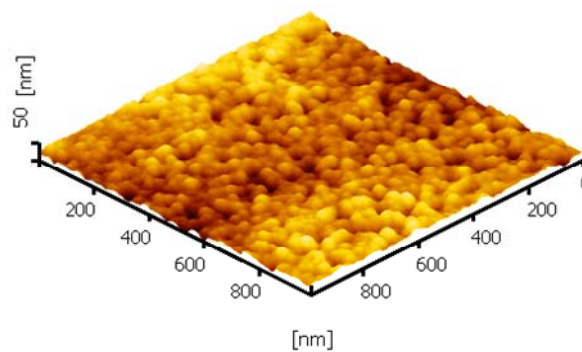


Figure 3.22 AFM planar image of the Ba(Zr_{0.05}Ti_{0.95})O₃ thin film.

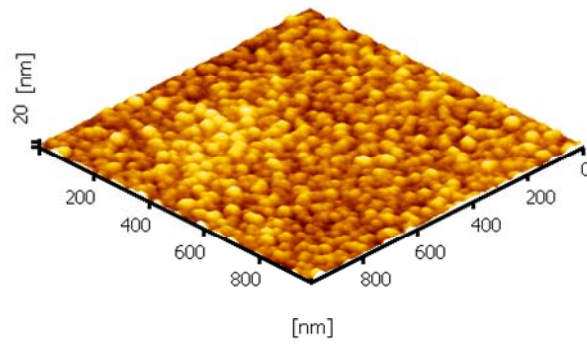


Figure 3.23 AFM planar image of the Ba(Zr_{0.10}Ti_{0.90})O₃ thin film.

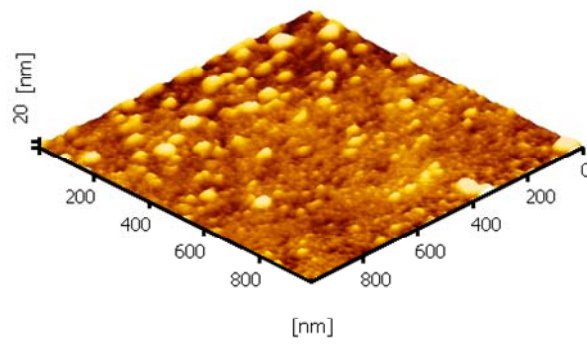


Figure 3.24 AFM planar image of the Ba(Zr_{0.15}Ti_{0.85})O₃ thin film

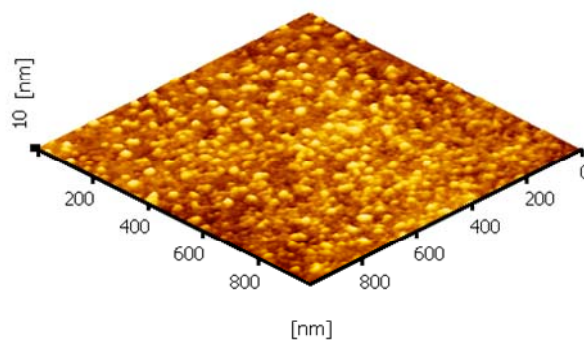


Figure 3.25 AFM planar image of the Ba(Zr_{0.20}Ti_{0.80})O₃ thin film.

3.4.5 Dielectric property and piezoelectric coefficient

The results of the dielectric constant and loss tangent were presented in figures 3.26-3.27. These values measured at 1 kHz for all the films were summarized in table 3.4. As frequency increase, the dielectric constant decreased because of the rapid reversal electric field preventing a charge orientation in the dielectric film. The dielectric loss increased with frequency due to the dielectric relaxation in the frequency range of 10^2 - 10^{10} Hz (Su *et al.*, 2003; Zhai *et al.*, 2004; Harlder *et al.*, 2005; Cheng *et al.*, 2006). The dielectric constant of the film increased with Zr content. This is because the measurements were performed at room temperature and was related to a shift in Curie temperature to lower temperature for higher content Zr as described in following chapter (chapter 5).

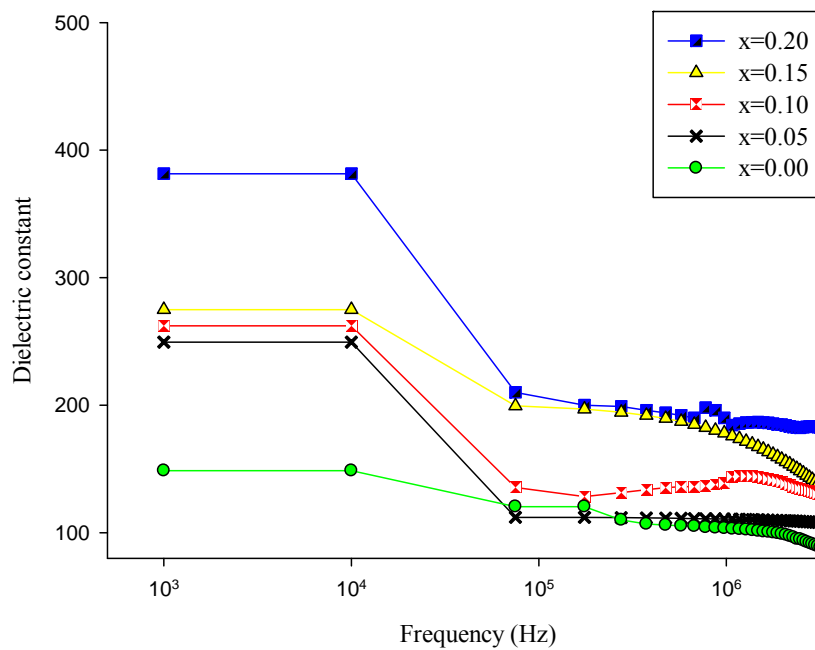


Figure 3.26 Variations of dielectric constant with frequency for the $\text{Ba}(\text{Zr}_x\text{Ti}_{1-x})\text{O}_3$ thin films with different compositions.

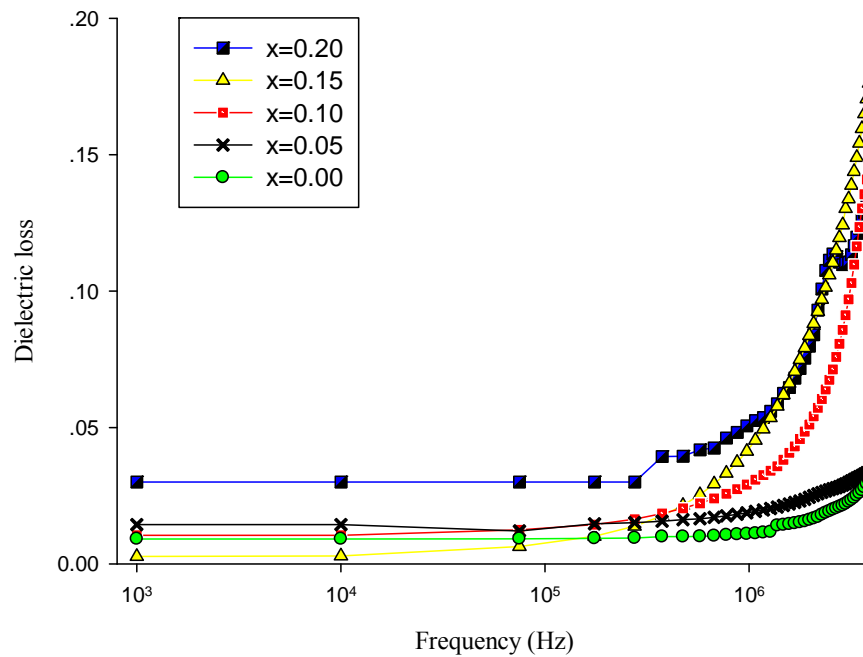


Figure 3.27 Variations of dielectric loss with frequency for the $\text{Ba}(\text{Zr}_x\text{Ti}_{1-x})\text{O}_3$ thin films with different compositions.

Table 3.4 The dielectric constant and dielectric loss measured at 1 kHz for the Ba(Zr_xTi_{1-x})O₃ thin films.

Ba(Zr _x Ti _{1-x})O ₃ thin films	Dielectric constant	Dielectric loss
x = 0.05	148.7	0.012
x = 0.05	250.0	0.014
x = 0.10	262.0	0.011
x = 0.15	275.0	0.027
x = 0.20	381.2	0.030

The piezoelectric response measured at 5 kHz for the BZT thin films was displayed in figures 3.28-3.31 by using equation (3.1) and substituting a slope of the graph, the piezoelectric coefficient d_{33} for each film was determined and listed in table 3.5

Table 3.5 The clamped values of the d_{33} coefficient for the poled Ba(Zr_xTi_{1-x})O₃ thin films.

Ba(Zr _x Ti _{1-x})O ₃ . thin films	Clamped d_{33} (pm/V)
x = 0.00	29.1 ± 0.5
x = 0.05	34.4 ± 0.5
x = 0.10	16.6 ± 0.5
x = 0.15	9.0 ± 0.5
x = 0.20	-

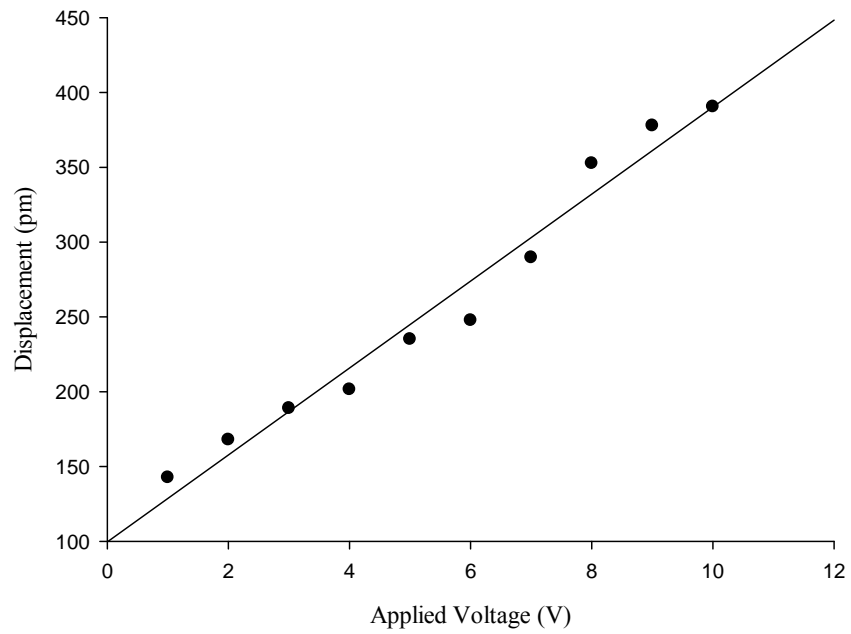


Figure 3.28 Variation of displacement with applied voltage for the BaTiO₃ thin film.

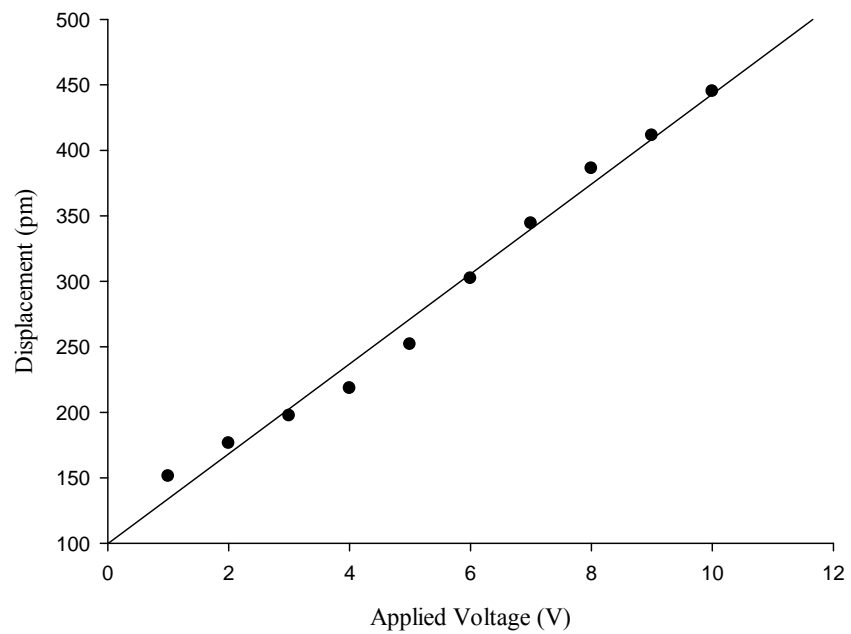


Figure 3.29 Variation of displacement with applied voltage for the Ba(Zr_{0.05}Ti_{0.95})O₃ thin film.

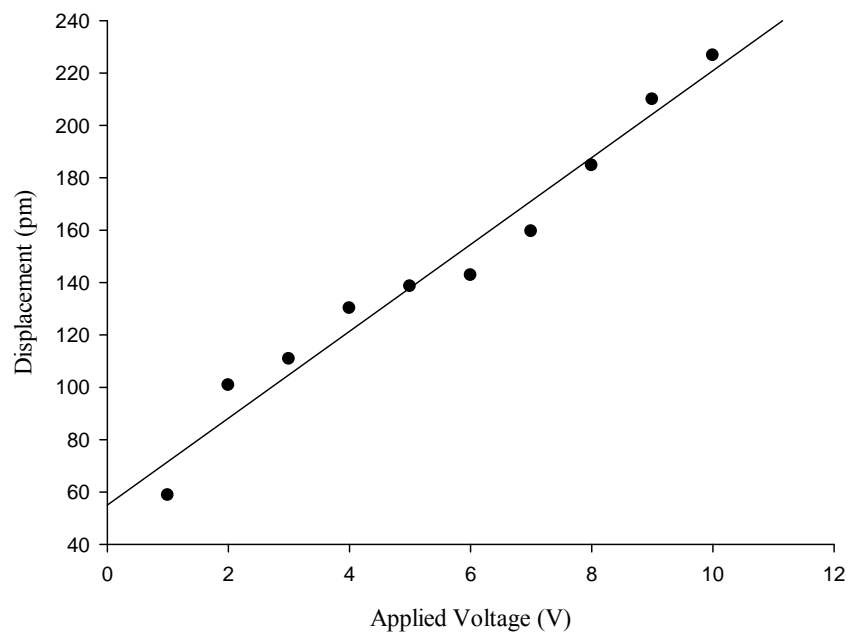


Figure 3.30 Variation of displacement with applied voltage for the $\text{Ba}(\text{Zr}_{0.10}\text{Ti}_{0.90})\text{O}_3$ thin film .

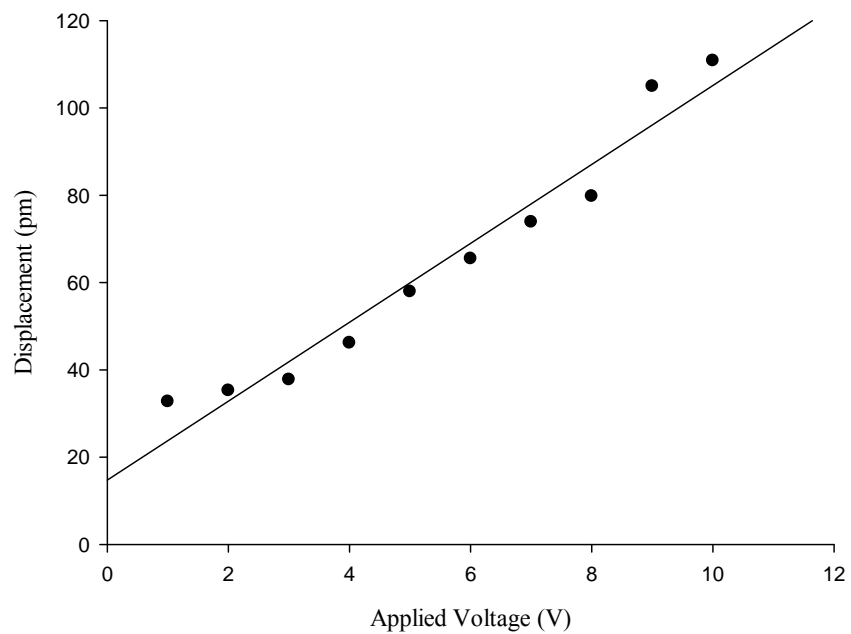


Figure 3.31 Variation of displacement with applied voltage for the $\text{Ba}(\text{Zr}_{0.15}\text{Ti}_{0.95})\text{O}_3$ thin film.

The resulting piezoelectric strain in the film produced a small displacement of the electrode surface of the film which in turn produced a small change in the intensity of the interference pattern. As can be seen, the d_{33} has its maximum of (34.4 ± 0.5) pm/V in $\text{Ba}(\text{Zr}_{0.05}\text{Ti}_{0.95})\text{O}_3$ thin film and this value was almost double the values in the $\text{Ba}(\text{Zr}_{0.10}\text{Ti}_{0.90})\text{O}_3$ and $\text{Ba}(\text{Zr}_{0.15}\text{Ti}_{0.85})\text{O}_3$ thin films. The d_{33} component associated with the extension and contraction of the film in the direction of the poling field which is perpendicular to the surface of the film. However, the spontaneous directions in a crystal are not always aligned with the poling field. There are different possible polar directions in different crystal structures. The tetragonal, orthorhombic and rhombohedral structures respectively have six, twelve and eight polar directions (ANSI/IEEE Std 180-1986; Dixit *et al.*, 2003). The higher the number of polarizable directions aligned to a poling field means the larger the piezoelectric coefficient obtained. In addition, the spontaneous polarization depends strongly on crystal symmetry. A crystalline-phase structure containing the polar axis aligned along the crystal symmetry possesses high piezoelectric coefficient. From these concepts the $\text{Ba}(\text{Zr}_{0.05}\text{Ti}_{0.95})\text{O}_3$ was therefore identified to be orthorhombic while both $\text{Ba}(\text{Zr}_{0.10}\text{Ti}_{0.90})\text{O}_3$ and $\text{Ba}(\text{Zr}_{0.15}\text{Ti}_{0.85})\text{O}_3$ thin films were rhombohedral.

3.5 Conclusions

This work has adapted reliable procedures to develop promising BZT thin films. The BZT thin films with different Zr/Ti ratios deposited on commercial Pt/Ti/SiO₂/Si substrates have an average thickness of 350 ± 50 nm. According to TGA and XRD results the suitable pyrolysis of the films is 350 °C and the annealing 800 °C. All the films crystallized into perovskite structure without pyrochlore. This work intently studied the crystallographic data for all the films. The confirmation of crystal structure for the thin films of different Zr/Ti ratios has been made as follows: the thin film without Zr crystallized into tetragonal perovskite whereas $\text{Ba}(\text{Zr}_{0.05}\text{Ti}_{0.95})\text{O}_3$ is orthorhombic. It is rhombohedral for both $\text{Ba}(\text{Zr}_{0.10}\text{Ti}_{0.90})\text{O}_3$ and $\text{Ba}(\text{Zr}_{0.15}\text{Ti}_{0.85})\text{O}_3$. Finally, $\text{Ba}(\text{Zr}_{0.20}\text{Ti}_{0.80})\text{O}_3$ is cubic. Unlike most of the PZT thin film, the BZT thin films have non-columnar microstructure with the average grain size decreased with increasing Zr content. The permittivity of the film increased with

Zr contents with a very low dielectric loss. The values of the dielectric constant for all the BZT thin films are comparable to the BZT films fabricated by rf magnetron sputtering but higher than those obtained by a chemical spin-coating technique (Wu, Wu and Chen, 1996; Pontes *et al.*, 2004). These values are of the same each those of the lead-free ones (Harlder *et al.*, 2005; Liang and Wu, 2005). The piezoelectric property of BZT were characterizing by the single-beam Michelson interferometer. The Ba(Zr_{0.05}Ti_{0.95})O₃ thin film exhibits the best piezoelectric response and its clamped piezoelectric coefficient d_{33} is 35 pm/V. This value is comparable to the maximum d_{33} value of Ba(Zr_{0.05}Ti_{0.95})O₃ thin film characterized by Halder *et al.*, (2005).

As mentioned earlier in the chapter, the miniaturizations of MEMS products require piezoelectric thin film. These are, for example, thin films of 100 nm or less for dynamic random access memory (DRAM) applications. The BZT thin films produced in this work are probably introduced in such applications.

CHAPTER 4

BARIUM ZIRCONATE TITANATE POWDERS

This chapter describes herein the fabrication of the BZT powders by sol-gel process. The BZT powders were characterized crystalline phase and particle size. An effect of sintering additive on BZT powder is studied. The knowledge of correlations between the preparation conditions and properties of the BZT is then applied to the BZT ceramics described in chapter 5.

4.1 Introduction

Due to increasing concerns regarding environment and public health, the piezoceramics of lead-free compositions have been highly desirable in order to replace or reduce the use of the lead-based materials. Barium zirconate titanate or $\text{Ba}(\text{Zr}_x\text{Ti}_{1-x})\text{O}_3$, BZT) is one of the promising candidates as it is derived from two non-lead perovskite substances, i.e., barium titanate (BaTiO_3) and barium zirconate (BaZrO_3). There have been reports that the zirconium substitution in the titanium lattices enhances the dielectric and piezoelectric properties (Yu *et al.*, 2002; Tang *et al.*, 2004). The BZT-based materials, therefore, have a high potential for using as active elements in today technologies and nano- or micro-fabrication processes (Yu *et al.*, 2002; Tang *et al.*, 2004). In promoting the product for development, the importance factor in using the materials of fine particle sizes with homogeneous distribution must be taken into account.

4.2 Review of previous work

The preparation for homogeneous powders needs to control the two most critical factors, which are temperature and time. Powder processing involves the control of both particle size and mixing rate, no matter what the starting materials are powders or partly reacted powders (Wang and Chen, 2006).

Generally, the chemical reactions are limited by diffusion at atomic level. It is necessary to take into account the prior production of fine and well mixed particles. In the sol-gel techniques described in chapter 3. The sol describes the dispersion of colloids in liquids. If the viscosity of the sol is made to increase sufficiently, e.g., by partial loss of the liquid phase, it becomes a rigid gel. Sol-gel method is a typically wet chemical method to make the particles by chemical in solution starting with metal oxide as the precursor. Sol-gel techniques are also used for several purposes including the formation of fine powders homogeneous thin and thick films, fibers, homogeneous bulk material, porous solid, and powder. This project used the sol-gel process for producing uniform mixtures of fine particles as presented in this chapter.

Increasing in miniaturization and integration of the films in the electronic device industry leads to the formation of thinner layers in order to obtain more area per unit volume. However, the decrease in layer thickness leads to the dielectric breakdown and electrical degradation under DC field stress. In order to reduce the layer thickness the powders have to be developed (Setter, 2001). The well-defined morphology also decreases the sintering temperature. This also allows the use of less expensive conductors and reduces the energy consumption instead of using expensive electrode materials such as platinum or palladium. (Valant *et al.*, 2006).

Veith *et al.*, (2000) prepared nanopowder of BZT via alkoxide and semi-alkoxide (hydroxide and acetate) routes. Each process used different starting materials. A temperature required for the decomposition of the intermediates of semi-alkoxide precursors higher than that of alkoxide one. On the other hand, the semi-alkoxide routes are rather simple and suitable for large scale synthesis of perovskites. But it is possible that the final ceramic material is contaminated with small amounts of undesired phases especially in the case of acetate route.

Tang *et al.*, (2004) prepared powder of $\text{Ba}(\text{Zr}_{0.2}\text{Ti}_{0.8})\text{O}_3$ by using the sol-gel method. The dry gel was annealed at 1,100 °C for 5 h and after grinding, BZT powders were obtained. The annealed powders were pressed into disks. The pellets were sintered at 1,300-1,550 °C for 5 h and cooled in a furnace.

Qi *et al.*, (2006) reported the relationship between the lattice parameter and Zr content of the powders. As shown in a previous chapter (chapter 2, figure 2.11).

Chen *et al.*, (2010) prepared Ba(Zr_{0.2}Ti_{0.8})O₃ nano powder by sol-gel method. The obtained nano powders were calcined at 700, 800 and 900 °C for 4 h. The suitable calcined is 900 °C for 4 h due to the absence of BaCO₃ it can be implied that this is the temperature necessary for forming BZT single perovskite phase. The lattice parameter obtained from XRD pattern the *c/a* ratio about 1.005-1.017 from this result it can be concluded that the structure of Ba(Zr_{0.2}Ti_{0.8})O₃ powder is cubic. The crystalline size of Ba(Zr_{0.2}Ti_{0.8})O₃ powder were calculated from the Scherrer equation ranging from 20.6-22.2 nm corresponding to TEM image which the average grain size about 20-28 nm, respectively.

4.3 Materials and methods

4.3.1. Preparation of the Ba(Zr_xTi_{1-x})O₃ powders

The sol-gel route (Jewei *et al.*, 2004 and Zhai *et al.*, 2004) of barium acetate, zirconium isopropoxide and titanium isopropoxide starting materials was used. Acetic acid, 2-Methoxyethanol (2-ME) were the solvents. Poly ethyleneglycol (C_{2n+2}H_{4n+6}O_{n+2}, Poch) was used as surfactant; it was dissolve in precursor solution. The preparation procedure was described in chapter 3. A clear gel was obtained after the removal of volatiles in vacuum and kept in an oven until dried. Different temperatures starting from 700 °C to 1,100 °C for 2 h were used in calcination. The preparation procedure was shown in figure 4.1.

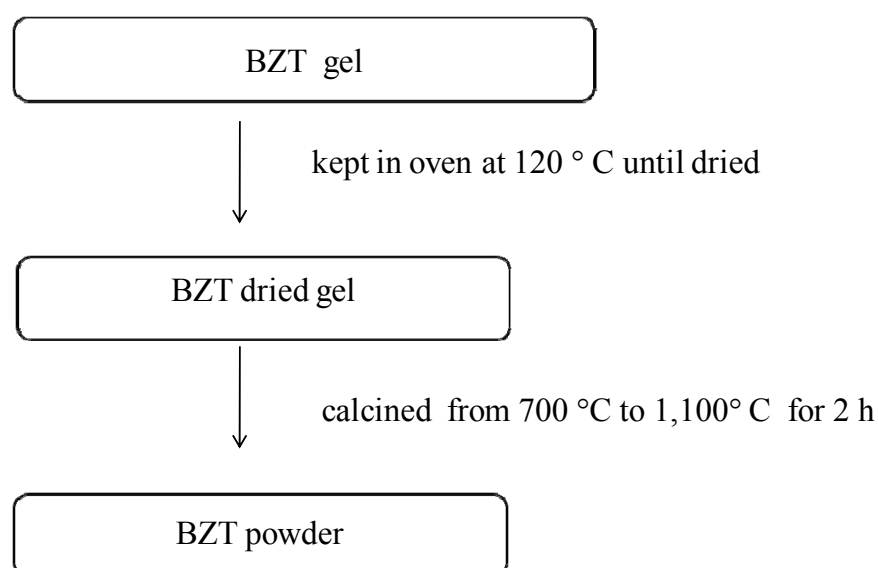


Figure 4.1 Preparation procedure for the BZT powder.

4.3.2 *Low-temperature synthesized $Ba(Zr_{0.05}Ti_{0.95})O_3$ powder*

The BZT of composition of best piezoelectric properties was modified with sintering additive and studied its influence on the obtained powder. The dried gel was added 1.5 wt% of lithium oxide powder (Li_2O , Aldrich, 97% purity) and homogeneously mixed by ball milling 3 h before calcined at a temperature of 700 °C for 10 h by ball-milling for 3 h as shown in figure 4.2.

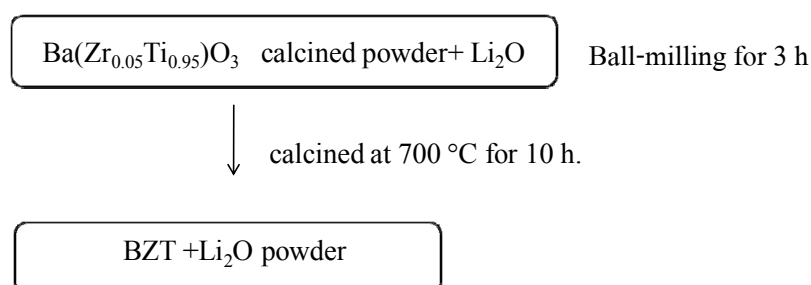


Figure 4.2 Preparation procedure for the $Ba(Zr_{0.05}Ti_{0.95})O_3$ with sintering additive powder.

4.4 Characterization of the $\text{Ba}(\text{Zr}_x\text{Ti}_{1-x})\text{O}_3$ powders

XRD Diffractometer (PHILLIPS X'pert MPD) with Ni filtered CuK_α radiation, Raman Spectroscope (NT_MDT; NTEGRA spectra), the particle size distribution were carried on Mastersizer 2000 Version 5.1 (MALVERM).

4.5 Results and discussion

4.5.1 XRD patterns, Raman spectroscopic data and TEM analysis

4.5.1.1 XRD patterns

The crystallographic data from the XRD results indicate that the calcination at 700-900 ° C the BaTiO_3 powders has cubic perovskite structure (ICDD reference pattern: 01-075-0461). When increasing the temperature to 1,000 ° C the BaTiO_3 powder has tetragonal perovskite structure (ICDD reference pattern: 01-089-1428) (figure 4.3). For the $\text{Ba}(\text{Zr}_{0.20}\text{Ti}_{0.80})\text{O}_3$ powder, it displays the cubic phase (ICDD reference pattern: 00-036-0019) as shown in figure 4.4.

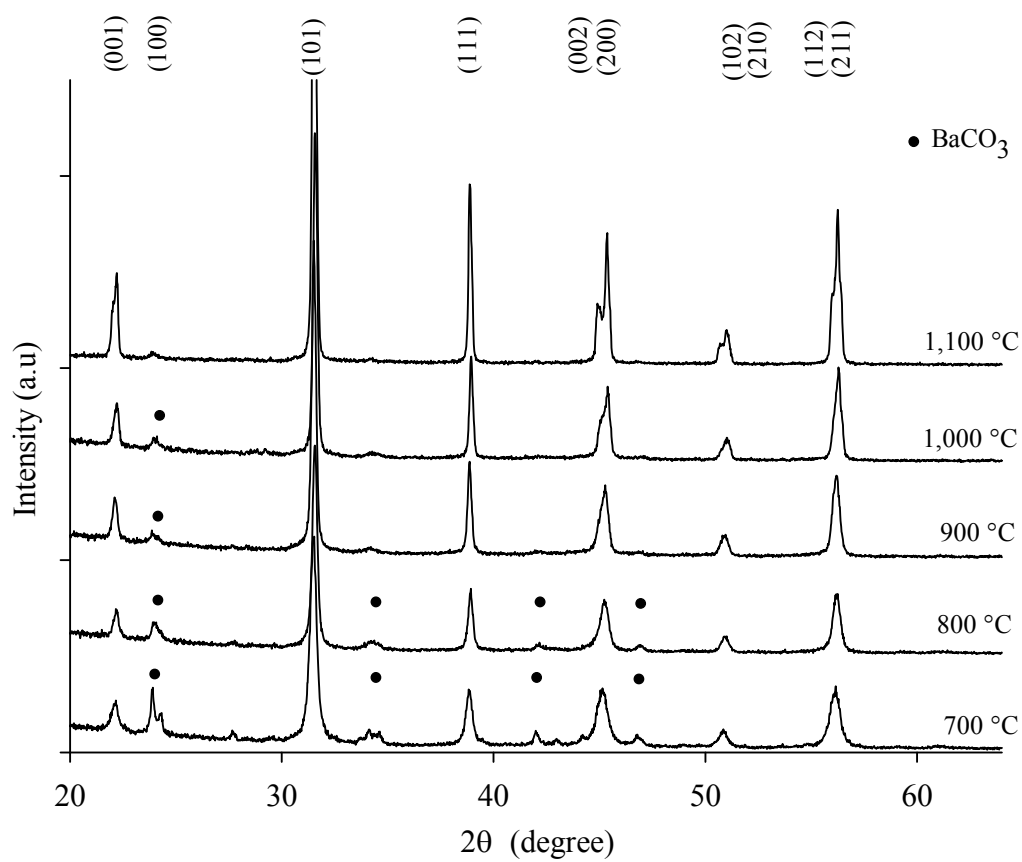


Figure 4.3 XRD patterns of the BaTiO₃ powder calcined at various temperatures.

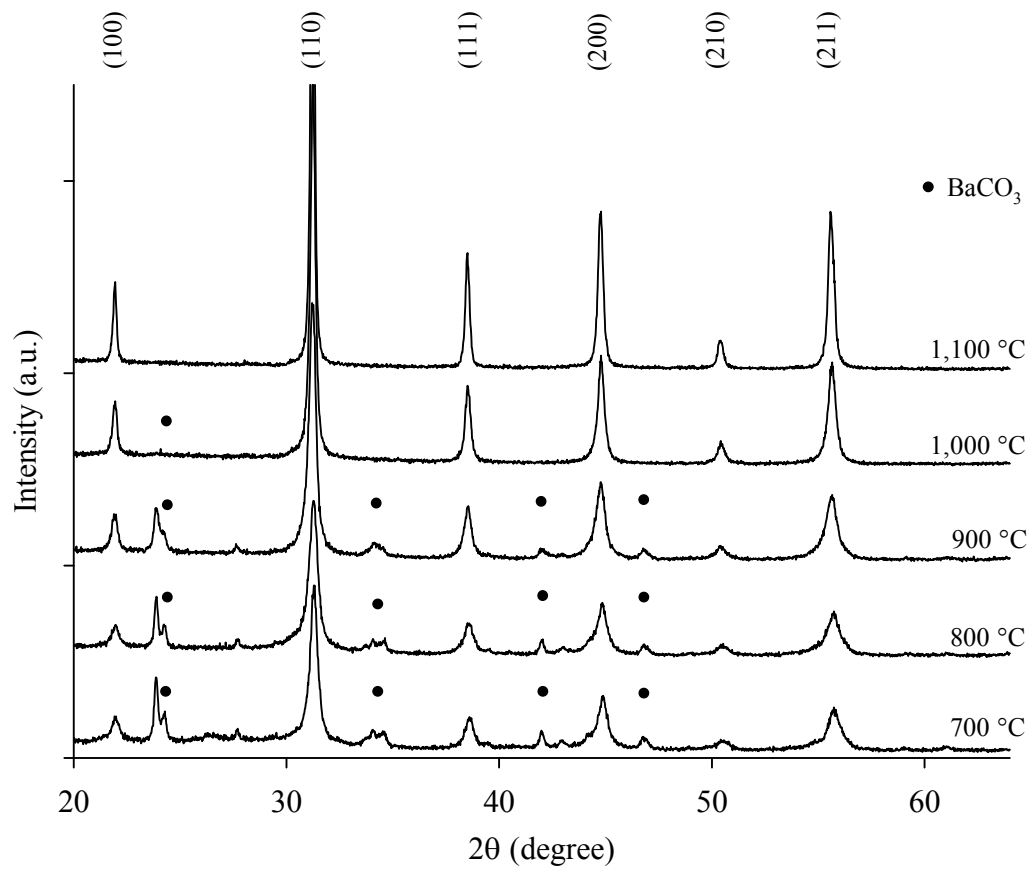


Figure 4.4 XRD patterns of the Ba(Zr_{0.20}Ti_{0.80})O₃ powder calcined at various temperatures.

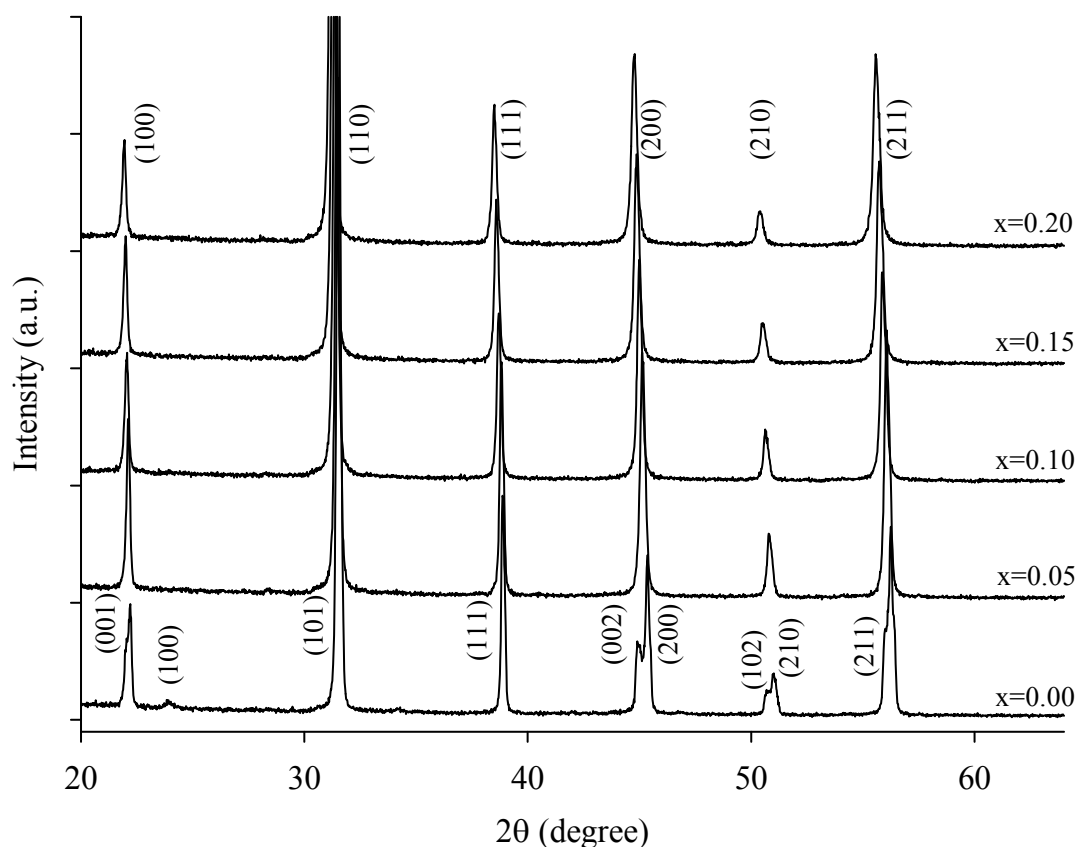


Figure 4.5 XRD patterns of the Ba(Zr_xTi_{1-x})O₃ powders calcined at 1,100 ° C for 2h.

The BZT powders calcined at 1,100 ° C for 2h were XRD analyzed as displayed in figure 4.5. The powder without zirconium has the tetragonal phase which is noticeable from the splitting XRD peaks (ICDD reference pattern: 01-089-1428), and the Ba(Zr_{0.20}Ti_{0.80})O₃ powder shows the cubic phase (ICDD reference pattern: 00-036-0019). Figure 4.6 summarizes all the calculated latticed constants of the BZT powders and shows that the lattice constants increased with the zirconium content. This agreed well with the report by Qi *et al.* (2006). The samples at other compositions, i.e., 0 < x < 0.2, was further identified based on the Raman Spectroscopic data.

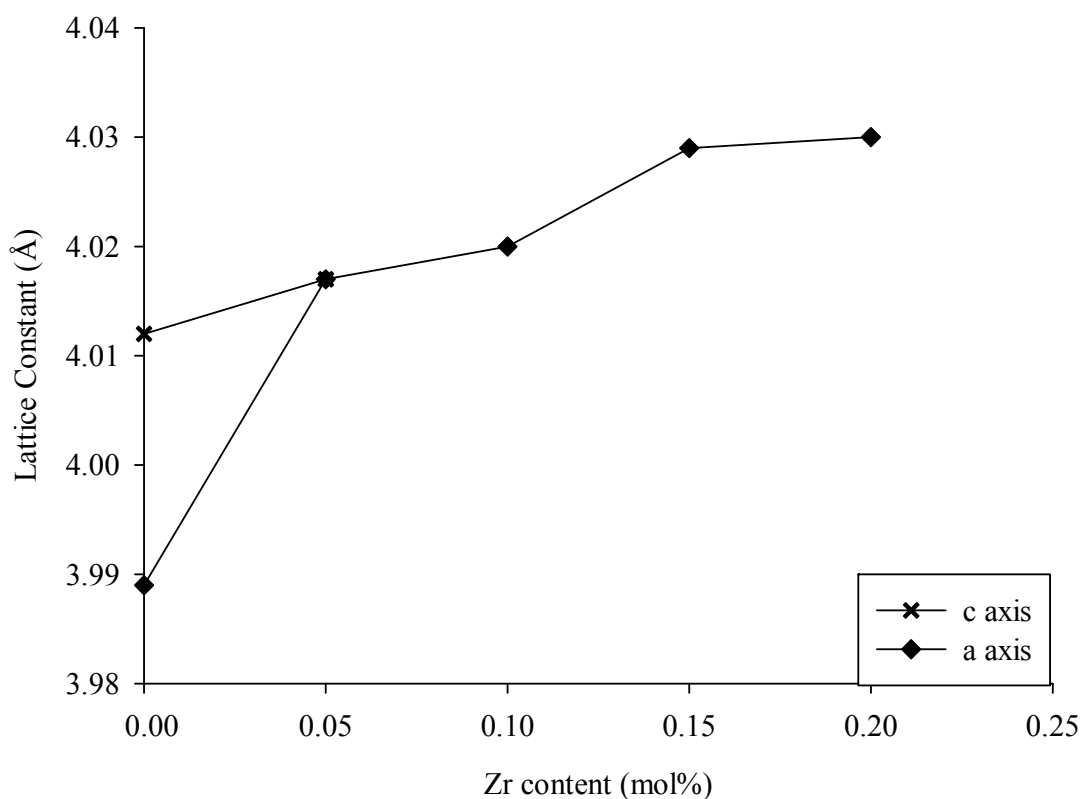


Figure 4.6 Calculated lattice constants as a function of the $\text{Ba}(\text{Zr}_x\text{Ti}_{1-x})\text{O}_3$ calcined powders at various Zr contents.

4.5.1.2 Raman spectroscopic data

The Raman spectrum at room temperature (figures 4.7-4.9) were presented to clarify the crystalline phase for the BZT with compositions of $0 < x < 0.2$. Owing to the random grain orientation of the BZT powders, the direction of the phonon wave vectors radiate randomly from one grain to the others with respect to the crystallographic axes (Moura *et al.*, 2008; Dobal *et al.*, 2001). As observed, when the Zr content reached 10 mol%, consideration this mode frequency is expected to be about 129 $1/\text{cm}$ for Zr replacing Ti sites, which will be reduced further by an increase in the ionic radius [$R(\text{Ti}^{4+}) = 0.0745 \text{ nm}$, $R(\text{Zr}^{4+}) = 0.086 \text{ nm}$]. The additional mode could therefore be associated with a normal mode involving Zr atoms. Since this mode disappears in the $\text{Ba}(\text{Ti}_{0.90}\text{Zr}_{0.10})\text{O}_3$ and $\text{Ba}(\text{Ti}_{0.85}\text{Zr}_{0.15})\text{O}_3$ compositions, it may be considered an indication of the orthorhombic to rhombohedral phase transition.

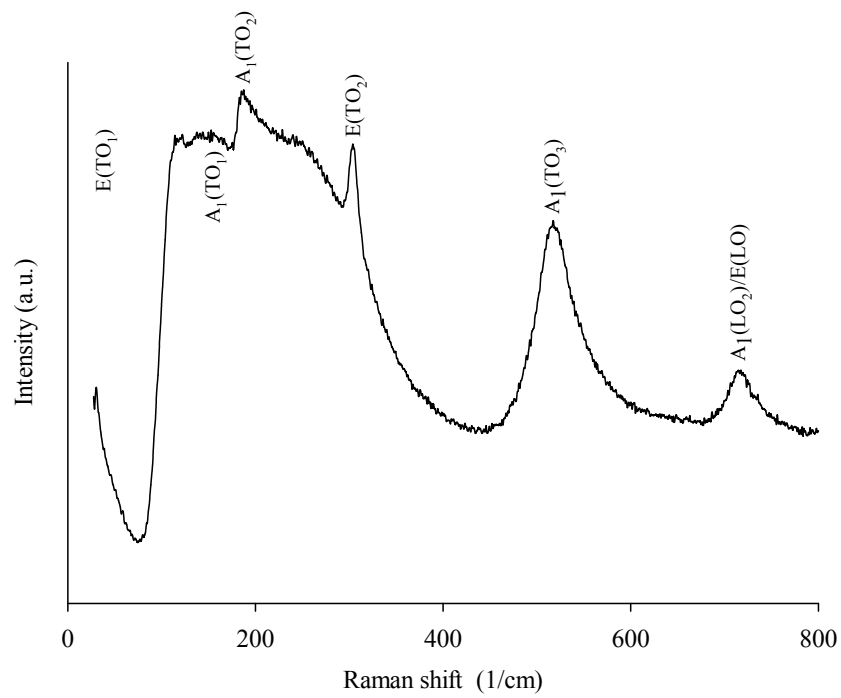


Figure 4.7 Raman spectra of the $\text{Ba}(\text{Zr}_{0.05}\text{Ti}_{0.95})\text{O}_3$ powder calcined at $1,100\text{ }^\circ\text{C}$ for 2 h.

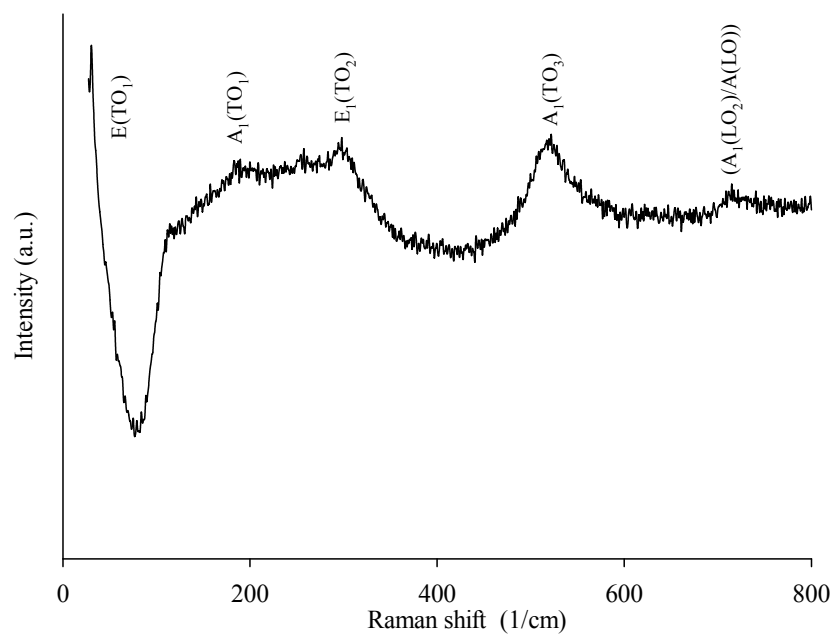


Figure 4.8 Raman spectra of the $\text{Ba}(\text{Zr}_{0.10}\text{Ti}_{0.90})\text{O}_3$ powder calcined at $1,100\text{ }^\circ\text{C}$ for 2 h.

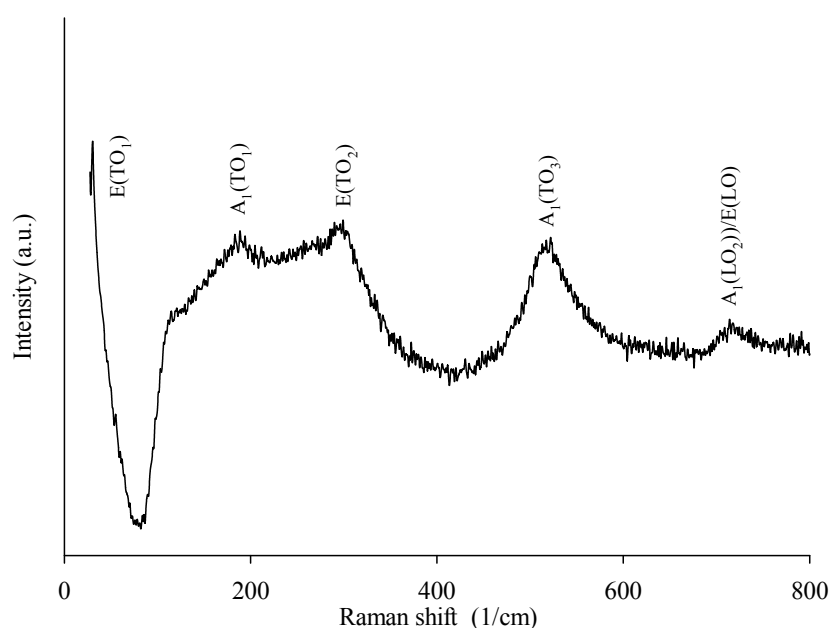
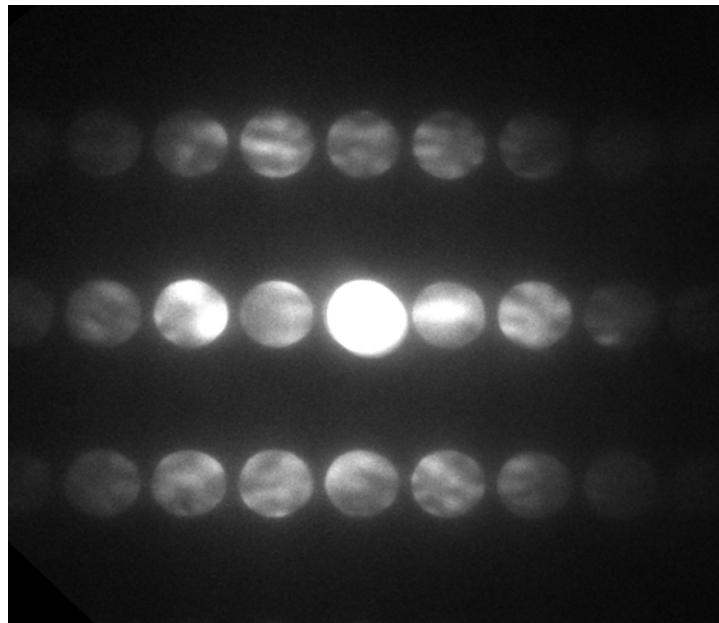


Figure 4.9 Raman spectra of the $\text{Ba}(\text{Zr}_{0.15}\text{Ti}_{0.85})\text{O}_3$ powder calcined at $1,100\text{ }^\circ\text{C}$ for 2 h.

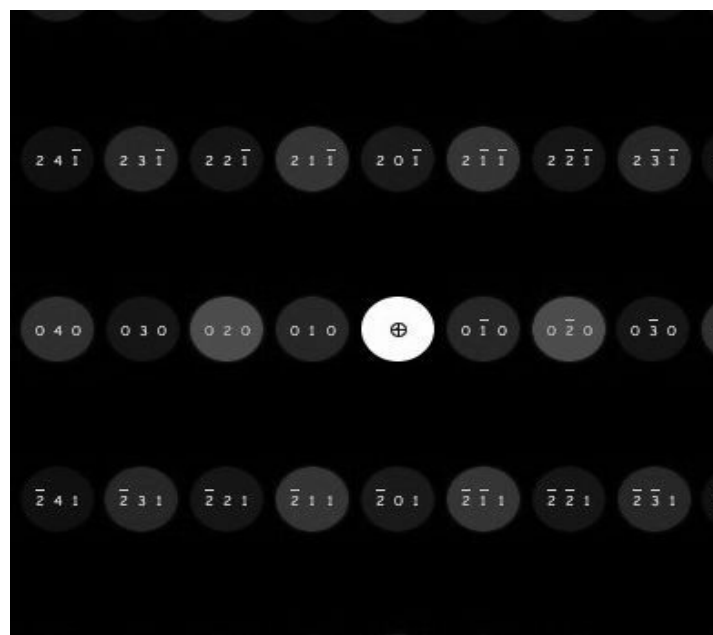
4.5.1.3 TEM analysis

The crystal structure of $\text{Ba}(\text{Zr}_{0.05}\text{Ti}_{0.95})\text{O}_3$ powder could be observed and analyzed by TEM technique using convergent-beam electron diffraction (CBED) mode. Comparison between CBED pattern obtained and simulation from simulation program “JEMS” were taken to confirm the information of the BZT structure (Yordsri *et al.*, 2011).

The CBED patterns of $\text{Ba}(\text{Zr}_{0.5}\text{Ti}_{0.95})\text{O}_3$ powder and the simulation were shown in figure 4.10 and 4.11. Two zone-axis CBED patterns were taken from the same area of $\text{BaZr}_{0.5}\text{Ti}_{0.95}\text{O}_3$ to indicate the structure shown in figure 4.10(a) [102] zone axis pattern and figure 4.10 (b), the simulated patterns by JEMS. The [001] zone axis pattern displayed in figure 4.11 (a) corresponding to the pattern the simulated pattern in figure 4.11 (b).

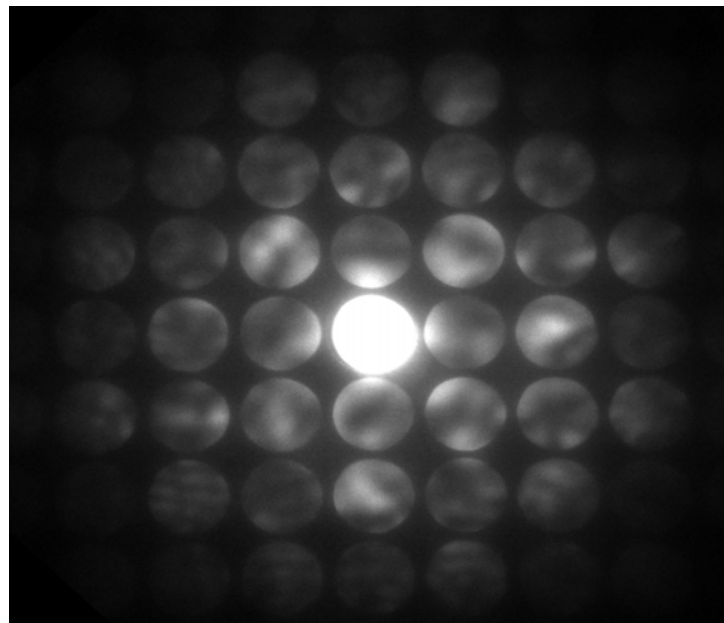


(a)

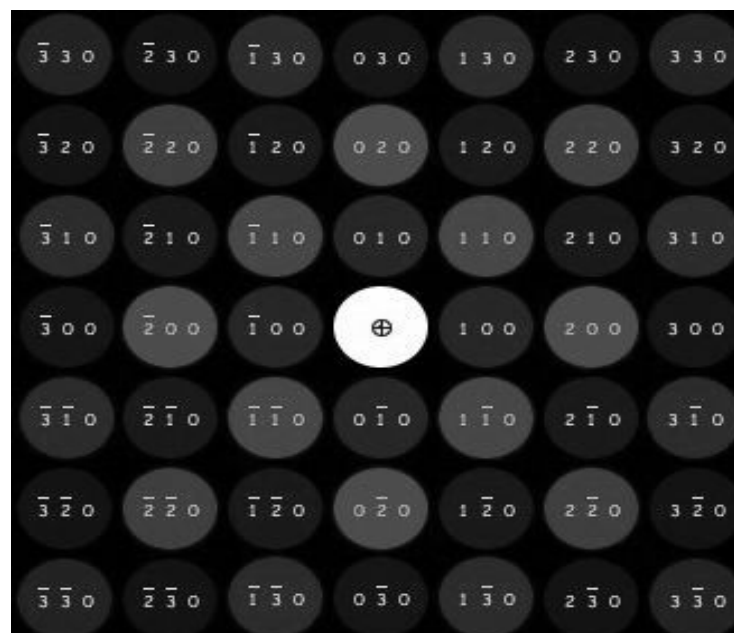


(b)

Figure 4.10 CBED patterns (a) and simulated (b) images for $[102]$ zone axis of $\text{Ba}(\text{Zr}_{0.05}\text{Ti}_{0.95})\text{O}_3$ powder.



(a)



(b)

Figure 4.11 CBED patterns (a) and simulated (b) images for $[001]$ zone axis of $\text{Ba}(\text{Zr}_{0.05}\text{Ti}_{0.95})\text{O}_3$ powder.

4.5.2 Particle size characterization

4.5.2.1 XRD patterns

The crystalline size for all the BZT powders after calcinations was calculated by using equation 4.1 and the (111) peak was chosen for the calculation. Table 4.1 lists all the results

$$d_{XRD} = \frac{0.89\lambda}{\beta \cos \theta} \quad (4.1)$$

Where λ is the wavelength of Cu-K α radiations (1.54 Å), β is the full width at half maximum of the peak and θ is the angle obtained from 2θ value corresponding to maximum intensity peak of XRD patterns.

Table 4.1 The crystalline size of the Ba(Zr $_x$ Ti $_{1-x}$)O $_3$ powders.

Ba(Zr $_x$ Ti $_{1-x}$)O $_3$ powders	Crystalline size (nm)
x = 0.00	62
x = 0.05	63
x = 0.10	56
x = 0.15	43
x = 0.20	50

4.5.2.2 Laser particle size analyzer

In order to enhance the distribution of the calcined powder, the ultrasonic mixer was used and the particle size distributions were as shown in figures 4.12-4.16. A broad peak distribution ranging from 10 to 100 μm , including a small portion of the powder with particle size larger than 100 μm could be observed for all compositions. This means that there are the agglomerations of the powder after calcinations.

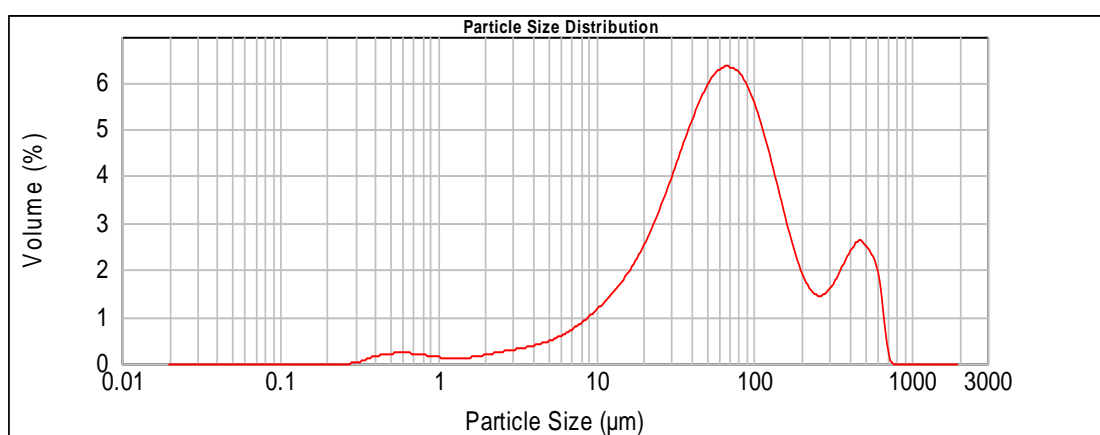


Figure 4.12 Particle size distribution of the BaTiO_3 calcined powder.

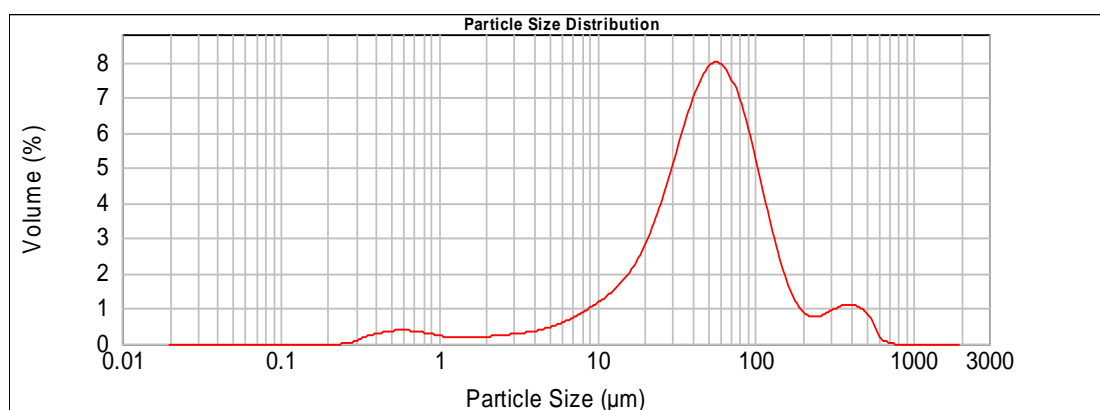


Figure 4.13 Particle size distribution of the $\text{Ba}(\text{Zr}_{0.05}\text{Ti}_{0.95})\text{O}_3$ calcined powder.

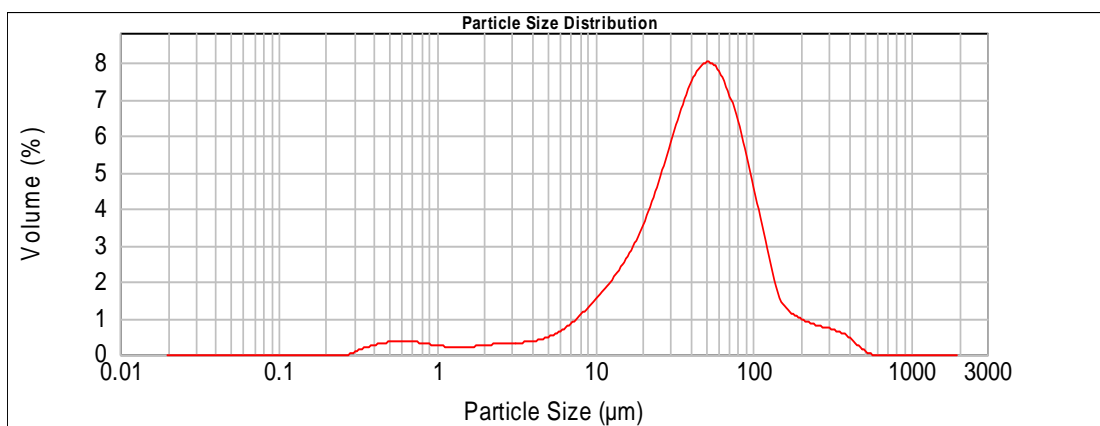


Figure 4.14 Particle size distribution of the $\text{Ba}(\text{Zr}_{0.10}\text{Ti}_{0.90})\text{O}_3$ calcined powder.

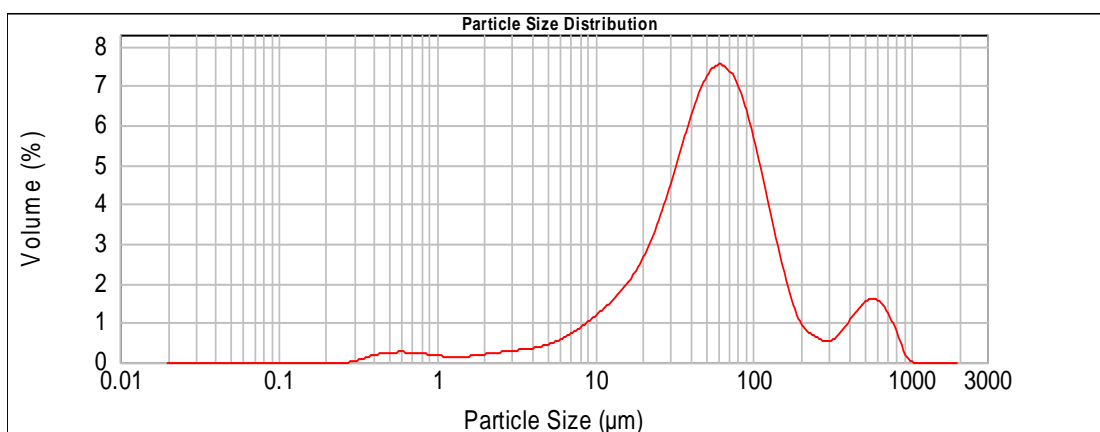


Figure 4.15 Particle size distribution of the $\text{Ba}(\text{Zr}_{0.15}\text{Ti}_{0.85})\text{O}_3$ calcined powder.

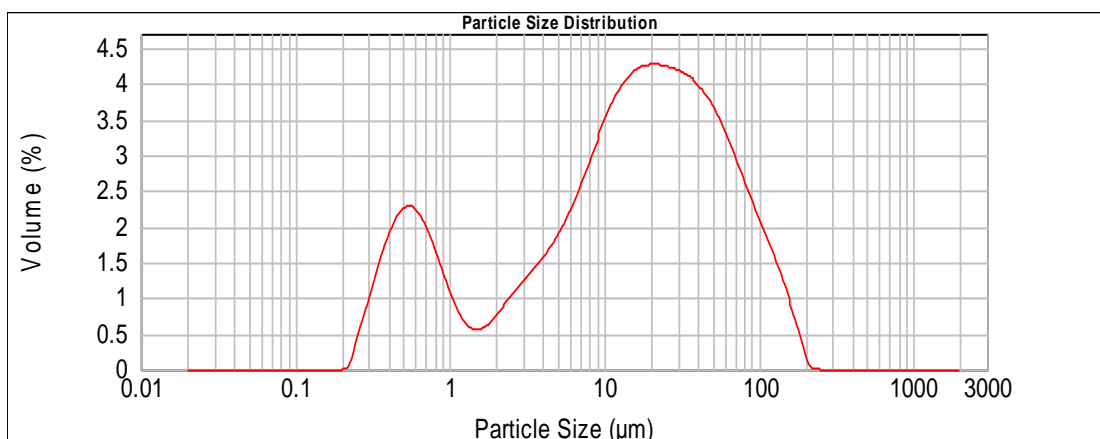


Figure 4.16 Particle size distribution of the $\text{Ba}(\text{Zr}_{0.20}\text{Ti}_{0.80})\text{O}_3$ calcined powder.

4.5.3 Effect of sintering additive

The Li_2O was added in the gel of $\text{Ba}(\text{Zr}_{0.05}\text{Ti}_{0.95})\text{O}_3$ before calcinations. Therefore, the effect of the additive on the properties was investigated. For comparison purpose, figure 4.17 displays the XRD patterns of $\text{Ba}(\text{Zr}_{0.05}\text{Ti}_{0.95})\text{O}_3$ powders with and without Li_2O . In both compositions, the main crystalline phase is perovskite. However, a small amount of Li_2O resulted in the second phase of the BaCO_3 (ICDD reference pattern: 01-071-2394) as observed in figure 4.17.

The TGA analysis was carried out for the $\text{Ba}(\text{Zr}_{0.05}\text{Ti}_{0.95})\text{O}_3$ gel without Li_2O and for the calcined powder of $\text{Ba}(\text{Zr}_{0.05}\text{Ti}_{0.95})\text{O}_3$ with 1.5 wt% Li_2O . The results were shown comparatively in figure 4.18. A relatively high weight loss occurred in the $\text{Ba}(\text{Zr}_{0.05}\text{Ti}_{0.95})\text{O}_3$ gel during the heat treatment. A lower weight loss in the Li_2O doped powder was observed because the powder was calcined. In both cases, the thermal analysis contained three common mechanism of thermal decomposition: solvents removing, organic complex decomposing and BZT phase form. A further increase in the sintering temperature promotes the formation of BZT, without the novel chemical reactions took place.

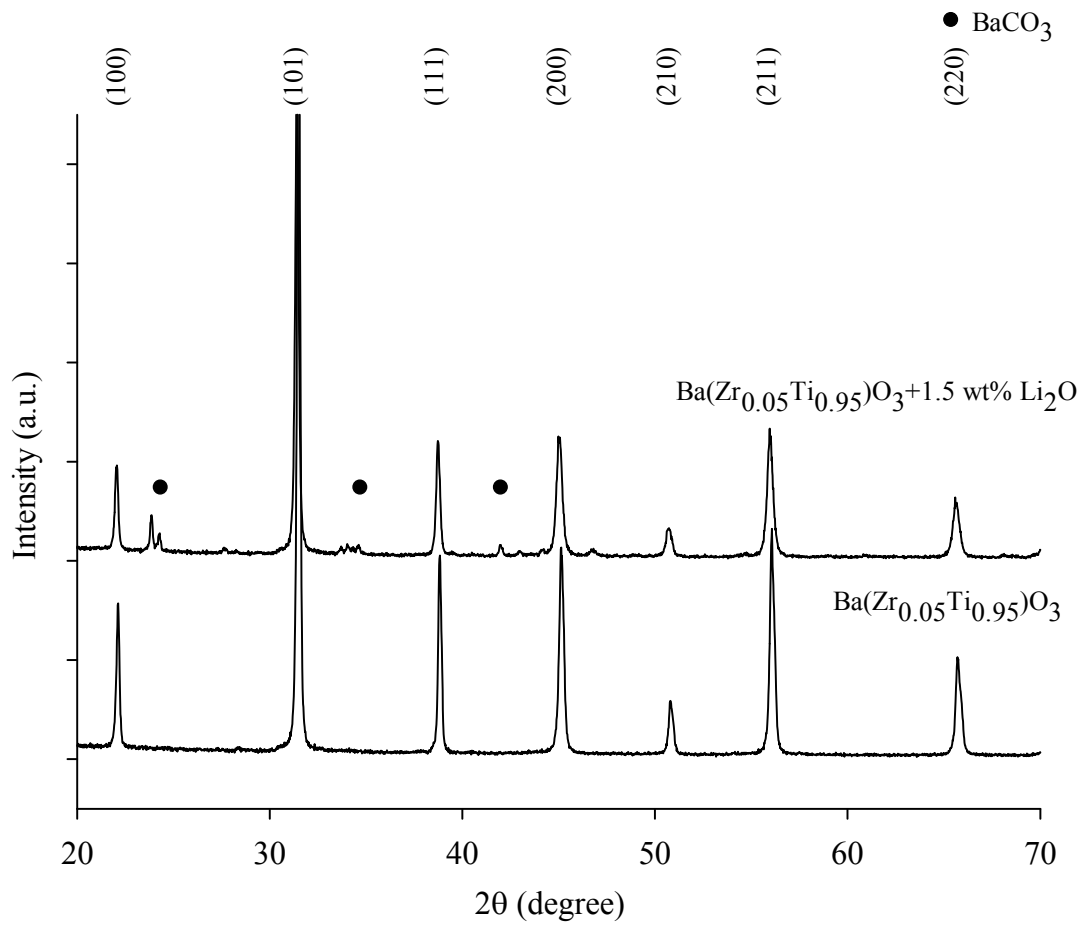


Figure 4.17 XRD patterns of Ba(Zr_{0.05}Ti_{0.95})O₃ powder calcined at 1,100° C for 2 h and Ba(Zr_{0.05}Ti_{0.95})O₃ with 1.5 wt% Li₂O powder calcined at 700 ° C for 10 h.

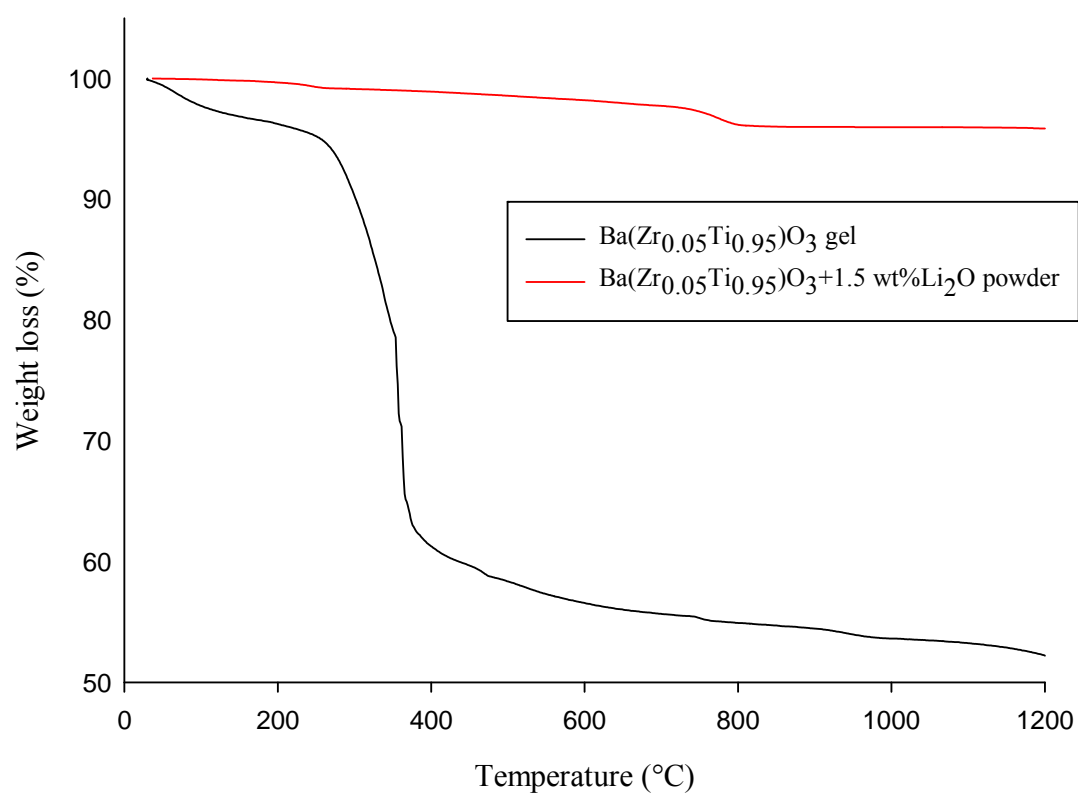


Figure 4.18 TGA patterns of the Ba(Zr_{0.05}Ti_{0.95})O₃ gel and the Ba(Zr_{0.05}Ti_{0.95})O₃ with 1.5 wt% Li₂O powder calcined at 700 °C for 10 h.

Based on the Raman spectrum at room temperature, the crystalline phase of the $\text{Ba}(\text{Zr}_{0.05}\text{Ti}_{0.95})\text{O}_3$ with 1.5 wt% Li_2O was identified to orthorhombic phase. The addition of Li_2O showed no effect on the phase of the sample as confirmed by the results in figures 4.19. In addition, it was able to calcine the $\text{Ba}(\text{Zr}_{0.05}\text{Ti}_{0.95})\text{O}_3$ with 1.5 wt% Li_2O at 700 °C and obtain the same crystalline phases as 1,100 °C-calcined sample. This means that the surface energy of the particle is higher in the Li_2O -added sample led to the lower calcination and sintering temperature.

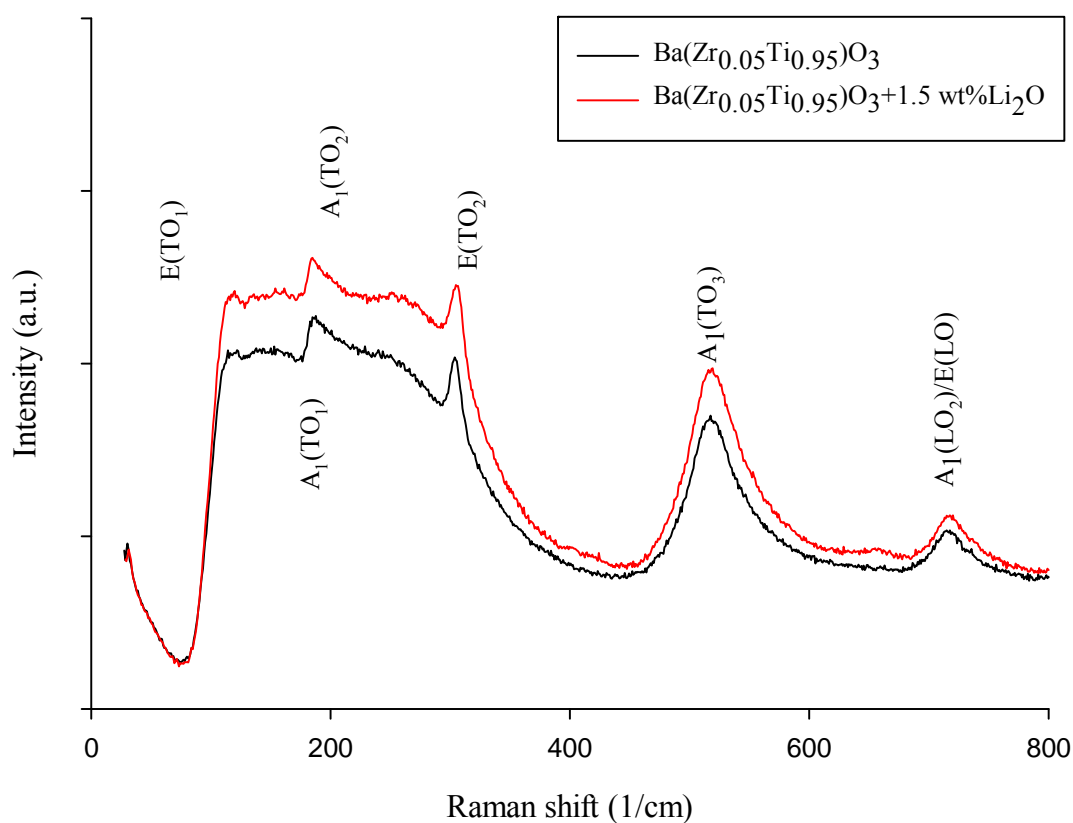


Figure 4.19 Raman spectras of the $\text{Ba}(\text{Zr}_{0.05}\text{Ti}_{0.95})\text{O}_3$ powder calcined at 1,100 °C for 2 h and $\text{Ba}(\text{Zr}_{0.05}\text{Ti}_{0.95})\text{O}_3$ powder with 1.5 wt% Li_2O calcined 700 °C for 10 h.

The particle sizes of the powders of $\text{Ba}(\text{Zr}_{0.05}\text{Ti}_{0.95})\text{O}_3$ and $\text{Ba}(\text{Zr}_{0.05}\text{Ti}_{0.95})\text{O}_3$ with 1.5 wt% Li_2O were analyzed. Without Li_2O , the powder was around 50-60 μm in diameter (figure 4.20). With the additive, the primary particles agglomerated and formed two main sizes of around 0.5 μm and around 40 μm (figure 4.21) caused by the inhomogeneous mixing of the additive.

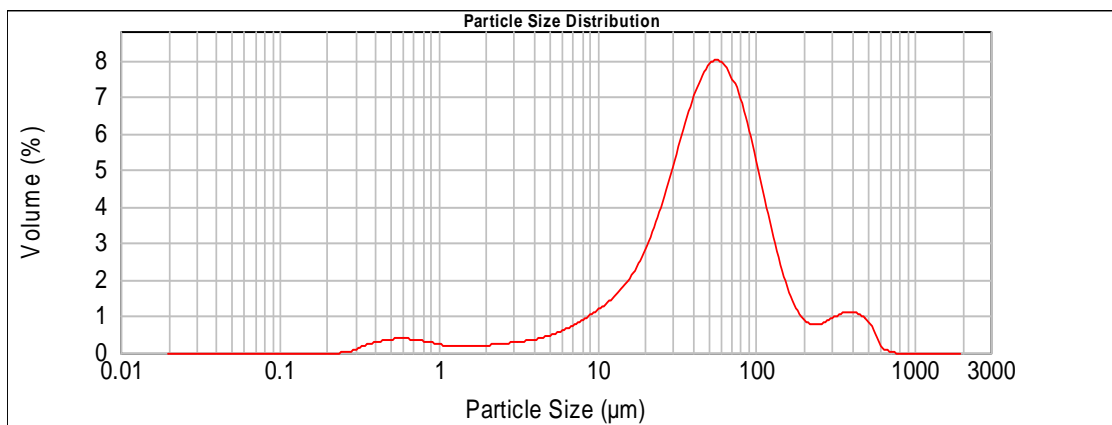


Figure 4.20 Particle size distribution of the calcined $\text{Ba}(\text{Zr}_{0.05}\text{Ti}_{0.95})\text{O}_3$ powder.

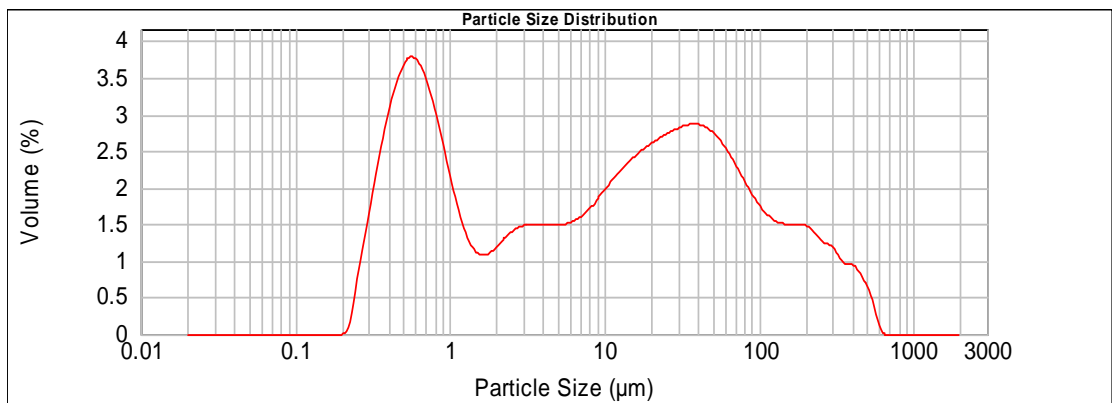


Figure 4.21 Particle size distribution of the calcined $\text{Ba}(\text{Zr}_{0.05}\text{Ti}_{0.95})\text{O}_3$ with 1.5 wt% Li_2O powder.

4.6 Conclusions

The BZT powder could be prepared using sol-gel process. A major disadvantage of this method is probably due to only small quantities of powders are obtainable from large quantities of the solution. In this chapter the crystal structure for the $\text{Ba}(\text{Zr}_x\text{Ti}_{1-x})\text{O}_3$ powders were all identified as follows. The powder without Zr crystallized into tetragonal perovskite whereas the $\text{Ba}(\text{Zr}_{0.05}\text{Ti}_{0.95})\text{O}_3$ is orthorhombic. It is rhombohedral for both $\text{Ba}(\text{Zr}_{0.10}\text{Ti}_{0.90})\text{O}_3$ and $\text{Ba}(\text{Zr}_{0.15}\text{Ti}_{0.85})\text{O}_3$. Finally, $\text{Ba}(\text{Zr}_{0.20}\text{Ti}_{0.80})\text{O}_3$ is cubic. The phase analyses of all the samples could be additionally confirmed by the measurements of the piezoelectric coefficient which was described in detail in Chapter 5. The Li_2O additive was able to lower calcination temperature without the effect on the crystalline phases. The size of the primary particles was reduced, however there was the mixture of the secondary particles. The application of the BZT powders obtained in this chapter was further used for fabricating ceramic and thick film as respectively mentioned in chapters 5 and 6.

CHAPTER 5

UNDOPED BZT CERAMICS AND BZT CERAMICS SYNTHESIZED AT LOW-SINTERING TEMPERATURE

In general, ceramic materials have high sintering temperatures. This is a major disadvantage for promoting the BZT material close to industrial requirements, e.g., high energy density and low energy consumption, one of the methodologies used is the addition of sintering additive that permit the densification of the ceramics at low temperature. It is realized that BZT ceramics derived from sol-gel powders are homogeneous and purified than those produced by solid-state reaction. This chapter thus aims to present the fabrication and characterization of BZT ceramics without and with sintering additive using the powder produced by sol-gel process. The effects of lithium oxide additive on the material properties are thoroughly studied.

5.1 Introduction

Since environmental concerns, lead-free ceramics such as KNN, NBT, and BZT (Shrout and Zhang, 2007) have been a growing interest in applications such as actuators and sensors. Among them, barium zirconate titanate ($\text{Ba}(\text{Zr}_x\text{Ti}_{1-x})\text{O}_3$, BZT) has become most attractive because it has been reported that the zirconium substitutions into the titanium lattices enhance the dielectric and piezoelectric properties (Yu *et al.*, 2002). The BZT-based materials, therefore, have high potential for usage as active elements in micro-fabricated devices (Stojanovic *et al.*, 2002 and Stojanovic *et al.*, 2004).

5.2 Review of previous work

Sol-gel technique can be used for several purposes including the formation of homogeneous thin films and powders as described in this analysis in chapters 3 and 4. The formation of thick film based on sol-gel derived powder will be discussed in chapter 6. There have been reported on BZT prepared by various routes or preparation conditions as described below.

Tang, Chew and Chan (2004) produced BZT ferroelectric ceramic ($\text{Ba}(\text{Zr}_x\text{Ti}_{1-x})\text{O}_3$, $x = 0.2, 0.25, 0.30$ and 0.35) by sol-gel process. Barium acetate, zirconium-n-propoxide and titanium n-butoxide were used as starting materials. Acetic acid and 2-methoxyethanol were the solvents. The dried gels obtained from this method were annealed at $1,100\text{ }^\circ\text{C}$ for 5 h, and then sintered at $1,400\text{ }^\circ\text{C}$ for 5 h. The silver paste was used as electrodes for electric characterization. The maximum dielectric constant at 1 MHz was 12250. It appeared that the Curie point shifted to lower temperature as Zr content increased. The ferroelectric phase transition occurred at $\text{Ba}(\text{Zr}_{0.20}\text{Ti}_{0.80})\text{O}_3$ - $\text{Ba}(\text{Zr}_{0.25}\text{Ti}_{0.75})\text{O}_3$ compositions.

Yu *et al.*, (2002) used solid-state reaction to prepare BZT ceramics of various Zr/Ti ratios, e.g. $\text{Ba}(\text{Zr}_x\text{Ti}_{1-x})\text{O}_3$ with $x = 0, 0.03, 0.08, 0.15, 0.20, 0.25$, and 0.30 . The most interesting composition was $\text{Ba}(\text{Zr}_{0.05}\text{Ti}_{0.95})\text{O}_3$ due to its high value of electromechanical coupling (0.565) and piezoelectric coefficient (236 pC/N). The high strain levels of $\sim 0.18\%$ at 40 kV/cm and of $\sim 0.25\%$ at ~ 120 kV/cm were reported for $0.03 < x < 0.08$.

Moura *et al.*, (2008) also fabricated $\text{Ba}(\text{Zr}_x\text{Ti}_{1-x})\text{O}_3$ ($x = 0.05, 0.10$, and 0.15) via solid-state reaction. Single phase BZT powders were obtained from calcination at $1,200\text{ }^\circ\text{C}$ for 2 h. and sintering at $1,550\text{ }^\circ\text{C}$ for 4 h. Raman spectroscopic analysis of the BZT indicated that there was a change in the crystal structure from orthorhombic to rhombohedral with increasing Zr content up to 10 mol%. Corresponding to this phase transition, the decrease in permittivity and remnant polarization was observed.

Fu *et al.*, (2009) focused on the microstructure and dielectric property of $\text{Ba}(\text{Zr}_{0.2}\text{Ti}_{0.8})\text{O}_3$ obtained from solid-state reaction. At this composition the BZT was reported to be tetragonal, very close to cubic phase. An average grain size was about 45 μm and the dielectric constant was about 7500.

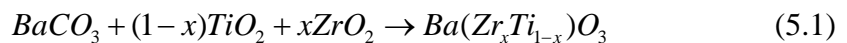
Regarding the reports on using sintering additive, they have been addressed in the following topic. In this work, the study of BZT prepared by sol-gel route with a change of Zr content (x) across the BaTiO_3 - BaZrO_3 phase diagram (Qi *et al.*, 2006) from $x = 0.0, 0.05, 0.10, 0.15,$ and 0.20 are carried out. All the BZT crystal structure will be completely identified and discussed in correlation to the material properties which is considered for adding sintering additive.

5.3 Sintering process

Sintering is the term used to describe the process of consolidation. The pores in a granular material will be eliminated by atomic diffusion driven by capillary forces. The sintering is often accompanied by shrinkage and densification. There have been proposed the methods to control the quality of the sintered products as described below.

5.3.1 Normal sintering

In the preparation of ceramics based on solid-state reaction, the mixed oxides undergo the cycles of mixing and heat treatment to achieve complete phase formation. There are two mechanisms involved: first, neck formation (by surface diffusion) and then, shrinkage (by grain boundary diffusion). This method is prepared by the following the chemical reaction (Ciomaga *et al.*, 2006)



Ciomaga *et al.*, 2006 used the reaction above to prepare the BZT from the BaCO_3 , ZrO_2 and TiO_2 starting materials. The average grain size of the BZT

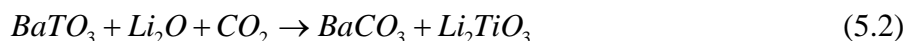
sintered at 1,350 °C is 0.75 μm and it became to 2.6 μm as sintering temperature increased to 1,450 °C.

5.3.2 Sintering additives

One of the main challenges in developing lead-free piezoelectric ceramics is to obtain composition that can form the desired structure at low temperatures and still remain good properties. In addition, the ceramics can be co-fired them with less expensive conductors, leading to a reduction of the energy consumption without using expensive electrode materials such as platinum or palladium.

Sintering additive is a particle which can be soluble or diffused into the ceramics in order to reduce grain boundary mobility. Sintering additive may also result in liquid-phase formation, then a reaction with the ceramic and, followed by the enhancement of elementary sintering mechanisms. Various sintering additives such as, B₂O₃, LiF and Li₂O were reported to have been used in BT and BST system, however, the report on the additive for BZT system still lack (Valant and Suvorov, 2004; Valant *et al.*, 2006; Hsi *et al.*, 2008 and Chou *et al.*, 2008).

For BaTiO₃ system, Valant *et al.*, (2006) studied a basic mechanism of low-sintering temperature or reaction liquid-phase sintering. The reaction of sintering additive and a matrix was



This reaction occurred at temperatures lower than 750 °C and the BaCO₃ usually starts melting at 811 °C. By adding 0.4 wt% of Li₂O the sintering temperature was as low as 820 °C.

Hsi *et al.*, (2008) prepared BaTiO₃ ceramic and used calcium borosilicate glass (CBS) for accelerating the densification and used LiF for reducing sintering temperature. The dense ceramics was obtained at low temperature (less than

900 °C). The suitable proportion of the CBS was 2 wt% and 4 wt% of LiF led to the high dielectric constant (>1700 at 1 kHz) and low dielectric loss (~0.01).

In 2004, Valant and Suvorov (2004) prepared low-sintering temperature $\text{Ba}(\text{Sr}_{0.60}\text{Ti}_{0.40})\text{O}_3$ or BST by a solid-state method. A small amount of Li_2O (0.4 wt %) additive reduced the sintering temperature to 900 °C. The BST had an apparent density of 97 %. However, there were two secondary phases or intermediate formation occurred during sintering process, Li_2TiO_3 and Ba_2TiO_4 .

Chou *et al.*, 2008 prepared low-sintering temperature $\text{Ba}(\text{Zr}_{0.35}\text{Ti}_{0.65})\text{O}_3$ using B_2O_3 - Li_2O co-additive through the solid-state method. $\text{Ba}(\text{Zr}_{0.35}\text{Ti}_{0.65})\text{O}_3$ ceramics was normally sintered at 1,500 °C for 5 h. The $\text{Ba}(\text{Zr}_{0.35}\text{Ti}_{0.65})\text{O}_3 + 4 \text{ wt}\% \text{Li}_2\text{O}$ was sintering at 1,000 °C for 4 h. The $\text{Ba}(\text{Zr}_{0.35}\text{Ti}_{0.65})\text{O}_3 + 4 \text{ wt}\% \text{Li}_2\text{O} + 0.75 \text{ wt}\% \text{B}_2\text{O}_3$ was found to sinter at 1,000 °C for 4 h. The co-doped ceramics increased in dense microstructure of BZT ceramics obtained by means of liquid-phase sintering.

5.3.3 Two-step sintering

This method is normally used for preparing nanocrystalline ceramics and achieving the complete densification of ceramic bodies without grain growth. The first step, the ceramic was fired at a higher temperature (T_1) to succeed an intermediate density, then cooled down and hold at lower temperature (T_2) until it was completely dense (Wang and Chen, 2006). Wang *et al.*, (2008) studied BaTiO_3 ceramic via modified oxalate precipitation method and two-step sintering method. The ceramic grain size ranging from 8 to 500 nm was obtained from the heat profile of T_1 at 1,220 °C for 5 min and T_2 at 1,150 °C for 2 h. The ceramics showed high dielectric constant of 9000 and low dielectric loss.

5.4 Materials and methods

5.4.1 Preparation procedure of the $Ba(Zr_xTi_{1-x})O_3$ ceramics

The gels received from the BZT solution prepared as described in figure 3.1, chapter 3. Firstly, the gels were kept in an oven until dried and calcined at different temperatures. Then a small amount of the calcined powders (1,100 °C for 2 h) was pressed into a pellet with a diameter (d) of 13 mm, finally the green body was sintered at 1,250 °C as shown in figure 5.1.

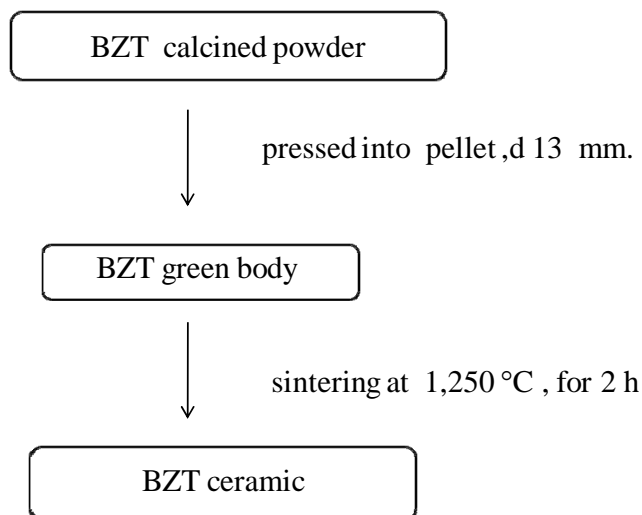


Figure 5.1 Preparation procedure of the BZT ceramic.

5.4.2 Process with the sintering additive

In order to lower sintering temperature, the composition of best piezoelectric properties, $\text{Ba}(\text{Zr}_{0.05}\text{Ti}_{0.95})\text{O}_3$ calcined powder was modified with sintering additive. The dried gel was added 1.5 wt% of lithium oxide powder (Li_2O , Aldrich, 97% purity) and homogeneously mixed before being calcined at 700 °C for 10 h. The BZT ceramic disks were then sintered at 900 °C for 4 h as shown in figure 5.2.

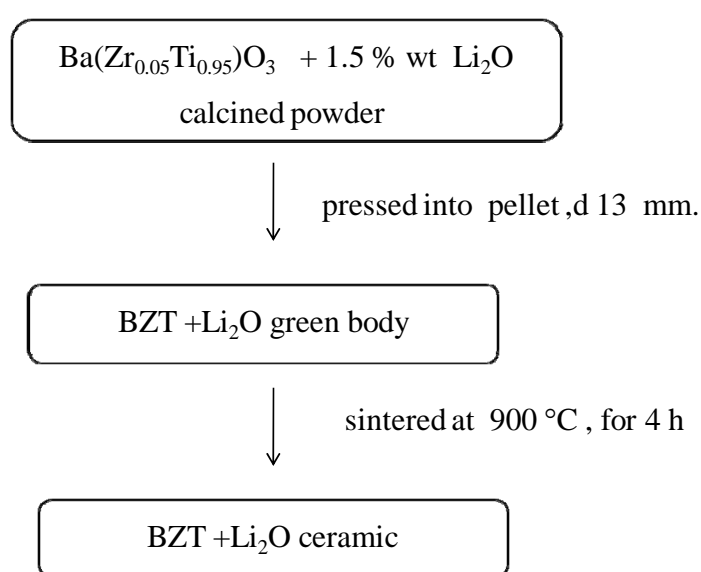


Figure 5.2 Preparation procedure of the $\text{Ba}(\text{Zr}_{0.05}\text{Ti}_{0.95})\text{O}_3$ with 1.5 % wt Li_2O ceramic.

5.4.3 *Microscopic characterization*

The surface morphology of sintered ceramics was featured using JEOL JSM-5800 LV (JEOL Apparatus).

5.4.4 *Densification analysis*

The densifications of ceramic were identified by Archimedes' method (ASTM, 1977). First, the sample was measured its dried weight (W_d), and then immersed in the water for 24 h. After that it was weighted in the air (W_a). A final weight (W_{aw}) was obtained by immersing the sample in the water for 24 h before weighting the immersing sample. All the weights were measured in grams. The density (ρ_b) in units of g/cm^3 for each sample can be calculated from:

$$\rho_b = \frac{W_d \rho_w}{W_a - W_{aw}} \quad (5.3)$$

Where ρ_w is the density of water (in g/cm^3).

5.4.5 *Dielectric and piezoelectric properties characterization*

The silver paste was used as electrodes. The electroded samples were heated at 600 °C for 10 min with heating rate 15 °C/min. Subsequently, they were found to be effectively poled at 3 kV/mm for 30 min in a silicone oil bath.

The LCR meter (Hewlett Packard 4263B) was employed to observe the dielectric properties. A resonance method was used to determine the transverse piezoelectric coefficient.

The piezoelectric strain coefficient for the ceramic sample was determined by the Piezo d_{33} tester (APC Part number: 90-2030) (Berlincourt Piezo d_{33} meter manual, 1974).

5.5 Results and discussion

The gels results were already analyzed and reported in chapter 3. The following is data on material properties which have yet not been mentioned.

5.5.1 *Microstructure of the $Ba(Zr_xTi_{1-x})O_3$ ceramics*

The SEM images of the BZT ceramics with various compositions are shown in figures 5.3-5.7. They are highly dense, only small amounts pores were observed. The grain sizes were decreased with increased Zr contents. Their density and grain sizes were listed in table 5.1.

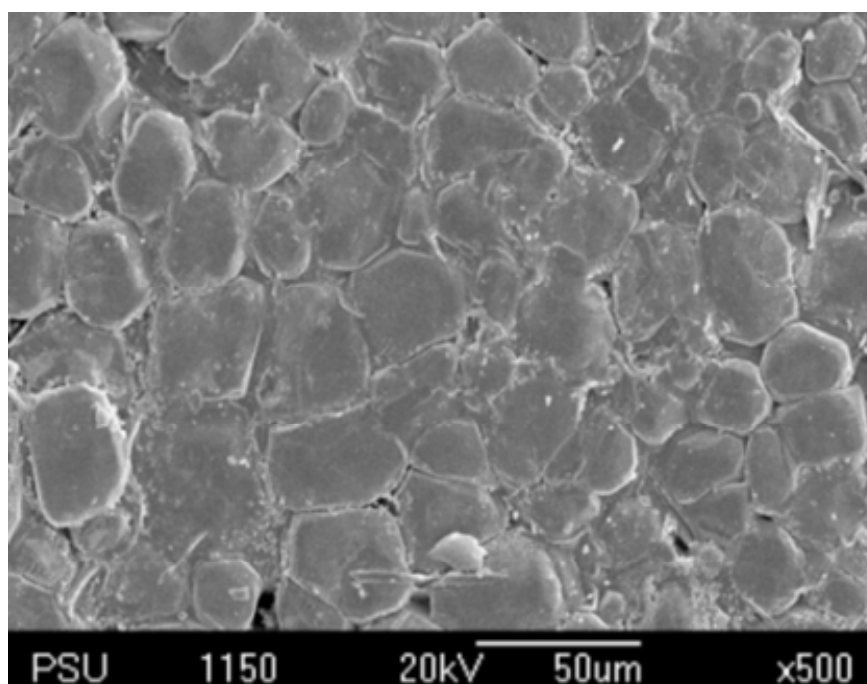


Figure 5.3 SEM image of the BaTiO₃ ceramic.

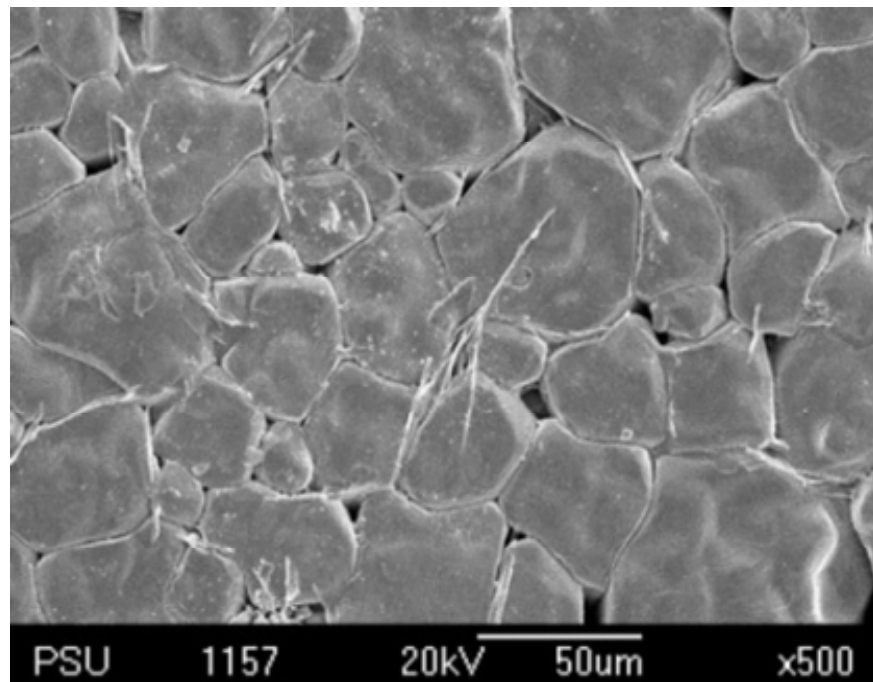


Figure 5.4 SEM image of the $\text{Ba}(\text{Zr}_{0.05}\text{Ti}_{0.95})\text{O}_3$ ceramic.

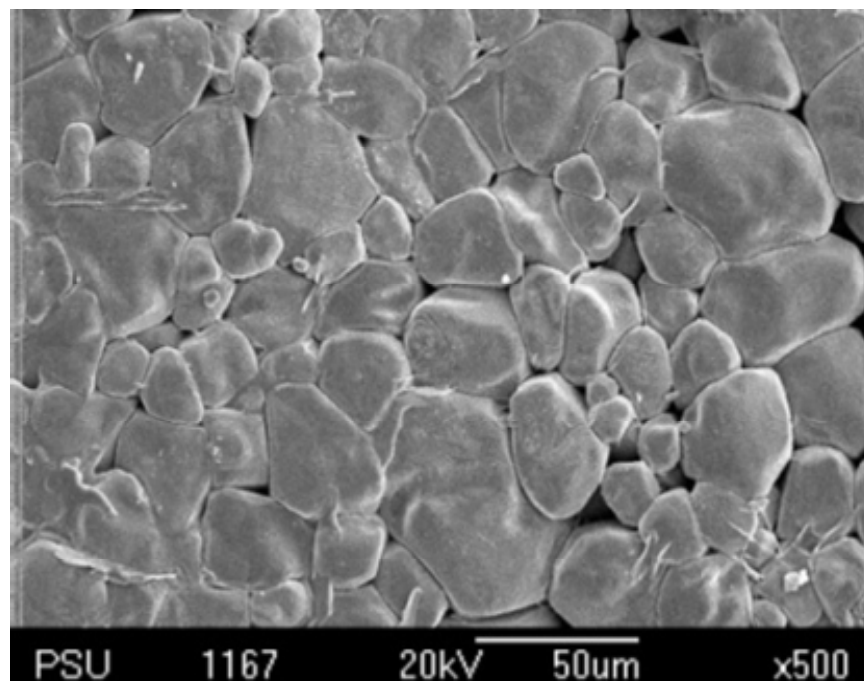


Figure 5.5 SEM image of the $\text{Ba}(\text{Zr}_{0.10}\text{Ti}_{0.90})\text{O}_3$ ceramic.

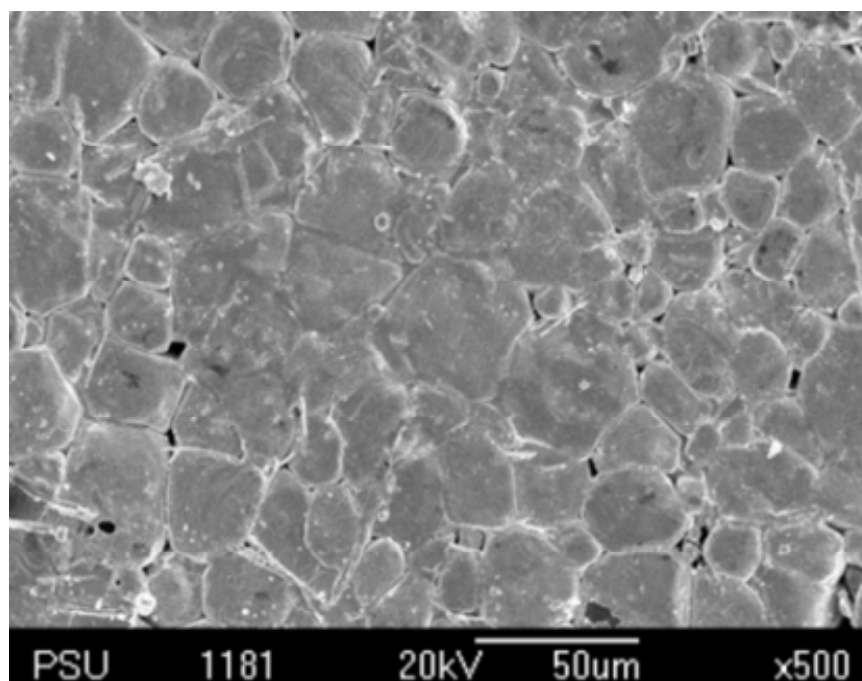


Figure 5.6 SEM image of the Ba(Zr_{0.15}Ti_{0.85})O₃ ceramic.

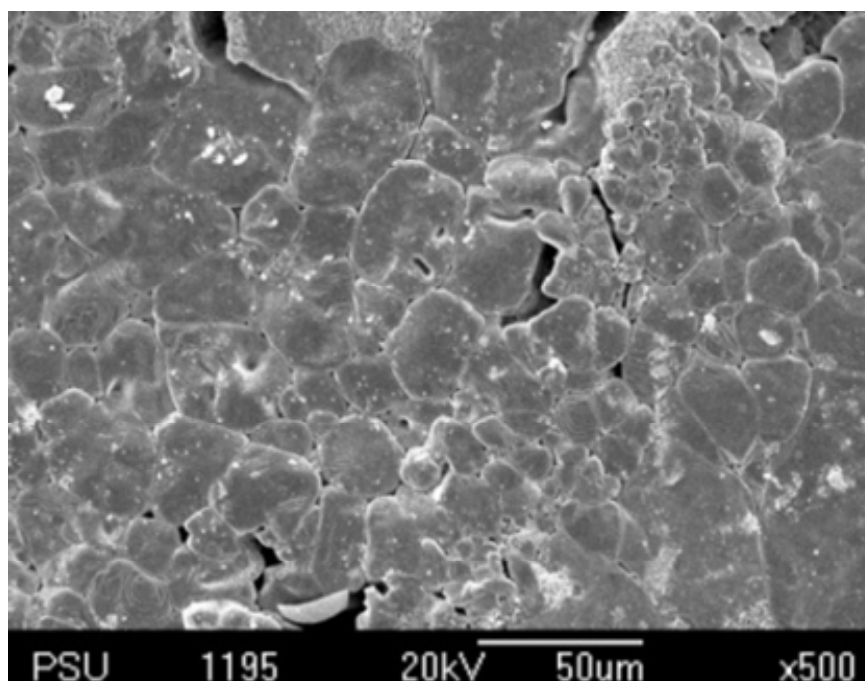


Figure 5.7 SEM image of the Ba(Zr_{0.20}Ti_{0.80})O₃ ceramic.

Table 5.1 Density and grain size of the Ba(Zr_xTi_{1-x})O₃ ceramics.

Ba(Zr _x Ti _{1-x})O ₃ ceramics	Density (ρ) (g/cm ³)	Grain size (μ m)
x = 0.00	5.04	39.60 \pm 3.5
x = 0.05	5.06	27.54 \pm 2.8
x = 0.10	5.09	21.63 \pm 4.2
x = 0.15	5.38	20.19 \pm 3.2
x = 0.20	5.41	15.94 \pm 4.5

5.5.2 Dielectric properties of the Ba(Zr_xTi_{1-x})O₃ ceramics

The dielectric constant and dielectric loss for all the samples measured at 1 kHz and at room temperature were summarized in table 5.2. The temperature dependence of dielectric constant was plotted in figure 5.8.

Table 5.2 Summary of the room-temperature dielectric properties measured at 1 kHz of the Ba(Zr_xTi_{1-x})O₃ ceramics.

Ba(Zr _x Ti _{1-x})O ₃ ceramics	Dielectric constant	Dielectric loss
x = 0.00	1302	0.04
x = 0.05	1361	0.04
x = 0.10	1957	0.05
x = 0.15	3704	0.06
x = 0.20	5118	0.07

At room temperature, the dielectric constant and the dielectric loss increased with Zr content. The increase in dielectric constant relating to the shift in Curie temperature (T_c) was shown in figure 5.8. The Zr substitution in BaTiO_3 ceramic affected the transition temperatures. When $0.0 < x < 0.2$, the transition temperatures were considerably above room temperature and became closer when the unit cell changed towards the cubic structure. This is due to the O-Ti-O bond is weaker than the O-Zr-O bond (Kuang *et al.*, 2009). Moreover, the $\text{Ba}(\text{Zr}_{0.20}\text{Ti}_{0.80})\text{O}_3$ ceramic displayed the broad curve of the dielectric constant measured near the T_c . This is because of the inhomogeneous distribution of Zr ions in the crystal lattice and the mechanical stress existed in the grains (Tang *et al.*, 2004). For $\text{Ba}(\text{Zr}_{0.05}\text{Ti}_{0.95})\text{O}_3$ ceramic, a change in the dielectric constant near 55°C was clearly noticeable. This was the tetragonal- to-orthorhombic transition (T_1) only appeared in this crystalline phase (Kuang *et al.*, 2009)

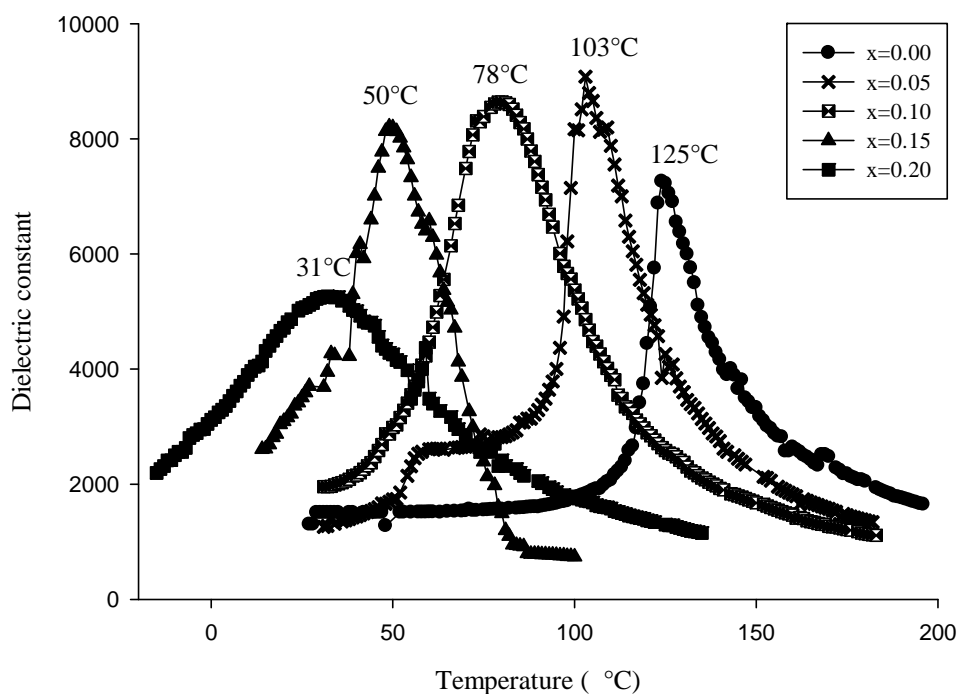


Figure 5.8 Variations of the dielectric constant with temperature of $\text{Ba}(\text{Zr}_x\text{Ti}_{1-x})\text{O}_3$ ceramics.

The electromechanical properties for all the BZT ceramics were summarized in table 5.3. The Ba(Zr_{0.05}Ti_{0.95})O₃ exhibited the highest piezoelectric response and good electromechanical coupling. It is known that the higher the number of polarizable directions aligned to a poling field, the larger the piezoelectric coefficient is (Moura *et al.*, 2008; Dixit *et al.*, 2003). Possible polar directions in the tetragonal, orthorhombic, and rhombohedral structures are six, twelve, and eight, respectively (ANSI/IEEE Std 180-1986). This is corresponded to the crystalline phases identified earlier by this work that the Ba(Zr_{0.05}Ti_{0.95})O₃ is orthorhombic while the Ba(Zr_{0.10}Ti_{0.90})O₃ and Ba(Zr_{0.15}Ti_{0.85})O₃ are rhombohedral.

Table 5.3 Summary of the electromechanical properties of the Ba(Zr_xTi_{1-x})O₃ ceramics

Ba(Zr _x Ti _{1-x})O ₃ ceramics	f_r (kHz)	f_a (kHz)	K_p (%)	$-d_{31}$ (pC/N)	d_{33} (pC/N)
x = 0.00	236	240	46	25.65	101 ± 5.0
x = 0.05	263	268	48	26.82	126 ± 5.0
x = 0.10	264	268	46	24.56	83 ± 5.0
x = 0.15	202	204	44	19.27	36 ± 5.0
x = 0.20	-	-	-	-	-

5.5.3 Effect of the sintering additive

Ba(Zr_{0.05}Ti_{0.95})O₃ ceramic was the subject of the study due to the highest electromechanically properties. The microstructures of Ba(Zr_{0.05}Ti_{0.95})O₃ ceramics without sintering additive was shown in figures 5.9. The grains are cubic in shape. A change in shape was clearly observed when adding the Li₂O. A significantly reduction in grain size was shown in figure 5.10. This was because the reaction of a liquid-phase during sintering process and thus accelerated the sintering mechanism (Valant *et al.*, 2004; Chou *et al.*, 2008). The density and grain sizes were listed in table 5.4. The values of the dielectric constant were listed in table 5.5.

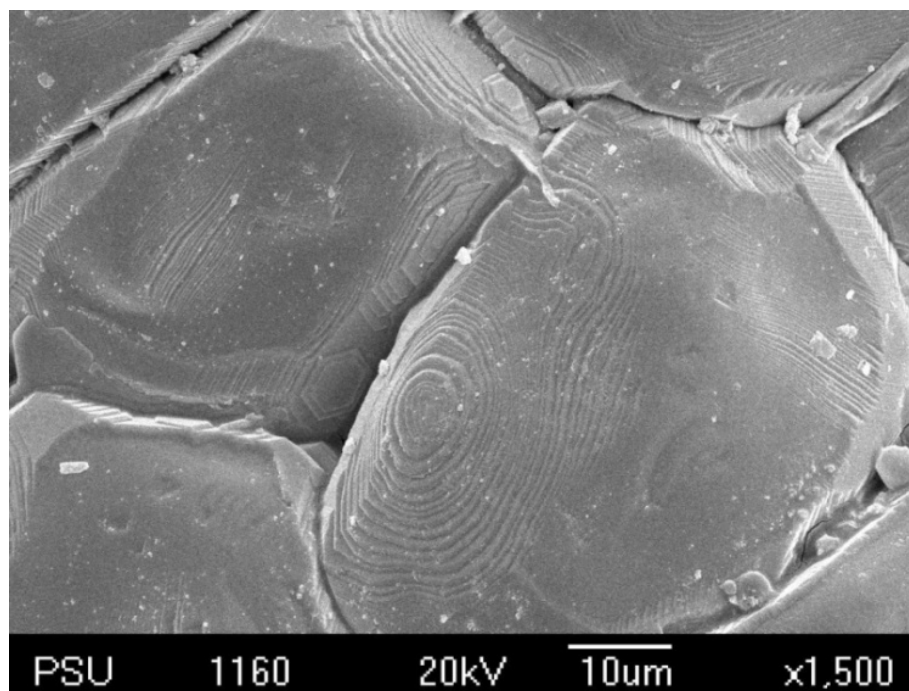


Figure 5.9 SEM image of the Ba(Zr_{0.05}Ti_{0.95})O₃ ceramic.

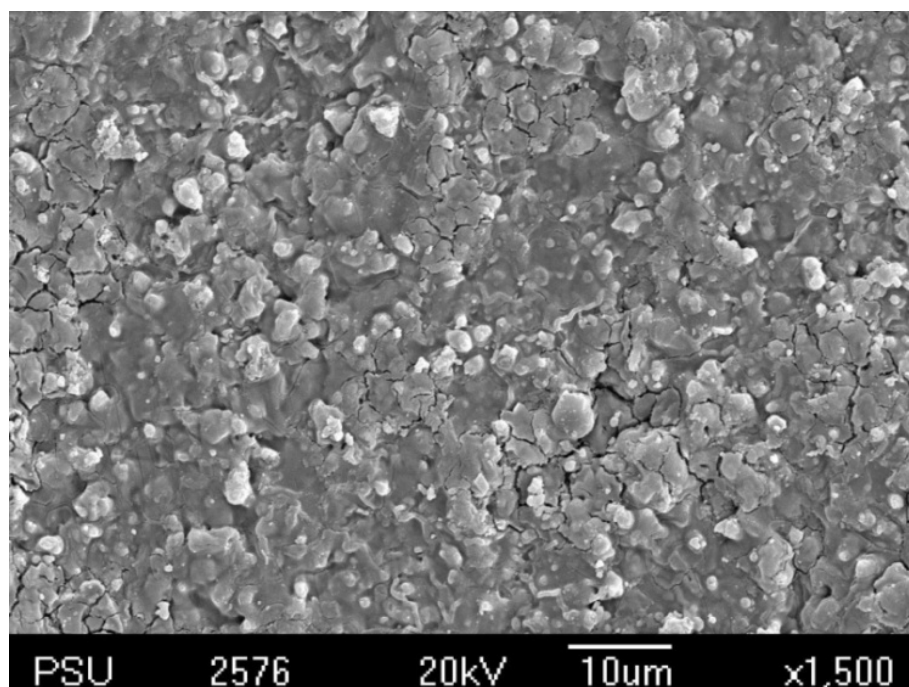


Figure 5.10 SEM image of the Ba(Zr_{0.05}Ti_{0.95})O₃ with 1.5 wt% Li₂O ceramic.

Table 5.4 Density and grain size of the $\text{Ba}(\text{Zr}_{0.05}\text{Ti}_{0.95})\text{O}_3$ ceramics, without and with the sintering additive.

BZT ceramics	Density (ρ) (g/cm^3)	Grain size (μm)
$\text{Ba}(\text{Zr}_{0.05}\text{Ti}_{0.95})\text{O}_3$	5.06	27.54 ± 2.8
$\text{Ba}(\text{Zr}_{0.05}\text{Ti}_{0.95})\text{O}_3$ with 1.5 wt% Li_2O	5.59	4.00 ± 1.2

Table 5.5 Room-temperature dielectric properties of the $\text{Ba}(\text{Zr}_{0.05}\text{Ti}_{0.95})\text{O}_3$ ceramics, without and with the sintering additive.

BZT ceramics	dielectric constant (1 kHz)	Dielectric loss (1 kHz)
$\text{Ba}(\text{Zr}_{0.05}\text{Ti}_{0.95})\text{O}_3$	1361	0.041
$\text{Ba}(\text{Zr}_{0.05}\text{Ti}_{0.95})\text{O}_3$ with 1.5 wt% Li_2O	1250	0.026

The density and grain sizes were listed in table 5.4. It can be noticed that the diffusions of Li^+ ions greatly affected the grain growth of ceramic, and consequently, reduced the grain size. Clearly, the phase transition was not significantly affected due to only the small amount of Li_2O was used (figure 5.11).

In table 5.5, the values of the dielectric constant of both samples were close to each other while the loss tangent was reduced after adding sintering additive. This was because of a large reduction in grain size in Li-doped sample which was followed by the higher concentration of grain boundaries (Moulson and Herbert, 1990). This also led to a broader and lower dielectric constant as a function of temperature as shown in figure 5.11. However, these values are still relatively high when compared to conventional ceramics.

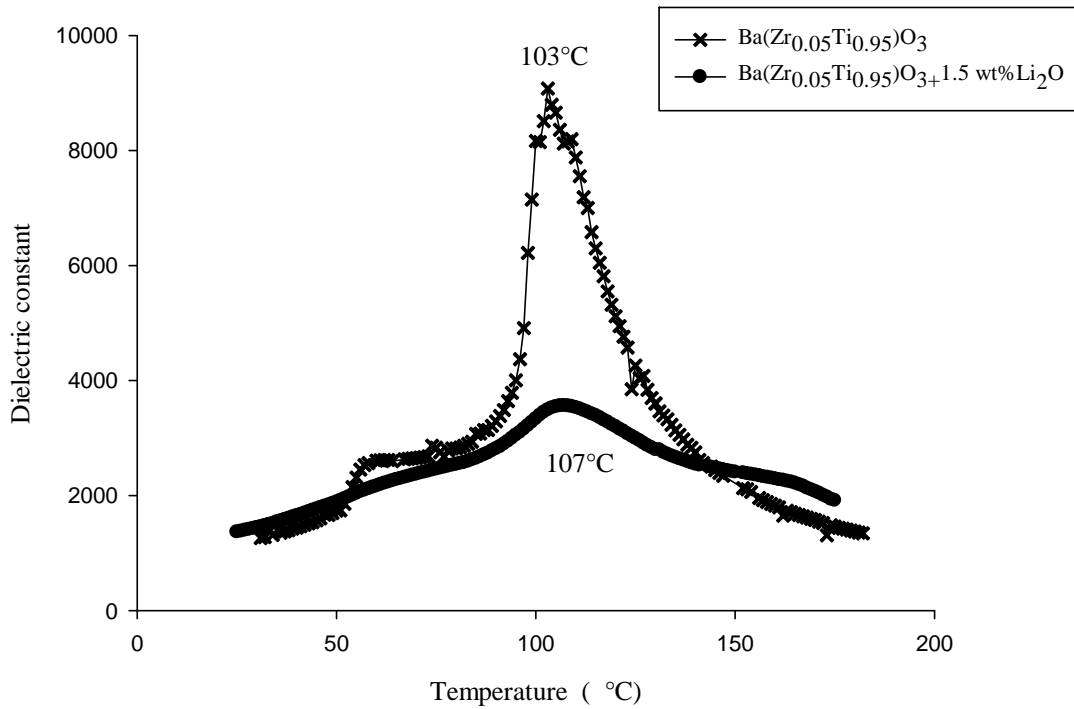


Figure 5.11 Variations of the dielectric constant with temperature for $\text{Ba}(\text{Zr}_{0.05}\text{Ti}_{0.95})\text{O}_3$ without and with 1.5 wt% Li_2O .

Table 5.6 Electromechanical properties of the $\text{Ba}(\text{Zr}_{0.05}\text{Ti}_{0.95})\text{O}_3$ ceramics, without and with the sintering additive.

BZT ceramics	f_r (kHz)	f_a (kHz)	k_p (%)	$-d_{31}$ (pC/N)	d_{33} (pC/N)
$\text{Ba}(\text{Zr}_{0.05}\text{Ti}_{0.95})\text{O}_3$	263	268	48	26.82	126 ± 5.0
$\text{Ba}(\text{Zr}_{0.05}\text{Ti}_{0.95})\text{O}_3$ with 1.5 wt% Li_2O	280	283	44	22.25	120 ± 5.0

The electromechanical properties of the $\text{Ba}(\text{Zr}_{0.05}\text{Ti}_{0.95})\text{O}_3$ was unchanged after adding the Li_2O as seen in table 5.6. The net polarization in BZT samples was not affected by the sintering additive which was not piezoelectric.

5.6 Conclusions

Barium zirconate titanate of different Zr contents was studied their physical and electromechanical properties and the use of lithium oxide as sintering additive was evaluated. The composition of best piezoelectric properties obtained from $\text{Ba}(\text{Zr}_{0.05}\text{Ti}_{0.95})\text{O}_3$ ceramics. With the additive, the densification of the BZT took place at 900 °C which is lower than the melting points of the conventional conductive materials like silver and gold (melting points 960° C and 1,063 °C, respectively). The Li_2O additive which is not piezoelectric affected only on the physical properties in the low-sintering-temperature BZT without influencing their good electromechanical properties. The mechanically activated powders of this material are attractive for, e.g., making paste materials used in conventional screen-printing techniques which was addressed and discussed in chapter 6.

CHAPTER 6

FREE-STANDING BARIUM ZIRCONATE TITANATE THICK FILM

Piezoelectric BZT thin films have been previously presented in chapter 3. The BZT films with thicknesses larger than nanometer range can actually be fabricated and incorporated into different kinds of devices. For instance, the films with thicknesses of 0.1-1 μm are normally used in IR sensors while those with typical thickness of 10-50 μm are needed in actuators. However, there have been a few reports regarding the fabrication and properties of BZT-based thick films in spite of their possible applications in capacitors and tunable microwave devices (Stojanovic *et al.*, 2004; Tick *et al.*, 2008). Chapter 6 aims to present the background of thick film technology, focusing on free-standing thick films with sacrificial layer procedure. Subsequently, the mentioned technology is applied to produce free-standing BZT thick film.

6.1 Introduction

The miniaturization of piezo-actuators and sensors is often difficult due to the lack of piezoelectric films of several micron thicknesses. Thick film technology has thus been introduced in order to effectively fill the technology gap between thin film and bulk. Thick films of ferroelectric materials are desired for fabricating MEMS which are required to withstand high operating voltages and generate a large driving force of energy with the properties close to the bulk. (Tadigadapa1 and Mateti, 2009; Kim *et al.*, 2005). Conventional dipping and spin-coating procedure do not allow achieving thickness of more than several microns. Thick film technologies are thus often required at industrial level.

Among the thick film technologies, the screen-printing method was chosen for producing BZT thick films with free-standing structure (Lucat *et al.*, 2007; Ginet, 2007; Lucat *et al.*, 2008; Castille *et al.*, 2009; Castille., 2010).

None of the free-standing BZT thick film has been previously reported. Therefore, the report in this work increases the possibility of using BZT elements in MEMS and other related technologies.

6.2 Free-standing thick films and concepts of a cantilever

It has been a few years since the free-standing thick films have been developed in the IMS laboratory of Bordeaux1 University, Bordeaux, France (Lucat *et al.*, 2007; Ginet, 2007; Lucat *et al.*, 2008; Castille *et al.*, 2009; Castille, 2010). This technology can achieve piezoelectric components released from the substrate through the combination of standard screen printing method and sacrificial layer. As can be seen from figure 6.1 the sacrificial layer acts as a mechanical support for the up-coming active layer. A removal of the sacrificial layer would leave behind a cavity between the active layer and the substrate, leading to the so-called free-standing or free-moving structure.

Choices of substrate, electrode materials and sacrificial layer all play an important role in the technology. Strontium carbonate (SrCO_3) was chosen as sacrificial layer because its chemistry and decomposition temperature are compatible with the overall procedure and temperature profile. The strontium carbonate can be removed after the final heat treatment by emerging the fabricated structure in a phosphoric acid of mild concentration. Common metals such as gold and silver are often used as electrodes because their melting temperature is lower than the firing temperature used in the procedure. Some additives or eutectic materials such as borosilicate glass frits are often used in order to lower the firing of the fabricated structure down to a temperature less than 1,000 °C without fracture and phase change. In the screen-printing process, the MEMS patterns will be placed on a variety of substrate materials. Alumina substrate is frequently used due to its high chemical and thermal stability and low corrosion. In general, the MEMS devices can be fabricated into three different structures, i.e, plates, diaphragms and cantilever. The most popular structure is the last one. The vibration configuration of a cantilever has two main modes, the vertical transversal vibration (figure 6.2 (a)) and the horizontal

longitudinal vibration (figure 6.2 (b)). The latter is of interest in this work because the piezoelement is moving more freely than the first.

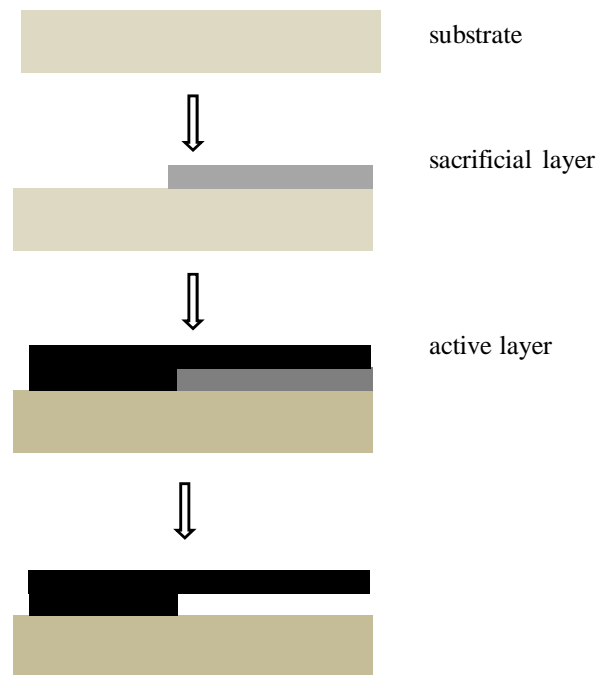


Figure 6.1 Thick film procedure with sacrificial layer deposited onto a substrate at the beginning step and removed afterwards at a final step (Lucat *et al.*, 2007; Ginet, 2007).

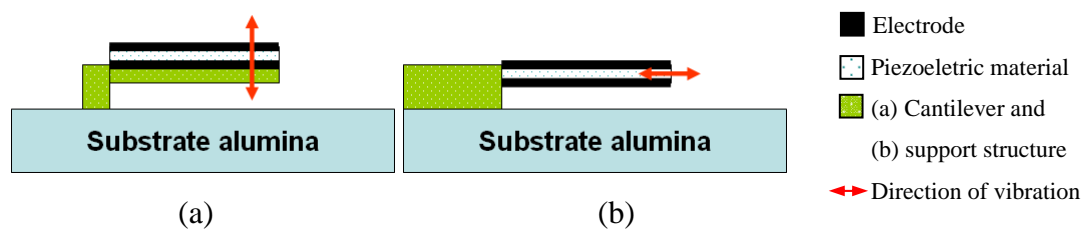


Figure 6.2 Transversal vibration (a) and longitudinal vibration (b) (Castille, 2010).

The frequency (f) of free standing structure as shown in figure 6.2 (b), according to ANSI/IEEE Std 176-1987 the longitudinal vibration, the propagation velocity wave along the structure of length (L), width (b) and thickness (h) is given as (ANSI/IEEE Std 176-1987).

$$v_{31} = \frac{1}{\sqrt{\rho_{beam} s_{11}^E}} \quad (6.1)$$

$$f_{31}^{(n)} = \frac{\lambda_{31}^n}{2\pi} \sqrt{\frac{k}{m}} \quad (6.2)$$

where
$$k = \frac{Ebh}{L} \quad (6.3)$$

Then the frequency can be obtained by placing (6.3) into (6.2) to yield (6.4)

$$f_{31}^{(n)} = \frac{\lambda_{31}^n}{2\pi L} \sqrt{\frac{E_i}{\rho_i}} \quad \text{or} \quad f_{31}^{(n)} = \frac{\lambda_{31}^n}{2\pi L} \sqrt{\frac{1}{\rho_i s_{11}^E}} \quad (6.4)$$

The Eigen values of $\lambda_{31}^{(n)}$ are defined corresponding to the longitudinal vibration given by (ANSI/IEEE Std 176-1987)

$$\lambda_{31}^{(n)} = \frac{2n-1}{2} \pi, \quad n = 1, 2, \dots \quad (6.5)$$

6.3 Review of previous work

The previously works have been reported on the lead-based thick films deposited on different substrates by screen-printed process and was described in figure 6.3 (Yao and Zhu, 1998). Moreover, PZT thick films (cantilever types) of various dimensions were shown in figure 6.4 (Castille *et al.*, 2009; Castille, 2010).

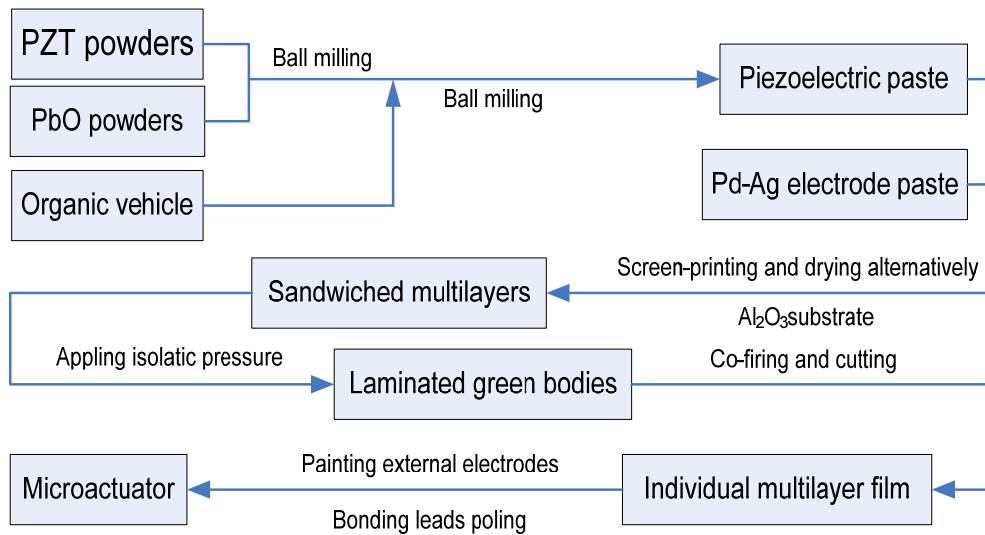


Figure 6.3 Flow chart of the preparation of PZT thick-film actuator (Yao and Zhu, 1998).

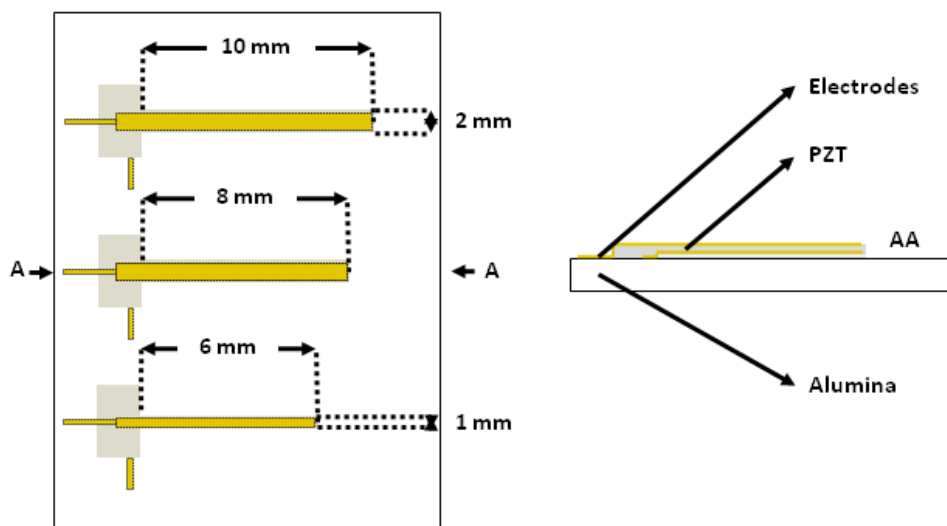


Figure 6.4 The PZT thick film geometry with various shapes (Castille *et al.*, 2009; Castille, 2010).

Zhang *et al.*, (2003) fabricated the PZT cantilever, the width of 100 μm and the length of 130-280 μm , for operating at its resonance in a frequency range of 6.1-29.6 kHz. The PZT-cantilever was actuated with an applied electric voltage of 100 V, with typical tip displacement of 30 μm .

Cotton *et al.*, (2007) fabricated the screen-printed PZT-Pz29 thick film using the paste without any binders. A maximum piezoelectric coefficient d_{33} of 168 pC/N was obtained. This value was 28 % more than those of other conventional piezoelectric thick films.

Stojanovic *et al.*, (2002) fabricated barium titanate ((BaTiO₃) thick films of three layers by using the screen-printing technique on alumina. A small amount of the LiF was used as a sintering additive. Thicknesses of the BT films ranging from 25-75 nm were obtained by sintering at 850° C for 1 h. The relative permittivity or dielectric constant for all the films were 500-2600 and the Curie temperature was ~120 °C. These values are similar to those of the bulk.

Zimmeermanm *et al.*, (2004) prepared BST (BaSr_{0.6}Ti_{0.4}O₃) and BZT (BaZr_{0.3}Ti_{0.7}O₃) thick films with an average grain diameter of 30 nm. The materials for making the pastes were prepared by solid-state reaction. After calcination of the powders at 1,100 and 1,250 °C for BST and BZT, respectively, the paste for each material was made. When each paste was mixed with the binder until a paste was established, the paste was screen-printed onto alumina and followed by firing at 1,200 °C and 1,080 °C for BST and BZT, respectively. For BZT, the maximum dielectric constant was 500 (at Curie temperature of -50 °C) while the room-temperature relative permittivity of the BST was 230 at 25° C.

Palukuru *et al.*, (2010) reported on the screen-printed barium strontium titanate (BST) thick films for integrating them into tunable microwave device. They used the BST powder doped with 0.8 wt% of Li₂O and pre-heated at 500 °C for 10 h. The paste was prepared by mixing 80 wt% of BST powder, 16 wt% of organic medium and 4 wt% of dispersant. Alumina was used as substrate. The films were sintered at 900 °C for 3 h.

Tick *et al.*, (2008) described the LiO₂-doped BST thick films prepared by double screen-printed method. The thickness obtained after sintering 60 μm. The films were fired with different sintering temperatures, 500, 700 and 900 °C (for the same period of 10 h). The highest density of 72 vol%, was received from the 500 °C film. In accordance of the sintering temperature mentioned earlier, the dielectric constants (1 MHz) were 700, 730 and 790 while the dielectric loss were extremely low, 0.0042, 0.0051 and 0.0055.

The neat BZT is usually at high temperature as high as 1,250 °C which leads to the elaborating of electrode is possible. To achieve the desired BZT structure that can be sintered at low temperatures and to be co-fired with inexpensive conductors like gold, possible additives for reducing sintering temperatures are used, for example, B₂O₃, LiF and Li₂O were reported their use in BT and BST system, however, the report on the additive for BZT system is rarity (Valant and Suvorov, 2004; Valant *et al.*, 2006; Hsi *et al.*, 2008 and Chou *et al.*, 2008).

The free-standing piezoelectric thick films which combine the standard screen-printed and the sacrificial layer of graphite or glass have been reported for making thick films and LTCC (low temperature co-fired ceramics). The sacrificial layer is normally eliminated at the end of the process to release the beam and allow it to move freely. Various applications benefit from this technology are, for example, electrothermal microactuators, microresistors, strain gauges, microchannels, and implementation of piezoelectric devices (Lucat *et al.*, 2008).

Lucat *et al.*, (2008) selected the strontium carbonate material as sacrificial layer due to mechanical and thermal stability, and solubility in acidic acid. Castille *et al.*, (2009) fabricated free standing PZT cantilever for gas sensor by a screen-printed and a sacrificial layer techniques. The piezoelectric paste was prepared by PZ26 powder. Lead borosilicate and ESL400 were the glass frit and organic vehicle, respectively and the pastes were screened on the alumina substrate. The best resonance behavior and quality factor was obtained from the cantilever with dimension of 8×2×0.08 mm³. By using the longitude vibration mode, the self-actuating cantilever could detect the toluene with a 44 μm PEUT (polyetheruretane) coating.

6.4 Materials and methods

6.4.1 *Preparation of the sacrificial layer paste*

The sacrificial paste was prepared by using the strontium carbonate or SrCO_3 (Carlo Erbe Reagent, purity: 99%) due to its decomposition temperature (1,100 °C) which is less than the standard temperature in screen-printing process (lower than 1,000 °C). Epoxy resin (ELS 400, Electro-Science Laboratories, Inc) was selected as the organic vehicle because it has more ability to be used on a flexible substrate. Among the polymers it can serve as a basis for a screen-printed paste, the epoxy resin seems to be the best compromise due to its good chemical compatibility with other materials, an application compatible with screen-printing and good temperature resistance. The starting powder was sieved at 38 μm . The powder was dried at 120 °C for 1 h to discard the humidity. The SrCO_3 dried powder (80 wt%) was mixed with epoxy resin in mortar for 20 min before being homogenized for 4 h by two turntables machine (Castille, 2010).

6.4.2 *Preparation of the BZT pastes*

Owing to the sintering temperature below 950 °C it is preferable, due to the melting point of gold electrode (1,063 °C), it is necessary to add different compounds to achieve liquid-phase sintering or assist sintering. The best electromechanically properties, $\text{Ba}(\text{Zr}_{0.05}\text{Ti}_{0.95})\text{O}_3$ (BZT) was employed as active powder as described in chapters 4 and 5 was used in this endeavor. Three groups of the BZT powders; namely A, B and C were desired. After that the ratio between BZT and resin were characterized before preparing thick films. The suitable ratio of preparing the pastes was described below.

Group A. BZT + 1.5 wt% Li₂O powder

The powder of the BZT + 1.5 wt% Li₂O derived from sol-gel method described earlier was selected as starting powder. Before weighting and mixing the powder, it was dried and kept for 1 h in an oven (120 °C) in order to remove the moisture. The powder was sieved in a 38 μm mesh. The powder and the organic vehicle were mixed using 75 wt% of powder and 25 wt% of vehicle. The powders were homogeneously milled for 20 min in a mortar agate before being homogenized for 4 h by two turntables machine.

Group B. BZT + 1.5 wt% Li₂O ceramic

The BZT with 1.5 wt% Li₂O calcined powder was also prepared from sol-gel method and was used for making the paste. This powder was pressed into disk and sintered at 900 °C for 4 h to obtain the BZT ceramic. The BZT disks were undergone the grinding process in methanol by planetary ball milling for 24 h. The ground powder was dried in an oven until the dried powder was obtained. Then the powder was fed to make the paste in a similar manner as Group A.

Group C. BZT ceramic + Li₂CO₃-Bi₂O₃-CuO powder

The BZT used here was also prepared from sol-gel method as previously described in chapter 4. This powder was pressed into disk and sintered at 1,250 °C for 2 h. The same grinding process for Group B was also used for this group. The common additive, Li₂CO₃-Bi₂O₃-CuO (40-10-50 wt %) for PZT element was applied to the BZT powder in order to reduce sintering temperature (Seveyrat and Gonnard, 2003). Next, the rest of the procedure was described for the first two groups.

6.4.3 The BZT thick film fabrication

The process for preparing thick film was shown in figure 6.5.

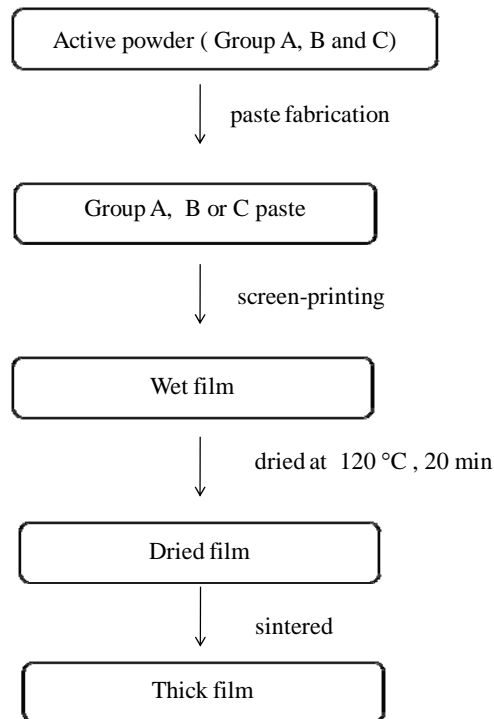


Figure 6.5 Flow chart of the thick film elaborating.

The preparation of cantilever-type structure was presented in figure 6.6 (Castille, 2010). First, the gold electrode (8838 A , Electro-Science Laboratories, Inc.) was screened on alumina substrate through a 325 screen mesh (figure 6.6 (a)) The next step was depositing the sacrificial layer by using a 70 mesh of screen, and dried this layer for 20 min at 120 °C. The thickness of the film obtained was 100 μm (figure 6.6 (b)). Then the bottom electrodes were screened (figure 6.6 (c)). The BZT layer was a screen 70 mesh to obtain a final thickness after dried film about 160 μm (figure 6.6 (d)). Finally, the top electrode was screened (figure 6.6 (e)). The films were dried in an oven at 120 °C for 20 min before sintering.

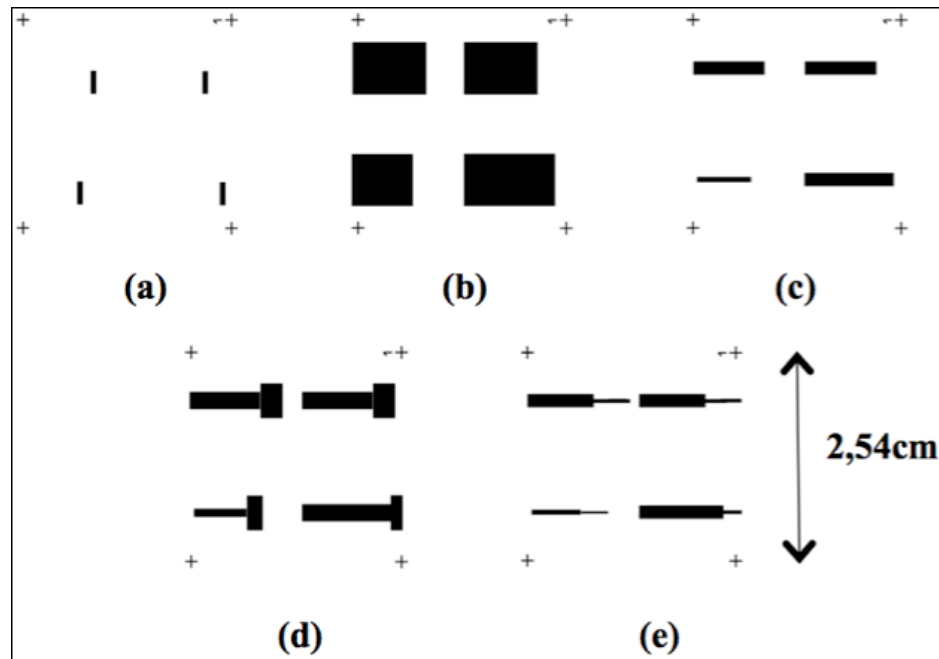


Figure 6.6 Patterned screen for (a) the tracks of gold (b) the layer sacrificial (c) the lower electrode (connected to conductive tracks), (d) the layer piezoelectric and (e) the top gold electrode (Castille, 2010).

6.4.4 Pressing the thick films

The procedure of pressing thick film in order to improve the compactness of the film was depicted in figure 6.7. All samples were packed in polyethylene (PE) bags sealed by heat. The PE films used to protect from high pressure (figure 6.8). Next, the sample was pressed at 100 MPa using the pressing machine (ICMCB (Institut de Chimie de la matière condensée de Bordeaux, Bordeaux 1 University, Bordeaux, France) as shown in figure 6.9.

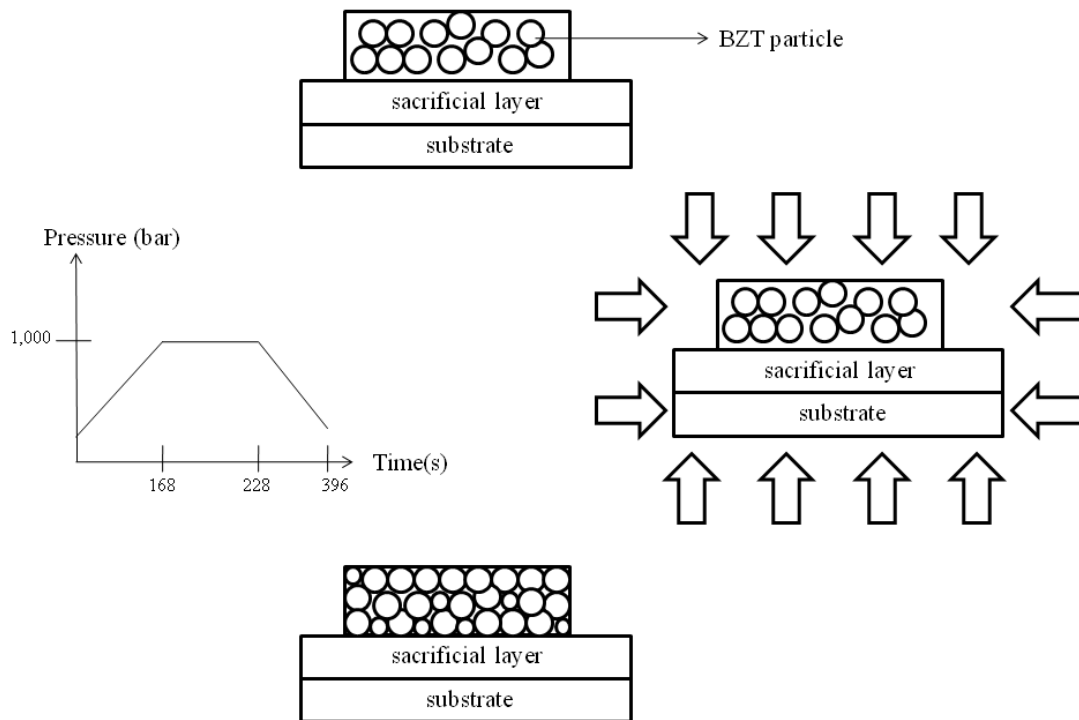


Figure 6.7 Procedure of pressing thick film.



Figure 6.8 Samples encapsulated in polymer film.



Figure 6.9 The pressing machine.

6.4.5 Removal of the sacrificial layer

The removal of the sacrificial layer was performed in a phosphoric acid for 2 h. It is possible to accelerate the reaction rates by increasing the temperature of the solution of phosphoric acid and/or by placing the sample and the acid solution in an ultrasonic bath (Castille, 2010).

6.5 Results and discussion

Depending on the starting material, powder/binder ratio, and additives in making the paste, the results were reported and discussed.

Three groups powder A, B and C stand for Group A (BZT + 1.5 wt% Li_2O powder), Group B (BZT + 1.5 wt% Li_2O ceramic) and Group C (BZT ceramic + $\text{Li}_2\text{CO}_3\text{-Bi}_2\text{O}_3\text{-CuO}$), respectively.

6.5.1 Particle size distribution

Three groups of the BZT powders A, B and C were characterized particle size by using the laser particle size distribution as described below.

The particle size distribution of A, B and C were shown in figures 6.10, 6.11 and 6.12, respectively. It can be seen that groups A and C consisted of both nano and micro sizes. While group B has only nanopowder.

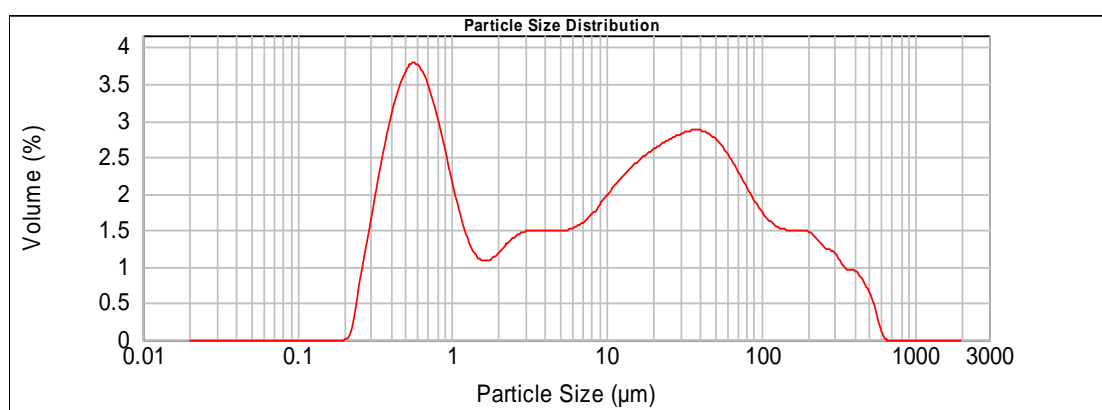


Figure 6.10 Particle size distribution of group A powder.

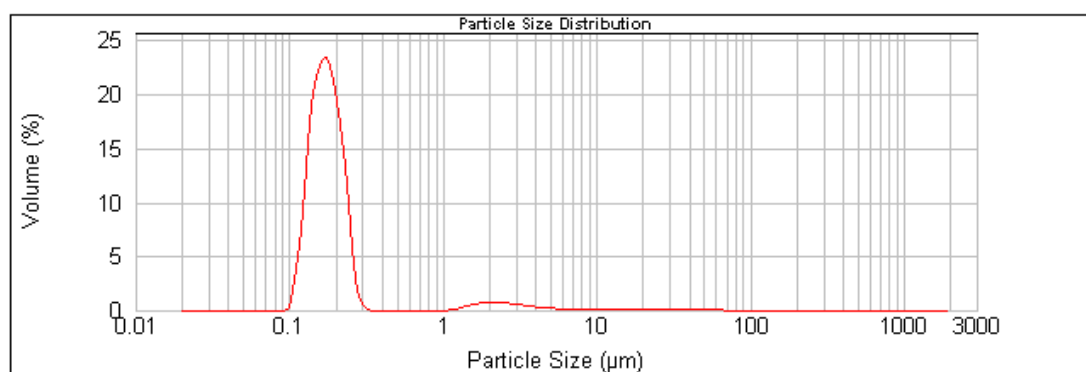


Figure 6.11 Particle size distribution of group B powder.

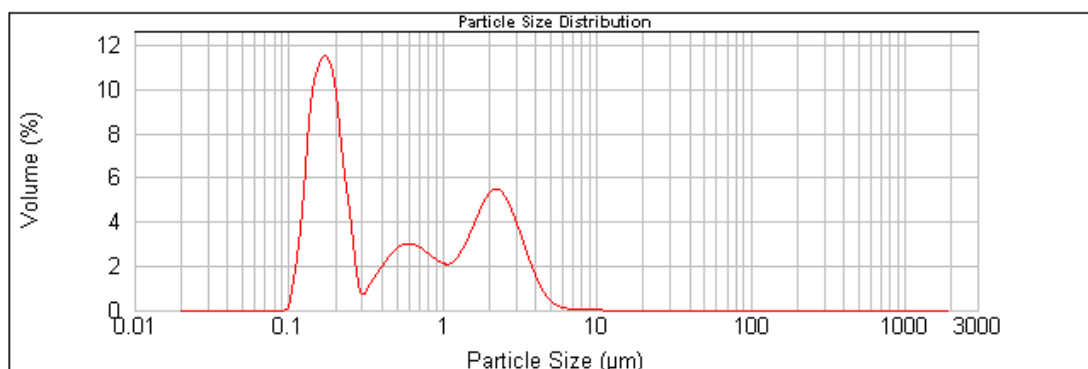


Figure 6.12 Particle size distribution of group C powder.

6.5.2 Effect of sintering condition

6.5.2.1 Green bodies of group A thick films (BZT + 1.5 wt% Li_2O powder)

The thick films were sintered at various sintering conditions as listed in table 6.1. It was noticed that the sintering condition of 900 °C, with a rate of 15 °C/min for 30 min was the best condition because of well sintering and low cracks was shown in figure 6.13. The sample is thus suitable for poling. Different temperature profiles and sacrificial layers were tested but the cracks still remained in the film. It seems that the appearance of crack caused by the inhomogeneity of the paste. Often that the cracks appeared close to the anchor plot as displayed in figure 6.14.

Table 6.1 Summary of sintering conditions of group A thick films.

Temperature (°C)	Heating rate (°C/min)	Firing time (min)	Characteristics of sintered BZT thick film
850	20	60	The sample was well sintered, and lots of micro-cracks were observed.
850	20	120	The sample was well sintered, and lots of micro-cracks were observed.
950	20	15	The sample was well sintered, and micro-cracks were observed.
950	20	25	The sample was well sintered, and micro-cracks were observed.
900	5	240	The sample was well sintered, and micro-cracks were observed.
900	15	30	The sample was well sintered, and low micro-cracks were observed was shown in figure 6.14

**Figure 6.13** The BZT (group A) cantilever of the element of dimension of $10 \times 2 \text{ mm}^2$ thickness $\sim 60 \text{ }\mu\text{m}$.



Figure 6.14 A picture and a sketch of the element of dimension of 8×2 mm showing the cracks (o) (Modified from Castille *et al.*, 2009).

6.5.2.2 Green bodies of group B thick films (BZT + 1.5 wt% Li_2O ceramic).

The results of the screen-printing in group B at various sintering condition were shown in figure 6.15

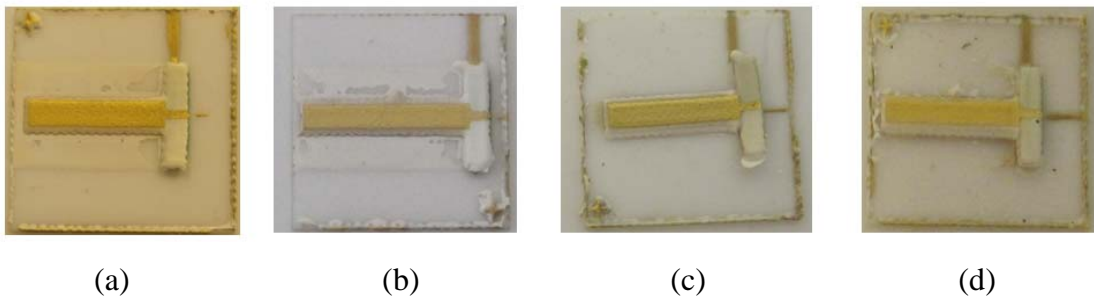


Figure 6.15 The thick film made from group B paste sintered at various sintering conditions (a) $850\text{ }^\circ\text{C}$ for 0.5 h, (b) $900\text{ }^\circ\text{C}$ for 0.1 h, (c) $900\text{ }^\circ\text{C}$ for 0.5 h, and (d) $900\text{ }^\circ\text{C}$ for 2 h.

It was observed that all the samples were well sintered but were not attached on the substrate and there was the bending of the beam. This was possibly due to the less viscosity of the nanopowder started paste leading to more shrinkage of the BZT thick film.

6.5.2.3 Green bodies of Group C thick films(BZT ceramic + Li_2CO_3 - Bi_2O_3 - CuO)

Green bodies of Group C thick films fired at various sintering conditions were listed in table 6.2.

Table 6.2 Summary of sintering conditions of group C thick films.

Temperature (°C)	Heating rate (°C/min)	Firing time (min)	Characteristics of sintered BZT thick film
850	15	30	The sample was well sintered, as shown in figure 6.16
900	15	10	The sample was well sintered.
900	15	30	The sample was well sintered.

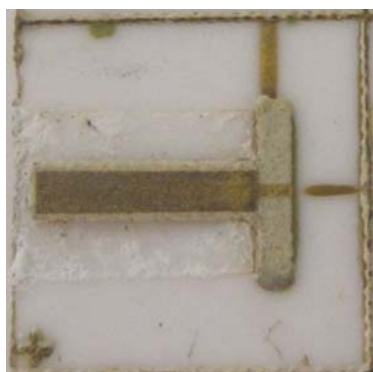


Figure 6.16 The Group C thick films sintering at 850 °C with a rate of 15 °C/min for 0.5 h.

From table 6.2, the sintering condition of 850 °C, with a rate of 15 °C/min for 0.5 h was suitable for poling. This was because the lowest sintering temperature and suitable temperature used with gold electrode is (melting point 1,063 °C).

6.5.3 Poling effect

The poling procedure was performed in order to activate the piezoelectricity in the polycrystalline element (see Chapter 2, section 2.1.1). This method involves with heating the piezoelectric component near the Curie temperature before applying an electric field. The dipoles in the sample will align their orientation in parallel to the direction of the electric field. For the cantilever, this procedure was done by placing the piezoelectric element in a cell thermostatically coupled to a vacuum pump where the moisture was removed and the helium coolant was used. Normally, the poling field in a range of 3-5 kV/mm was used (Castille, 2010).

6.5.4 Preliminary results

The poling process was carried out on the samples in group A ($\text{Ba}(\text{Zr}_{0.05}\text{Ti}_{0.95})\text{O}_3 + 1.5 \text{ wt\% Li}_2\text{O}$ powder) and group C ($\text{Ba}(\text{Zr}_{0.05}\text{Ti}_{0.95})\text{O}_3 + \text{Li}_2\text{CO}_3 - \text{Bi}_2\text{O} - \text{CuO}$ ceramic) with sintering conditions mentioned earlier. After poling, the dielectric constant of the samples (group A and C at best sintering condition) was measured by using HP4194A (Agilent). The value of dielectric constant and dielectric loss of group A (sintered at 900 °C with a rate of 15 °C/min for 30 min) were 300, and 0.1, respectively. Group C (sintering temperature to 850 °C, with a rate of 15 °C/min for 30 min.), the value of the dielectric constant and dielectric loss were 78.5, and 0.035, respectively. The preliminary results on electromechanical characterization of BZT cantilever were summarized in table 6.3

Table 6.3 Electrocmehanical characterizations of BZT cantilever.

Group of powder	f_r (kHz)	f_a (kHz)	k_{31} (%)	$-d_{31}$ (pC/N)	Q_m
$\text{Ba}(\text{Zr}_{0.05}\text{Ti}_{0.95})\text{O}_3 + \text{Li}_2\text{CO}_3 - \text{Bi}_2\text{O} - \text{CuO}$ ceramic (Group C)	48.450	48.675	10.66	10.28	162

6.6 Conclusions

The integration of BZT material into thick film technology was demonstrated in this chapter. The screen-printing process and free-standing cantilever structure were applied to produce the free-standing BZT cantilever. The screen-printing ink or paste has been produced from either BZT nanopowder or BZT micropowder for comparison. From the study, good cantilevers are obtained from the pastes made of micropowder of the $\text{Ba}(\text{Zr}_{0.05}\text{Ti}_{0.95})\text{O}_3$ with 1.5 wt % Li_2O and the $\text{Ba}(\text{Zr}_{0.05}\text{Ti}_{0.95})\text{O}_3$ with 3 %wt $\text{Li}_2\text{CO}_3\text{-Bi}_2\text{O}_3\text{-CuO}$.

CHAPTER 7

CONCLUSIONS AND FUTURE WORK

7.1 Main conclusions

(1) The integration of the piezoelectric bulk into the MEMS-based products is often expensive and some functional requirements are not achievable. Therefore, the piezoelectric thin films have been highly required. The present work presents the reliable synthetic route of acetic sol-gel and spinning method for the production of the $\text{Ba}(\text{Zr}_x\text{Ti}_{1-x})\text{O}_3$ or BZT thin films. The sol-gel BZT thin films with different x values ranging from 0.00-0.20 have been deposited on commercial Pt/Ti/SiO₂/Si substrates and have an average thickness of 350 ± 50 nm. The pyrolysis of 350 °C and annealing of 800 °C were used in the procedure. All the films possess single perovskite phase crystallized into different crystal structures, depending on the Zr/Ti ratios. The thin film without Zr crystallized into tetragonal structure whereas the $\text{Ba}(\text{Zr}_{0.05}\text{Ti}_{0.95})\text{O}_3$ film is orthorhombic. It is rhombohedral for both $\text{Ba}(\text{Zr}_{0.10}\text{Ti}_{0.90})\text{O}_3$ and $\text{Ba}(\text{Zr}_{0.15}\text{Ti}_{0.85})\text{O}_3$. Finally, the $\text{Ba}(\text{Zr}_{0.20}\text{Ti}_{0.80})\text{O}_3$ film is a cubic type. Unlike most of the PZT thin film, the BZT thin films have non-columnar microstructure and the grain size is decreasing with increasing Zr content. In contrast, the values of the dielectric constant for all the BZT thin films are increased with Zr and are comparable to those of the BZT films fabricated by other methods such as rf magnetron sputtering (Wu, Wu and Chen, 1996). Owing to its well-known capacity and high spatial resolution, the single-beam Michelson interferometer has been applied for measurement of the piezoelectric response in the thin films. Among the prepared BZT thin films, the orthorhombic $\text{Ba}(\text{Zr}_{0.05}\text{Ti}_{0.95})\text{O}_3$ exhibits best measured value of the piezoelectric coefficient, d_{33} of 35 pm/V. This can be explained that it is because the highest number of polarizable directions is found in the orthorhombic crystal structure, leading to the largest magnitude of the piezoelectric coefficient.

(2) The BZT powders of different Zr/Ti ratios can be derived from the sol-gel prepared previously in (1). This can be done by calcinations of the gel at 1,100 °C. The calcination has been further reduced to be 700 °C when adding the Li₂O additive into the gel. Concerning the crystalline structures of the calcined powder of different Zr/Ti ratios, they are completely similar to those of the thin films of the same compositions.

(3) In order to promote the use of BZT ceramics in applications where the bulk structure is necessary such as piezoelectric transformer and actuator, the sintering temperature should be lower and the production procedure could be simpler. In this work the Li₂O additive has been used in the preparation of the BZT ceramics and then the densification of the ceramics is taken place at temperature lower than the melting temperature of the electrodes. The grains of the BZT ceramic are much smaller after doping while the density is higher. However, the additive which is not piezoelectric has no effect on the electromechanical properties of the BZT ceramics.

(4) There have been a few reports regarding to the fabrication and properties of BZT-based thick films in spite of their possible applications in MEMS-based devices. This work presents the integration of BZT material into thick film technology focusing on screen-printing process and free-standing cantilever structure. The screen-printing ink or paste has been produced from either BZT nanopowder or BZT micropowder for comparison. Good cantilevers are obtained from the pastes made of micropowder of Ba(Zr_{0.05}Ti_{0.95})O₃ with 1.5 wt % Li₂O and Ba(Zr_{0.05}Ti_{0.95})O₃ with 3 %wt Li₂CO₃-Bi₂O-CuO.

7.2 Future work

Some difficulties arisen during the course of this work are:

- (a) a problem caused by a short circuit in the films with thick electrode layer,
- (b) the agglomeration of the powder which leads to a non-homogeneous paste,

The following topics are of interest for future study:

- (a) Measurements of the electromechanical coupling factor, k , an indicator of the energy conversion.
- (b) Measurements of the piezoelectric coefficient of the thick film.
- (c) The chemistry and the sintering mechanism of the element made from nanopowder.

REFERENCES

- ASTM.1997. Standard test for water absorption, bulk density, apparent porosity, and apparent specific gravity of fired whiteware products, *Designation C 373(72)*: 313-314.
- Berlincourt Piezo d_{33} meter manual. (1974).
- Bernardi, M., E. Antonelli, A. Lourenço, C. Feitosa, L. Maia, and A. Hernandes. 2007. BaTi_{1-x}Zr_xO₃ nanopowders prepared by the modified pechini method. *Journal of Thermal Analysis and Calorimetry* 87(3): 725-730.
- Böttger, U. 2005. Dielectric Properties of Polar Oxides. In *Polar Oxide: Properties, Characterization, and Imaging*, edited, Böttger, U., Tiedke, S. and Waser, R. 11-38. Weinheim: WILEY-VCH Verlag GmbH.
- Brinker, C. J. and Scherer, G. W. 1990. *Sol-Gel Science: The Physics and Chemistry of Sol-Gel Processing*. Academic Press Inc. Boston.
- Budd K. D., Dey, S. K., and Payne, D. A., 1986. The effect of hydrolysis conditions on the characteristics of PbTiO₃ gels and thin films, in *Better Ceramics Through Chemistry II*, Eds. C. J. Brinker *et al.*, *Materials Research Society Symposium Proceedings* 73: 711-716.
- Castille, C. 2010. Etude de MEMS piézoélectriques libérés et microstructurés par sérigraphie. Application à la détection en milieu gazeux et en milieu liquid. PhD thesis, Électronique, L'Université Bordeaux I.

- Castille, C., Dufour, I., Maglione, M., Debéda, H., Pellet, C. and Lucat C. 2009. Proceedings of the Eurosensors XXIII conference Sensor Application using longitudinal mode of screen-printed PZT cantilever. *Procedia Chemistry* 1: 971-974.
- Chen, I. W., and Wang, X. H. 2004. Sintering dense nanocrystalline ceramics without final-stage grain growth. *Nature* 404(6774): 168-171.
- Chen, X., Cai, W., Fu, C., Chen, H., and Zhang, Q. 2010. Synthesis and morphology of $\text{Ba}(\text{Zr}_{0.2}\text{Ti}_{0.8})\text{O}_3$ powders obtained by sol-gel method. *Journal of Sol-Gel Science and Technology*: 1-8.
- Cheng, W. X., Ding, A. L., He, X. Y., Zheng, X. S. and Qiu, P. S. 2006. Characterization of $\text{Ba}(\text{Zr}_{0.05}\text{Ti}_{0.95})\text{O}_3$ thin film prepared by sol-gel process. *Journal of Electroceramics* 16: 523-526.
- Choi, W. S., Jang, B. S., Roh, Y., Yi, J. and Hong, B. 2002. The effect of deposition temperature on the electrical and physical properties of the $\text{Ba}(\text{Zr}, \text{Ti})\text{O}_3$ thin films. *Journal of Non-Crystalline Solids* 303: 190-193.
- Chou, X., Zhai, J., Sun, J. and Yao, X. 2008. Preparation and dielectric properties of $\text{B}_2\text{O}_3\text{-Li}_2\text{O}$ -Doped $\text{BaZr}_{0.35}\text{Ti}_{0.65}\text{O}_3$ ceramics sintered at a low temperature. *Ceramics International* 34(4): 911-915.
- Ciomaga, C. E., Buscaglia, M. T., Viviani, M., Buscaglia, V., Mitoseriuv, L., Stancu, A. and Nanni, P. 2006. Preparation and dielectric properties of $\text{BaZr}_{0.1}\text{Ti}_{0.9}\text{O}_3$ ceramics with different grain sizes. *Phase Transitions* 79(6-7): 389-397.
- Cotton, D. P. J., Chappell, P. H., Cranny, A. and White, N. M. 2007. A new binderless thick-film piezoelectric paste. *Journal of Materials Science: Materials in Electronics* 18: 1037-1044.

- Damjanovic, A. 2005. Hysteresis in piezoelectric and ferroelectric materials. In *The Science of hysteresis volume I, II and III*. Bertotti G. and Mayergoz I. 337-452. Elsevier Inc.
- Dixit, A., Majumder, S. B., Savvinov, A. R., Katiyar, R. S., Guo, R. and Bhalla, A. S. 2002. Investigations on the sol-gel-derived barium zirconium titanate thin films. *Materials Letters* 56: 933-940.
- Dixit, A., Majumder, S. B., Katiyar, R. S. And Bhalla, A. S. 2003. Relaxor behavior in sol-gel-derived $\text{BaZr}_{(0.40)}\text{Ti}_{(0.60)}\text{O}_3$ thin films. *Applied Physic Letter* 82: 2679-2681.
- Dixit, A., Majumder, S. B., Katiyar, R. S. and Bhalla, A. S. 2005. Dielectric and tunable properties of $\text{BaZr}_x\text{Ti}_{1-x}\text{O}_3$ thin films. *Ferroelectric Letters*, 32: 131-137.
- Dobal, P. S., Dixit, A., Katiyar, R. S., Yu, Z., Guo, R. and Bhalla, A. S. 2001. Micro-Raman scattering and dielectric investigations of phase transition behavior in the BaTiO_3 - BaZrO_3 System. *Journal of Applied Physics* 89(12): 8085-8091.
- Ferrari, V. 2005. Chapter 4 Acoustic-wave piezoelectric and pyroelectric sensors based on PZT thick films. In *Smart sensors and mems*, Yurish, S. Y. and Gomes, M. T. S. R. 125-154 Netherlands. Kluwer Academic Publishers.
- Fu, C., Pan, F., Cai, W., Deng, X. and Liu, X. 2009. Microstructures and dielectric properties of $\text{BaZr}_{0.2}\text{Ti}_{0.8}\text{O}_3$ ceramics. *Symposia D, E and F from MRS International Materials Research Conference Journal of Physics: Conference Series* 152(012075): 1-6.
- Ferroperm Piezoceramics. 2003. Ferroperm Piezoceramics A/S: Denmark.

- Ginet, P. 2007. Conception et élaboration de microstructures en technologie hybride couche épaisse pour des applications MEMS. Électronique, PhD thesis L'Université Bordeaux I.
- Halder, S., Gerber, P., Schneller, T. and Waser, R. 2005. Electromechanical properties of $(\text{BaTi}_{1-x}\text{Zr}_x)\text{O}_3$ thin films. *Applied Physics A: Material Science & Processing* 81: 11-13.
- Hsi, C. S., Chen, Y. C., Jantunen, H., Wu, M. J., and Lin, T. C. 2008. Barium titanate based dielectric sintered with a two-stage process. *Journal of the European Ceramic Society* 28(13): 2581-2588.
- IEEE Standard definitions of primary ferroelectric Terms 1986. ANSI/IEEE Std., 180-1986. Published by The Institute of Electrical and Electronics Engineers, Inc., New York, NY 10017, USA.
- IEEE Standard on piezoelectricity. 1987. ANSI/IEEE Std., 178-1987 Published by The Institute of Electrical and Electronics Engineers, Inc., New York, NY 10017, USA.
- Ikeda T. 1990. *Fundamentals of piezoelectricity*. Oxford University Press: New York.
- Jaffe B., Cook W. R., and Jaffe H. 1971. *Piezoelectric Ceramics*, Academic Press, London.
- Jayadevan, K. P. and Tseng, T. Y. 2002. Review composite and multilayer ferroelectric thin films: processing, properties and applications. *Journal of Materials Science: Materials in Electronics* 13: 493-459.
- Jiwei, Z., Xi, Y., Liangying, Z., Bo, S., and Chen, H. 2004. Orientation control and dielectric properties of sol-gel deposited Ba (Ti, Zr)O₃ thin films. *Journal of Crystal Growth* 262: 341-347.

- Kay, H. F. and Vousdan, P. 1949. Symmetry changes in barium titanate at low temperature and their relation to its ferroelectric properties. *Philosophical Magazine* 7: 1019-1040.
- Khaenamkaew, P., Muensit, S., Bdikin, I. K. and Kholkin A. L. 2007. Effect of Zr/Ti ratio on the microstructure and ferroelectric properties of lead zirconate titanate thin films. *Materials Chemistry and Physics* 102: 159-164.
- Khaenamkaew, P., Kholkin, A. L., Bdikin, I. K. and Muensit, S. 2008. Microstructure and ferroelectric properties of graded PZT (40/52/60) and (60/52/40) thin films. *Ceramics International* 34: 1027-1030.
- Khaenamkaew, P. 2008. Ferroelectric and electromechanical properties of sol-gel PZT films with single-composition and compositionally graded structure. Ph D Thesis, Prince of Songkla University.
- Kim, S. G., Kang, C. Y., Choi, J. W., Kim, D. Y., Sung, M. Y., Kim, H. J. and Yoon, S. J. 2005. Properties of piezoelectric actuator on silicon membrane, prepared by screen printing method. *Materials Chemistry and Physics* 90: 401-404.
- Kuang, S.J., Tang, X.G., Li, L.Y. Jiang, Y.P. and Liu, Q.X. 2009. Influence of Zr dopant on the dielectric properties and Curie temperatures of $\text{Ba}(\text{Zr}_x\text{Ti}_{1-x})\text{O}_3$ ($0 \leq x \leq 0.12$) ceramics. *Scripta Materialia* 61 : 68–71.
- Liang, C. S., and Wu, J. M. 2005. Electrical Properties of W-doped $(\text{Ba}_{0.5}\text{Sr}_{0.5})\text{TiO}_3$ thin films. *Journal of Crystal Growth* 274(1-2): 173-177.
- Lucat, C., Ginet, P., Castille, C., Debéda, H. and Ménil, F. 2008. Microsystems elements based on free-standing thick-films made with a new sacrificial layer process. *Microelectronics Reliability* 48: 872-875.

- Lucat, C., Ginet, P. M enil, F. Deb eda, H. Production of multilayer microcomponents by the sacrificial thick layer method, CNRS Patent WO07077397, 2007-07-12.
- Mason, W. P. and Jafee, H. 1954. Methods for measuring piezoelectric, elastic, and dielectric constants of crystals and ceramics. *Proceedings of the IRE*. 42(6): 921-930.
- Masys, A. J., Ren, W., Yang, G. and Mukherjee, B. K. 2003. Piezoelectric strain in lead zirconate titanate ceramics as a function of electric field, frequency, and dc bias. *Journal of Applied Physics* 94:1155-1162.
- Moulson, A. J. and Herbert, J. M. 1990. *Electroceramics*. Chapman and Hall: New York.
- Moura, F., Simoes, A. Z., Stojanovic, B. D., Zaghete, M. A., Longo, E., and Varela, J. A. 2008. Dielectric and ferroelectric characteristics of barium zirconate titanate ceramics prepared from mixed oxide method. *Journal of Alloys and Compounds* 462: 125-134.
- Muensit, S. and Guy, I. L. 1998. Piezoelectric coefficients of gallium nitride thin films. *Applied Physics Letter* 72(15): 1896-1898.
- Muensit, S., and Khaenamkeaw, P. 2002. Michelson interferometer for the piezoelectric measurements. *Songklanakarin Journal of Science and Technology* 24(1): 107-117.
- Muensit, S., Sukwisut, P., Khaenamkeaw, P. and Lang, S. B. 2008. Piezoelectric coefficients of multilayer Pb(Zr,Ti)O₃ thin films. *Applied Physics A: Materials Science & Processing* 92(3): 659-663.
- Official Journal of the European Union, 2003.

- Palukuru, V.K., Peräntie, J., Komulainen, M., Tick, T. and Jantunen, H. 2010. Tunable microwave devices using low-sintering-temperature screen-printed barium strontium titanate (BST) thick films. *Journal of the European Ceramic Society* 30: 389-394.
- Piezoelectric Ceramics (PIEZOTITE®) Sensors. Cat.No.P19E-6, 2008. Murata Manufacturing Co., Ltd.
- Pontes, F. M., Escote, M. T., Escudeiro, C. C., Leite, E. R., Longo, E., Chiquito, A. J., Pizani, P. S. and Varela, J. A. 2004. Characterization of $\text{BaTi}_{1-x}\text{Zr}_x\text{O}_3$ thin films obtained by a soft chemical spin-coating technique. *Journal of Applied Physics* 96(2): 4386-4391.
- Qi, J. Q., Wang, Y., Chen, W. P., Li, L. T. and Chan, H. L. W. 2006. Perovskite barium zirconate titanate nanoparticles directly synthesized from solutions. *Journal of Nanoparticle Research* 8: 959-996.
- Schwartz, R. W., Schneller, T. and Waser, R. 2004. Preliminary communication / Communication chemical solution deposition of electronic oxide films. *C. R. Chimie* 7:433-461.
- Schwarzkopf, J. and Fornari, R. 2006. Epitaxial growth of ferroelectric oxide films. *Progress in Crystal Growth and Characterization of Materials* 52: 159-212.
- Setter, N. Electroceramics: Looking ahead. 2001. *Journal of the European Ceramic Society* 21(10-11): 1279-1293.
- Seveyrat L.S. and Gonnard P. 2003. Processing and characterization of piezoelectric thick films screen-printed on silicon and glass-ceramic substrates *Integrated Ferroelectrics* 51: 1-18.

- Shrout, T. R. and Zhang, S. J. 2007. Lead-free piezoelectric ceramics: Alternatives for PZT?. *Journal of Electroceramics* 19: 111-124.
- Stojanovic, B. D., Foschini, C. R., Pavlovic, V. B., Pavlovic, V. M., Pejovic, V. and Varela, J. A. 2002. Barium titanate screen-printed thick films. *Ceramics International* 28(3): 293-298.
- Stojanovic, B. D., Foschini, C. R., Pejovic, V. Z. , Pavlovic, V. B. and Varela, J. A. 2004. Electrical properties of screen printed BaTiO₃ thick films. *Journal of the European Ceramic Society* 24(6): 1467-1471.
- Springer-Verlag, 1981. Landolt-Bornstein Numerical Data and Functional Relationship in Science and Technology. Berlin, III/28a, pp268; III/16a, pp422, in Qi, J.Q., Wang, Y., Chen, W.P., Li, L.T. and Chan, H.L.W. 2006. Perovskite barium zirconate titanate nanoparticles directly synthesized from solutions. *Journal of Nanoparticle Research* 8:959-996.
- Su, B., Holmes, J. E., Meggs, C. and Button, T. W. 2003. Dielectric and microwave properties of barium strontium titanate (BST) thick films on alumina substrates. *Journal of the European Ceramic Society* 23: 2699-2703.
- Swartz, S. L. 1990. Topics in electronic ceramics. *IEEE Transaction Electrical Insulation* 25: 935-987.
- Tadigadapa, S., and Mateti, K. 2009. Piezoelectric mems sensors: State-of-the-Art and Perspectives. *Measurement Science and Technology* 20(9): 1-30.
- Tang, X. G., Wang, J., Wang, X. X. and Chan, H. L. W. 2004. Effects of grain size on the dielectric properties and tunabilities of Sol-gel derived Ba(Zr_{0.2}Ti_{0.8})O₃ ceramics. *Solid State Communications* 131(3-4): 163-168.

- Tang, X. G., Chew, K.-H. and Chan H. L. W. 2004. Diffuse phase transition and dielectric tenability of $\text{Ba}(\text{Zr}_y\text{Ti}_{1-y})\text{O}_3$ relaxor ferroelectric ceramics. *Acta Materialia* 52: 5177-5183.
- Tick, T., Peräntie, J., Rentsch, S., Müller, J., Hein, M. and Jantunen, H. 2008. Co-sintering of barium strontium titanate (BST) thick films inside a LTCC substrate with pressure-assisted sintering. *Journal of the European Ceramic Society* 28(14): 2765-2769.
- Torah, R. N., Beeby, S. P., Tudor, M. J. and White, N. M. 2007. Thick-film piezoceramics and devices. *Journal of Electroceramics* 19: 95-110.
- U.S Department of Health and Human Services, Public Health Service Agency for Toxic Substances and Disease and Registry, 2007.
- Uchino, K. 1997. *Piezoelectric Actuators and Ultrasonic Motors*. 2nded. Kluwer Academic Publishers: Boston.
- Valant, M., and Suvorov, D. 2004. Low-temperature sintering of $(\text{Ba}_{0.6}\text{Sr}_{0.4})\text{O}_3$. *Journal of the American Ceramic Society* 87(7): 1222-1226.
- Valant, M., Suvorov, D., Pullar, R. C., Sarma, K. and Alford, N. M. 2006. A mechanism for low-temperature Sintering. *Journal of the European Ceramic Society* 26(13): 2777-2783.
- Veith, M., Mathur, S., Lecere, N., Huch, V. and Decker, T. 2000. Sol-gel synthesis of nano-scaled BaTiO_3 , BaZrO_3 and $\text{BaTi}_{0.5}\text{Zr}_{0.5}\text{O}_3$ oxides via single-source alkoxide precursors and semi-alkoxide routes. *Journal of Sol-Gel Science and Technology* 15: 145-158.

- Wang, X. H., Deng, X. Y., Zhou, H., Li, L. T. and Chen, I. W. 2008. Bulk dense nanocrystalline BaTiO₃ ceramics prepared by novel pressureless two-step sintering method. *Journal of Electroceramics* 21(1): 230-233.
- Wang, X. H., and Chen, I. W. 2006. Sintering of nanoceramics. In *Nanomaterials Handbook*: CRC Press,
- William, D. and Callister, Jr. 2005. *Fundamentals of Materials Science and Engineering: An Integrated Approach*. 2nd ed. John Wiley & Sons Inc: United States of America.
- Wu, T. B., Wu, C. M. and Chen, M. L. 1996. Highly insulative barium zirconate titanate thin films prepared by rf magnetron sputtering for dynamic random access memory applications. *Applied Physics Letters* 69: 2659-2661.
- Yao, K. and Zhu, W. 1998. Improved preparation procedure and properties for a multilayer piezoelectric thick-film actuator. *Sensors and Actuators A* 71: 139-143.
- Yordsri, V., Binhayeeniyi, N., Muensit, N. and Thanachayanont, C. 2011. *Proceeding The 28th Annual Conference of the Microscopy Society of Thailand*. Chiang Rai, Thailand.
- Yu, Z., Guo, R. and Bhalla, A. S. 2000. Orientation dependence of the ferroelectric and piezoelectric behavior of Ba(Ti_{1-x}Zr_x)O₃ single crystals. *Applied Physics Letter* 77: 1535-1537.
- Yu, Z., Ang, C., Guo, R. and Bhalla, A. S. 2002. Piezoelectric and strain properties of Ba(Ti_{1-x}Zr_x)O₃ ceramics. *Journal of Applied Physics* 92(3): 1489-1493.

- Zhai, J., Yao, X., Zhang, L., and Shen, B. 2004. Dielectric nonlinear characteristics of $\text{Ba}(\text{Zr}_{0.35}\text{Ti}_{0.65})\text{O}_3$ thin films grown by a sol-gel process. *Applied Physics Letter* 84(16): 3136-3138.
- Zhang, Q. Q., Gross, S. J., Tadigadapa, S., Jackson, T. N. Djuth, F. T., Trolier-McKinstry, S. 2003. Lead zirconate titanate films for d_{33} mode cantilever actuators. *Sensors and Actuators A* 105: 91-97.
- Zhang Q. M., Pan W. Y., and Cross L. E. 1988. Laser interferometer for the study of piezoelectric and electrostrictive strains, *Journal of Applied Physics* 63: 2492-2496.
- Zimmermann, F., Voigts, M. Menesklou, W. and Ivers-Tiffée, E. 2004. $\text{Ba}_{0.6}\text{Sr}_{0.4}\text{TiO}_3$ and $\text{BaZr}_{0.3}\text{Ti}_{0.7}\text{O}_3$ thick films as tunable microwave dielectrics. *Journal of the European Ceramic Society* 24(6): 1729-1733.

VITAE

Name Miss Nawal Binhayeeniyi

Student ID 5010230026

Educational Attainment

Degree	Name of Institution	Year of Graduation
B.Sc.(Physics)	Prince of Songkla University	2000
M.Sc.(Physics)	Prince of Songkla University	2003

Scholarship Awards during Enrolment

Grant from Princess Naradhiwas University, 2007

The Program Strategic Scholarships for Frontier Research Network for the Jointed Ph.D. Program Thai Doctoral Degree from the Office of the Higher Education Commission, 2008-2011.

Franco-Thai Joint Research Project under the Office of the Higher Education Commission, Thailand and the Partenariat Hubert Curien (PHC) Program, France, 2009-2010

NANOTEC Center of Excellence at PSU, 2010

Work – Position and Address

Position	Address
Lecturer	Faculty of Science and Technology, Princess of Naradhiwas University , Narathiwat

List of Publications and Proceedings

Publications

1. **Binhayeeniyi, N.**, Dasaesamoh, A., Khakong, J., Khaenamkaew, P., and Muensit, S. 2008. Micro- and Macroscopic Observations of the Microtexture, the Dielectric and Piezoelectric Properties in Bulk and Multilayer Pb(Zr,Ti)O₃. *Advanced Materials Research*. 55-57:45-48.
2. **Binhayeeniyi, N.**, Sukvisut,P., Thanachayanont, C., and Muensit, S. 2010. Physical and electromechanical properties of barium zirconium titanate synthesized at low-sintering temperature, *Materials Letters* 64:305–308.

Proceedings

1. **Binhayeeniyi, N.**, Khakong,J. Khaenamkaew,P., and Muensit, S. 2008. Micro- and Macroscopic Observations of the Microtexture, the Dielectric and Piezoelectric Properties in Bulk and Multilayer $\text{Pb}(\text{Zr,Ti})\text{O}_3$. International Conference on Smart Materials Smart/Intelligent Materials and Nanotechnology and 2nd International Workshop on Functional Materials and Nanomaterials.22-25 April, 2008, Chaing Mai, Thailand.
2. **Binhayeeniyi, N.** and Muensit, S. 2008. Sol-gel derived $\text{BaZr}_x\text{Ti}_{1-x}\text{O}_3$ thin films of different elaborating conditions for use as microsensors. The 2nd Thailand Nanotechnology Conference [TNC] Nanomaterials for Health, Energy and Environment, 13-15 August, 2008, Phuket. Thailand.
3. **Binhayeeniyi, N.**, Lucat, C., Debéda H. and Muensit, S. Screen-Printed BZT for Cantilever. The 3rd Thailand Nanotechnology Conference [TNC] Nanomaterials for Health, Energy and Environment, 21-22 December, 2009, Bangkok. Thailand.
4. Muensit, S. and **Binhayeeniyi N.** Nanopowders of barium zirconium titanate for applications in electronic devices. IEEE International Nano Electronics Conference (INEC), 3-8 January 2010, Hong Kong, China.
5. Binhayeeniyi, N., **Thanachayanont, C.** and Muensit, S. The 27th Annual Conference of the Microscopy Society of Thailand. 20-22 January 2010, Fair House Beach Resort & Hotel, Koh Samui, Surat Thani, Thailand.
6. Yordsri, V., Binhayeeniyi, N., Muensit, N., and **Thanachayanont, C.** The 28th Annual Conference of the Microscopy Society of Thailand. 5-7 January 2011, Chiang Rai, Thailand.